Characterizing Design-Basis Fire Exposure for Highway Bridges

Principal Investigator: Spencer Quiel, Ph.D., P.E. (Lehigh University)
Project Team: Zheda Zhu, Ph.D. (Lehigh University)
Thomas Murphy, Ph.D., P.E. (Modjeski & Masters, Inc.)
Maria Lopez, Ph.D., P.E. (Modjeski & Masters, Inc.)
Frank Artmont, Ph.D., P.E. (Modjeski & Masters, Inc.)

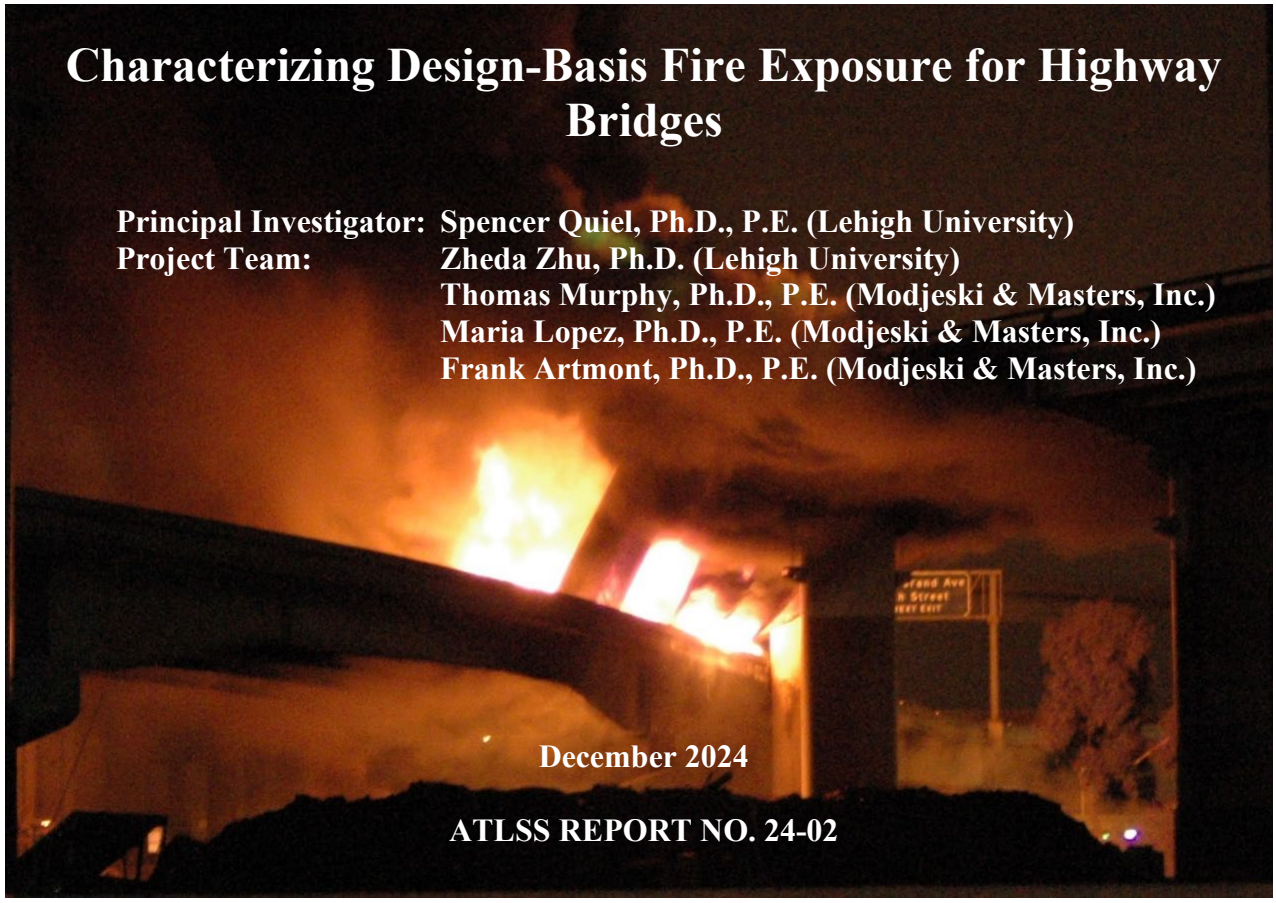

December 2024

ATLSS REPORT NO. 24-02

ATLSS is a National Center for Engineering Research on

Advanced Technology for Large Structural Systems

117 ATLSS Drive

Bethlehem, PA 18015-4729

Phone: (610)-758-3525
Fax: (610)-758-5902

www.atlss.lehigh.edu
Email: inatl@lehigh.edu

Cover photo by Philip Liborio Gangi (https://liboriogangi.tripod.com; used with permission)

Technical Report Documentation Page

1. Report No. ATLSS 24-02	**2. Gov't Accession No**. N/A	**3. Recipient's Catalog No.** N/A
4. Title and Subtitle Characterizing Design-Basis Fire Exposure for Highway Bridges		**5. Report Date** 12/19/2024 **6. Performing Org. Code** N/A
7. Author(s) Spencer Quiel, Ph.D., P.E. (Principal Investigator, Lehigh Univ., ORCID ID: 0000-0002-1316-7059) Zheda Zhu, Ph.D. (Lehigh Univ., ORCID ID: 0000-0001-5408-3110) Thomas Murphy, Ph.D., P.E. (Modjeski and Masters, Inc.) Maria Lopez, Ph.D., P.E. (Modjeski and Masters, Inc.) Frank Artmont, Ph.D., P.E. (Modjeski and Masters, Inc.)		**8. Performing Org. Report No.** N/A
9. Performing Organization Name and Address Lehigh University 117 ATLSS Drive Bethlehem, PA 18015 Modjeski and Masters, Inc. 100 Sterling Parkway, Suite 302 Mechanicsburg, PA 17050		**10. Work Unit No.** N/A **11. Contract or Grant No.** 693JJ321C000035
12. Sponsoring Agency Name and Address Federal Highway Administration 1200 New Jersey Avenue, SE Washington, DC 20590		**13. Type of Report and Period** Sept. 2021 – April 2024 **14. Sponsoring Agency Code** HIBS
15. Supplementary Notes None		

16. Abstract

This report addresses the development of design-basis fire exposure levels for highway bridges, which can define the thermal load in a performance-based structural-fire engineering framework. Several approaches are presented for characterizing the spatial and temporal thermal impact of open-air fires from both vehicles and stationary fuel sources under or near highway bridges. A vulnerability assessment is performed to establish spatial influence zones for structurally significant fire sizes (i.e., fires that are large enough to cause structural damage) based on their heat release rate (HRR) as well as their proximity and orientation to the bridge's primary structural elements. The frequency of a structurally significant fire hazard is characterized according to the type of primary structural element, its location relative to other roadways, and the traffic conditions on those roadways. A reliability-based design fire load is then stochastically determined in terms of maximum incident heat flux. The most critical parameters that influence the design fire load are the standoff and clearance from the closest roadways or other fuel locations to a given bridge span. A closed-form equation is developed to quantify the design fire load for a bridge span as a function of these two parameters.

17. Key Words Highway bridges, fire intensity, fire frequency, fire design load	**18. Distribution Statement** No restrictions.		
19. Security Classification (of this report): Unclassified	**20. Security Classification (of this page):** Unclassified	**21. No. of Pages:** 72	**22. Price** N/A

Form DOT F 1700.7 (8-72) Reproduction of completed page authorized.

SI* (MODERN METRIC) CONVERSION FACTORS

APPROXIMATE CONVERSIONS TO SI UNITS

Symbol	When You Know	Multiply By	To Find	Symbol
		LENGTH		
in	inches	25.4	millimeters	mm
ft	feet	0.305	meters	m
yd	yards	0.914	meters	m
mi	miles	1.61	kilometers	km
		AREA		
in^2	square inches	645.2	square millimeters	mm^2
ft^2	square feet	0.093	square meters	m^2
yd^2	square yard	0.836	square meters	m^2
ac	acres	0.405	hectares	ha
mi^2	square miles	2.59	square kilometers	km^2
		VOLUME		
fl oz	fluid ounces	29.57	milliliters	mL
gal	gallons	3.785	liters	L
ft^3	cubic feet	0.028	cubic meters	m^3
yd^3	cubic yards	0.765	cubic meters	m^3
		NOTE: volumes greater than 1000 L shall be shown in m^3		
		MASS		
oz	ounces	28.35	grams	g
lb	pounds	0.454	kilograms	kg
T	short tons (2000 lb)	0.907	megagrams (or "metric ton")	Mg (or "t")
		TEMPERATURE (exact degrees)		
°F	Fahrenheit	5 (F-32)/9 or (F-32)/1.8	Celsius	°C
		ILLUMINATION		
fc	foot-candles	10.76	lux	lx
fl	foot-Lamberts	3.426	$candela/m^2$	cd/m^2
		FORCE and PRESSURE or STRESS		
lbf	poundforce	4.45	newtons	N
lbf/in^2	poundforce per square inch	6.89	kilopascals	kPa

APPROXIMATE CONVERSIONS FROM SI UNITS

Symbol	When You Know	Multiply By	To Find	Symbol
		LENGTH		
mm	millimeters	0.039	inches	in
m	meters	3.28	feet	ft
m	meters	1.09	yards	yd
km	kilometers	0.621	miles	mi
		AREA		
mm^2	square millimeters	0.0016	square inches	in^2
m^2	square meters	10.764	square feet	ft^2
m^2	square meters	1.195	square yards	yd^2
ha	hectares	2.47	acres	ac
km^2	square kilometers	0.386	square miles	mi^2
		VOLUME		
mL	milliliters	0.034	fluid ounces	fl oz
L	liters	0.264	gallons	gal
m^3	cubic meters	35.314	cubic feet	ft^3
m^3	cubic meters	1.307	cubic yards	yd^3
		MASS		
g	grams	0.035	ounces	oz
kg	kilograms	2.202	pounds	lb
Mg (or "t")	megagrams (or "metric ton")	1.103	short tons (2000 lb)	T
		TEMPERATURE (exact degrees)		
°C	Celsius	1.8C+32	Fahrenheit	°F
		ILLUMINATION		
lx	lux	0.0929	foot-candles	fc
cd/m^2	$candela/m^2$	0.2919	foot-Lamberts	fl
		FORCE and PRESSURE or STRESS		
N	newtons	0.225	poundforce	lbf
kPa	kilopascals	0.145	poundforce per square inch	lbf/in^2

TABLE OF CONTENTS

LIST OF FIGURES

NOTE: All figures in this report are credited to co-authors Quiel and Zhu unless otherwise noted in the corresponding caption.

LIST OF TABLES

LIST OF ABBREVIATIONS

AADT	average annual daily traffic
AASHTO	American Association of State Highway and Transportation Officials
AHJ	authority having jurisdiction
AISC	American Institute of Steel Construction
ANCOVA	analysis of covariance
ASTM	American Society for Testing and Materials
Caltrans	California Department of Transportation
CDF	cumulative density function
CFD	computational fluid dynamics
CFR	Code of Federal Regulations
DOT	Department of Transportation
FARS	Fatal Accident Reporting System
FDS	Fire Dynamics Simulator
FDV	fire damage vulnerability
FE	finite element
FVM	finite volume method
HDPE	high-density polyethylene
HGV	heavy good vehicles
HRR	heat release rate
kip	1,000 lbf
ksi	kips per square inch
LHS	Latin hypercube sampling
LRFD	load and resistance factor design
MCM	Mudan and Croce's method
MCS	Monte Carlo simulation
MDSF	modified discretized solid flame
$MDSF_2$	modified discretized solid flame, 2nd generation
MPS	modified point source
NFPA	National Fire Protection Association
NIST	National Institute of Standards and Technology
NTSB	National Transportation Safety Board
NWC	normal-weight concrete
PCI	Precast/Prestressed Concrete Institute
PDF	probability density function
PennDOT	Pennsylvania Department of Transportation
PIARC	World Road Association
PS	point source
RWS	Rijkswaterstaat
SBDM	Shokri and Beyler's detailed method
SF	solid flame
SFPE	Society of Fire Protection Engineers
SVM	support vector machine
TFR	traffic fire rate
TP	truck percentage
TVRA	threat, vulnerability, and risk assessment

LIST OF NOTATIONS

A_f	area of pool fire footprint (m^2)
$A_{f,M}$	total surface area of the flame shape for $MDSF_2$ model
A_i	area of the intersected regions of the roadway underneath the target bridge for HRR_i
C_{ls}	capacity of the structure with respect to a pre-defined limit state ls
$D_{f,eff}$	effective diameter of the pool fire footprint (m)
DM	damage measure
E_{flame}	flame emissive power (kW/m^2)
E_i	emissive power and the area of the i^{th} element on the fire surface (kW/m^2)
E_{max}	flame emissive power for MCM model (kW/m^2)
E_{MCM}	effective emissive power of the MCM model (kW/m^2)
E_s	emissive power of smoke (kW/m^2)
E_{SBDM}	effective emissive power of the SBDM model (kW/m^2)
E_{tot}	total combustion energy (GJ)
E_{tot}^{up}	upper bound total combustion energy (GJ)
E_{tot}^{low}	lower bound total combustion energy (GJ)
F	risk objective
F_{12}	view factor from the fire to the target
$F_{12,H}$	view factor for horizontally oriented targets
$F_{12,V}$	view factor for vertically oriented targets
$F_{i\to j}$	view factor for element *i* to target *j*
$\Delta H_{c,eff}$	effective heat of combustion (kJ/kg)
H_f	flame height (m)
$H_{f,MCM}$	flame height for Mudan and Croce Method (m)
IM	intensity measure
$L_{A_i-A_{i-1}}$	length of the increased region from A_{i-1} to A_i between successive fire intensities
L_f	length (long edge dimension) of the pool fire footprint (m)
$\dot{Q}_{f,max}$	peak heat release rate (kW)
R	length of the line of sight from the point source to the center of the target (m)
R_s	risk performance criteria for hazardous structural events
S	extinction coefficient (m^{-1})
T_0	ambient temperature (°C)
V_{fuel}	combusted fuel volume (m^3)
W_f	width (long edge dimension) of the pool fire footprint (m)
b	bias term for boundary equation classifying the damage of structure member
$f_{ss,i}$	the number of structurally significant fires corresponds to certain fire intensity HRR_i
f_{ss}	annual number of structurally significant fires
g	gravitational acceleration constant (m/s^2)
k	time width coefficient for exponential heat release rate fire curve (s^{-1})
$\dot{m}_{\infty}^{"}$	maximum mass loss rate per unit area (kg/m^2-sec)
$\dot{m}^{"}$	mass loss rate per unit area related to fuel type and the equivalent diameter the footprint
n	retard index for exponential heat release rate fire curve
$\dot{q}^{"}$	incident radiative heat flux (kW/m^2)
$\dot{q}_D^{"}$	design heat flux for bridge
r	amplification coefficient for exponential HRR fire curve
$r_{i\to j}$	the distance or "radius" from the center of fire surface element *i* to target *j*
s	standoff, measures the minimum plane distance from the bridge to the roadway (m)
$\overline{s}$	normalized standoff
t	time in minutes

t_b	time needed to consume fuel for combustion over the pool area (sec)
t_d	end time of the fire hazard (sec)
t_D	time interval of decay phase (sec)
t_g	time of fire growth for quadratic fire curve of pool fire (sec)
t_h	time in hours
t_{max}	time interval of reaching the peak heat release rate (sec)
$w_1,\ w_2$	weighting factors for boundary equation classifying the damage of structure member
Δz	clearance of the bridge (m)
$\overline{\Delta z}$	normalized clearance
$\alpha_{g,L}$	linear growth rate for linear fire HRR curve (kW/s)
$\alpha_{D,L}$	linear decay rate for linear fire HRR curve (kW/s)
$\alpha_{g,q}$	growth rate of quadratic heat release rate time history curve (kW/s^2)
$\alpha_{D,q}$	decay rate of quadratic heat release rate time history curve (kW/s^2)
β_d	ratio between the integrated energy and the total energy for exponential HRR fire curve
$\kappa\beta$	empirical coefficient (m^{-1})
φ_{cyl}	the ratio of cylinder portion to the flame height
φ_{lum}	the ratio of luminous portion of the flame to the entire flame height
ρ_a	ambient air density (kg/m^3)
θ_i	absolute angle between the radius vector and the fire element's normal vector
θ_j	absolute angle between the radius vector and the target surface normal vector
ρ	density of specific fuel (kg/m^3)
χ	combustion efficiency
$\chi_{r,f}$	radiative fraction of the flames for $MDSF_2$ model
$\chi_{r,f\,max}$	maximum radiative fraction of the flames for $MDSF_2$ model
$\chi_{r,mps}$	radiative fraction for modified point source model
$\chi_{r,ps}$	point source radiative fraction

EXECUTIVE SUMMARY

When fire events occur, local transportation authorities and national agencies become increasingly aware of the impact of fire on their bridge inventories. This project provides design information that can complement and expand on Chapter 6 in National Fire Protection Association (NFPA) 502[1] [1], with the goal of enabling bridge designers and owners to make informed decisions about fire mitigation based on the calculated response of the structural system to likely fire hazards. A performance-based evaluation and mitigation of severe fire hazards for highway bridges includes the following steps:

(1) Characterize the size, proximity, and probability of a potential design basis fire.
(2) If a structurally significant hazard is identified, model the fire and calculate the resulting thermal exposure to the bridge structure.
(3) Evaluate the potential for fire-induced structural damage.
(4) Determine practical mitigation measures based on available resources and risk tolerance.

The information and techniques in this report can inform authorities having jurisdiction (AHJ) when evaluating the vulnerability of highway bridges to structurally significant fire hazards. This study address items (1) and (2) from the list above, namely the selection of a design fire exposure which accounts for likely hazards (such as vehicles passing under or near the bridge or stationary fuel sources that are stored or staged near the bridge). Thermal exposure from the design fire can define the thermal load in a performance-based structural-fire engineering evaluation of the bridge's primary structural system. The following questions are addressed in this report.

Are there any current specifications for bridge fire design?

Fire is not explicitly addressed in the current American Association of State Highway and Transportation Officials (AASHTO) Bridge Design Specifications[2] [2], nor is it addressed in most bridge design manuals that are maintained by state departments of transportation (DOTs). NFPA 502[1] Chapter 6 [1] is applicable only for bridges more than 1000 ft. (300 m) in length even though most of the overpasses that have collapsed in the last 30 years have been shorter spans. Additionally, while long-span bridge projects often need an evaluation for fire hazards via a threat, vulnerability, and risk assessment (TVRA), short- and medium-span bridge projects such as the common highway overpasses impacted by the previously mentioned fire events typically include no such need. NFPA 502[1] Section 6.3 states that "… the primary structural elements of bridges or elevated highways shall be protected to achieve the following functional requirements …":

a) support firefighter accessibility
b) mitigate structural damage and prevent collapse
c) minimize economic impact

The document states that an "engineering analysis," including the consideration of design fire scenarios and their proximity to the structure, is needed to determine whether the collapse of the bridge due to fire would

[1] Use of NFPA 502, Standard for Road Tunnels, Bridges, and Other Limited Access Highways, is not a Federal requirement.

[2] FHWA approves the use of the AASHTO LRFD Bridge Design Specifications 9th Edition, although the use is not required (see Memorandum dated April 11, 2022 at https://www.fhwa.dot.gov/bridge/structures/04112022.pdf).

have adverse impacts to life safety or other unacceptable impacts to functionality. NFPA 502[1] Section A.6.3.2 suggests the following fire scenarios for consideration in the analysis:

i. For bridges spanning moving traffic, the design fire scenario typically includes an HGV.
ii. For bridges spanning a freeway or highway, the design fire scenario typically includes a flammable tanker.

Beyond this information, little is provided regarding the available approaches and performance objectives for such an analysis. This report therefore addresses the development of structurally significant design fire exposures as input for the engineering analysis of a bridge based on its vulnerability to various fire scenarios.

Why is it important to consider fire effects on bridge structures?

Fires can cause significant damage to bridge structures, thus threatening user life safety as well as the functionality of the transportation network. Between 1980 and 2012, fire events caused bridge failure in the U.S. at an annualized rate that is consistent with other hazards such as earthquakes and construction defects [3–5]. Most of the fire-induced bridge failures in the United States (U.S.) from 1980 to 2023 have involved highway overpasses that are subjected to the effects of burning tanker trucks, heavy goods vehicles (HGVs), or a platooned combination of vehicles. These events include but are not limited to the near-collapse of an I-65 overpass near Birmingham, AL in 2002; the total collapse of a MacArthur Maze I-80/I-580/I-880 interchange overpass in Oakland, CA in 2007; severe damage leading to demolition of a Route 22/322 overpass at I-81 near Harrisburg, PA in 2013; and the collapse of an I-95 overpass just north of Philadelphia, PA in 2023. Fire hazards due to materials stored underneath bridges have also been highlighted by the total collapse of an I-85 overpass in Atlanta, GA in March 2017, where high-density polyethylene (HDPE) conduit stored under the overpass caught fire and caused the collapse of a 90-ft section of the overpass. A more comprehensive tabulation of fire-induced bridge failures in the U.S. from 1995 to 2023 is provided in this report.

What input parameters are needed to characterize the fire?

The following basic parameters are needed to characterize the intensity of the design fire:

- **Fuel types** have different characteristics such as heat of combustion (i.e., calorific value per unit mass), mass loss rate, soot yield, etc. A fire fueled by a hydrocarbon fuel such as gasoline will generally be more intense and have a higher heat release rate (HRR) and flame height than a fire fueled by a cellulosic material such as wood. Fires from vehicle and other flammable solid materials involve an eclectic combination of fuels and is often approximated using a hydrocarbon fire equivalent based on the estimated peak HRR.
- **Total combustion energy** represents the total amount of energy released via combustion of the fuels consumed by the fire and is typically expressed in units of megajoules. Most fires that threaten bridges are open air and are thus fuel controlled. The total combustion energy therefore is a contributing parameter to the duration of the fire hazard from ignition to burnout.
- **Footprint size** refers to the area over which the fire has spread and is typically measured in square meters or square feet. A larger footprint offers more surface area for combustion of the available fuels, thus generating more intensity but with faster consumption of the fuel.

What parameters characterize the intensity of fire effects on bridge structures?

Fire effects on structures can be characterized as a time history of either temperature exposure or heat flux exposure (typically in units of power per unit area or kW/m^2). Temperature exposure is often used for enclosed spaces in buildings or tunnels due to the buildup of hot gases and the confinement of flames. Heat flux is more appropriate for the open-air fires that typically affect bridges unless the fire is significantly entrapped underneath the bridge, in which case the bridge would be evaluated more like a tunnel (per NFPA 502[1] Chapter 7). The following parameters are needed to calculate the heat flux imparted to a bridge's structural elements from a nearby fire:

- **Heat release rate (HRR**) is the rate at which energy is released by a fire and is typically expressed in units of megawatts. The peak HRR can characterize the intensity of the fire and is a function of the size and type of the fuel source. Details regarding the calculation of HRR are provided in Section 2.1 of this report.
- **Duration** of the fire from ignition to burnout consists of three general stages: initial ramp up, peak HRR, and decay. Though the entire duration of the fire should be considered, the heat flux imparted to the structure during the time at peak HRR will have the most impact. Details regarding the development of the HRR time history are provided in Section 2.2.
- **Flame height** is measured as the vertical distance from the fuel source to the top of the flames produced by the fire. Flame height will determine the location from which the fire emits radiative heat flux to the target structure. For fires underneath a bridge, flame heights that exceed the clearance from the fuel source to the structural elements will result in engulfment and high levels of directly applied heat flux. Details regarding the calculation of flame height are provided in Section 3.2.
- **Proximity and orientation** of the fire to the bridge's structural elements will determine the intensity and surface area of thermal exposure on those elements. Fires located directly underneath a bridge will generally impart more thermal exposure than fires located alongside the bridge elements. The distance and angle of orientation between the fire and the bridge, as well as any intervening barriers or structures, will influence the heat flux that is imparted to the structural elements.

What tools can be used to calculate the thermal impact of fire hazards on bridge structures?

Section 4 presents several common approaches that are used to model open-air fire hazards that impact bridges: (1) standard fire curves, (2) computational fluid dynamic (CFD) simulations, and (3) semi-empirical models based on a combination of experimental data and first-principle calculations. Semi-empirical models receive the most attention in this report since they are simpler to use than computationally intensive CFD models and provide significantly more detailed thermal exposure information than standard fire curves.

How can the thermal exposure from a design fire be quantified as structurally significant?

A structurally significant fire has sufficient intensity and proximity to the bridge such that the structural elements will be adversely impacted by the resulting thermal exposure. A risk-based method is proposed in this report via the following steps: (1) thermal-based damage assessment based on the type of primary structural elements; (2) development of structural damage influence zones based on the size of the fire; (3) quantification of fire frequency; and (4) calculation of thermal load (i.e., peak heat flux and fire duration) corresponding to a given reliability level. The details of these steps are presented in Sections 5 and 6 of this report, which includes a case study for demonstration.

1 INTRODUCTION

1.1 Recent history of bridge fire hazards

As shown in Figure 1-1, several surveys of bridge failures in the U.S. between 1980 and 2012 [3–5] have indicated that, as expected, common hazards such as flooding, scour, collision, deterioration, and overload cause the majority of bridge failures. Fire, however, causes failure at a rate comparable to or exceeding earthquakes and construction defects, both of which are addressed much more extensively in current practice via design, inspection, and mitigation. To date, fire exposure has typically received far less attention and fewer resources as a subject for bridge research and a hazard consideration for bridge design and retrofit than all other hazards shown in Figure 1-1.

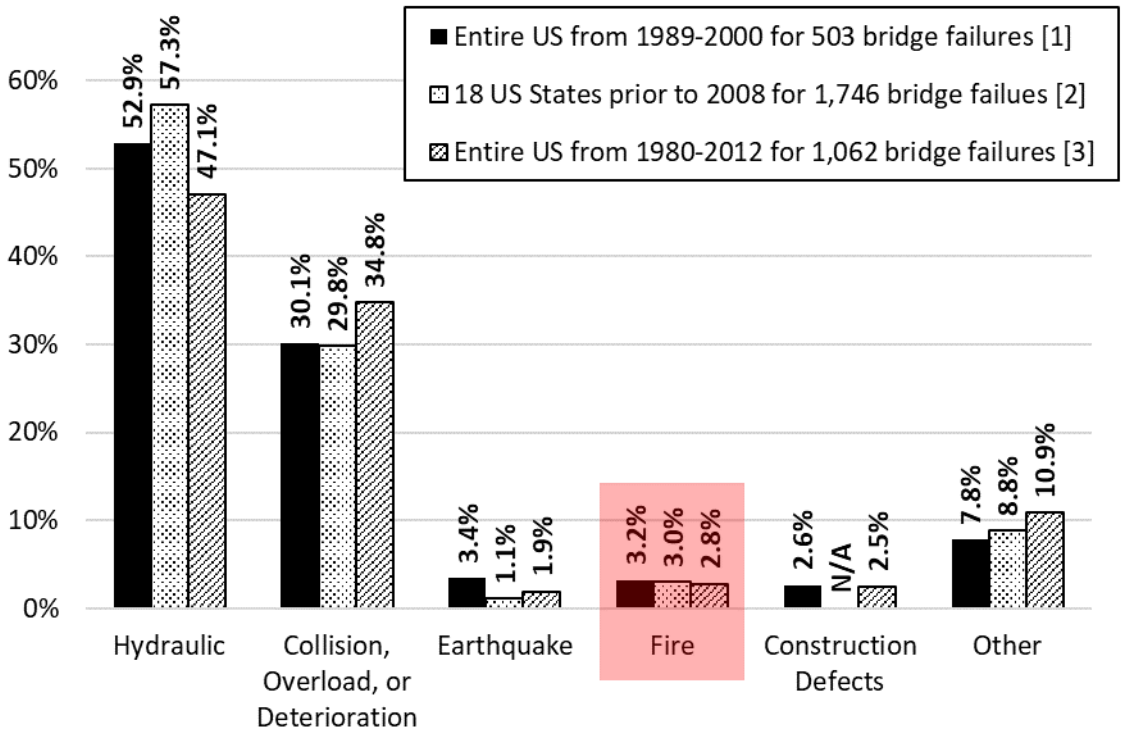

Figure 1-1: Chart. Percentages of bridge failures categorized by primary hazard per surveys of U.S. bridges.

A list of major fire incidents that have affected both steel and concrete bridges in the U.S. from 1995 to 2023 is tabulated in Table 1-1 through Table 1-4. The severity of bridge damage resulting from a fire hazard depends on the (1) fire intensity, (2) fire location relative to the bridge, and (3) bridge construction type. For instance, it is clear from Table 1-1 that the tanker fire or truck fire underneath the bridge is much more likely to cause severe bridge damage up to potential collapse. On the contrary, fire hazards on a bridge deck can cause relatively minor damage even when the tanker trunk is involved. Hence, these factors should be considered in a performance-based bridge fire analysis.

Table 1-1: Summary of major fire incidents for bridges in the U.S. from 1995-2005 [6–11].

Bridge/location	Date of fire incident	Fire source	Relative Location	Material type used in structural members	Damage description	Damage level
I-80W/I-580E ramp in Emeryville, CA	02/05/95	A gasoline tanker	Over	Steel girders + reinforced concrete slab	Deck, guard rail and some ancillary facilities were damaged	Minor
I-95 Chester Creek, PA	05/24/98	A gasoline tanker truck carrying 8,000 gallons crashed	Underneath	Steel girders + reinforced concrete slab	Steel girders were severely damaged and twisted due to fire	Heavy
37 Expressway near I-95, RI	07/20/00	A gasoline tanker truck carrying 1,000 gallons turned over	Over	Concrete girders+ reinforced concrete slab	The bridge girders severely damaged and eventually replaced	Heavy
I-80, Denville, NJ	06/24/01	A truck crashed	Underneath	Concrete girders+ reinforced concrete slab	Bridge girders were severely damaged and the bridge was replaced	Heavy
I-20/I-59/I-65 interchange in Birmingham, AL	01/05/02	A loaded gasoline tanker crashed	Underneath	Steel girders+ reinforced concrete slab	Main span of girders sagged about 3 meters (10 feet)	Collapse
Puyallup River Bridge, Olympic, WA	12/11/02	A tanker carrying 30,000 gallons of methanol crashed	Underneath	Precast prestressed I girders + cast in place reinforced concrete slab	Two columns and 15 girders were damaged and replaced	Heavy
I-95 Howard Avenue Overpass in Bridgeport, CT	03/26/03	A car struck a truck carrying 8,000 gallons of heating oil	Underneath	Steel girders + reinforced concrete slab	Collapse of the girders of southbound lanes and partial collapse of the northbound lanes	Collapse
I-95, Baltimore, MD	01/13/04	A truck crashed on the bridge and caught on fire	Over	Concrete girders+ reinforced concrete slab	Minor damage	Minor
I-75 Big Slough Canal, FL	02/03/04	A truck crashed underneath the bridge	Underneath	Steel girders + reinforced concrete slab	Minor structural damage	Minor
Bridge over the Norwalk River near Ridgefield, CT	07/12/05	A tanker truck carrying 33,000 gallons of gasoline	Underneath	Precast pre-stressed box girders + cast in place reinforced concrete slab	The deck was replaced, and its beams were tested by the FHWA	Heavy

Table 1-2: Summary of major fire incidents for bridges in the U.S. from 2006-2008 [6–11].

Bridge/location	Date of fire incident	Fire source	Relative location	Primary structural members	Damage description	Damage level
Belle Isle Bridge in NW Expressway, Oklahoma City, OK	01/28/06	A truck crashed into the bridge	Beside	Precast pre-stressed I girders + cast in place reinforced concrete slab	Concrete girders were slightly damaged by the fire. The safety of the bridge was assessed, and the bridge was reopened to traffic	Minor
Williams River bridge in Bill Williams, AZ	07/28/06	A tanker carrying 7,600 gallons diesel crashed on the bridge (fuel spilled)	Underneath	Precast pre-stressed I girders + cast in place reinforced concrete slab	Three concrete girders were damaged	Heavy
I-80/I-580/I-880 interchange in Oakland, CA	04/29/07	A gasoline tanker crashed	Underneath	Steel girders + reinforced concrete slab	Two spans of I-580 bridge girders collapsed	Collapse
Longfellow Bridge, Boston, MA	05/02/07	Debris	Underneath	Steel arch	No damage was reported	Superficial
Stop Thirty Road, State Route 386 Nashville, TN	06/20/07	A fuel tanker truck rear-ended a loaded dump truck	Underneath	Concrete hollow box girder bridge	The bridge sustained very little damage and traffic was reopened after minor repairs	Minor
Bill Williams River Bridge, AZ	06/20/07	A gasoline tanker over-turned	Underneath	Precast pre-stressed I girders + cast in place reinforced concrete slab	Concrete girders were damaged by the fire and subsequently repaired, but it was not necessary to replace any of the girders	Moderate
Tappan Zee Bridge, over Hudson River, NY	07/02/07	A car struck a tractor-trailer	Beside	Steel truss, cantilever type bridge	Minor structural damage	Minor
Big Four Bridge, Louisville, KY	05/07/08	Electrical problem of the lighting system	Beside	Steel truss bridge	Minor structural damage resulting in large amount of debris on the bridge	Minor

Table 1-3: Summary of major fire incidents for bridges in the U.S. from 2009-2017 [6–11].

Bridge/location	Date of fire incident	Fire source	Relative location	Primary structural members	Damage description	Damage level
I-10 Escambia Bay, FL	06/04/09	A truck crashed on the bridge	Over	Concrete girders + reinforced concrete slab	Minor damaged of the concrete deck	Minor
Manhattan Bridge, NYC, NY	07/08/09	A truck crashed on the bridge	Over	Suspension	No damage was reported	Minor
Bridge over I-75 near Hazel Park, MI	07/15/09	A gasoline tanker	Underneath	Steel girders + reinforced concrete slab	Complete collapse of the bridge to the freeway below	Collapse
Throgs Neck Bridge, NYC, NY	07/21/09	Construction fire	Underneath	Steel girders + reinforced concrete slab	Some steel girders were damaged	Heavy
I-10 Bayway in Mobile, AL	09/02/09	A truck crashed on the bridge and caught into fire	Over	Concrete girders	Minor damage of the concrete deck	Minor
Metro-North railroad bridge over Harlem River, NY	09/20/10	Explosion in power transformer caused burning of wood pilings	Underneath	Steel truss bridge	Minor structural damage of truss members	Minor
Bridge over State Route 60, Los Angeles, CA	12/14/11	A tanker truck carrying 8,000 gallons of gasoline	Underneath	Precast pre-stressed I girders + cast in place reinforced concrete slab	Concrete girders were damaged significantly by the fire. The bridge was demolished and replaced	Heavy
I-375 bridge over I-75 in Detroit, MI	05/24/15	A gasoline tanker carrying 9,000 gallons crashed over the bridge	Over	Steel girders + reinforced concrete slab	Concrete deck was damaged significantly by the fire. Also, the steel girders experienced some damage	Moderate
Liberty Bridge, Pittsburgh, PA	09/02/16	Burning of plastic piping	Underneath	Steel cantilever bridge	Intense heat had caused a 30-foot (9 m) steel beam (compression chord) to buckle	Heavy
Highway overpass on I-85 in Atlanta, GA	03/30/17	Combustion of 76 reels of high-density polyethylene conduit and nine racks of fiberglass conduit	Underneath	Pre-stressed bulb-T girder	Span 30 NB collapsed. Two adjacent spans were replaced	Collapse

Table 1-4: Summary of major fire incidents for bridges in the U.S. from 2018-2023 [6–11].

Bridge/location	Date of fire incident	Fire source	Relative location	Primary structural members	Damage description	Damage level
Brent Spence Bridge, I-71/75 over the Ohio River, Cincinnati, OH	11/11/20	Two semi-trucks caught collided and caught on fire	Underneath (Lower deck of double-deck truss)	Through truss with a suspended center span	Two spans of upper deck stringers and deck had to be replaced	Minor
I-95 highway overpass, Philadelphia, PA	06/11/23	A gasoline tanker carrying 8,500 gallons crashed over the bridge	Underneath	Steel girders + reinforced concrete slab	North bound bridge span collapse, adjacent south bound span replaced	Collapse

1.2 Existing specifications and research development

Fire is not explicitly addressed in the AASHTO Load Resistance Factor Design (LRFD) Bridge Design Specifications, 9th Edition[2] [2], nor is it in most bridge design manuals curated by state departments of transportation (DOTs) or other authorities having jurisdiction (AHJ). The most significant national reference addressing the design of bridges exposed to fire is provided by NFPA 502[1] Chapter 6 [1], which applies only to bridges more than 1,000 ft. (300 m) in length. However, most of the overpasses that have collapsed from 1995 through 2023 were shorter than 1,000 ft. (300 m) (as shown in Table 1-1). NFPA 502[1] Section 6.3 states that the primary structural elements of bridges or elevated highways shall be protected to achieve the following functional requirements: (1) support firefighter accessibility; (2) mitigate structural damage and prevent collapse; and (3) minimize the economic impact. The document states that an "engineering analysis," including the consideration of design fire scenarios and their proximity to the structure, is needed to determine whether the collapse of the bridge due to fire would have adverse impacts to life safety or other unacceptable implications. However, little information is provided regarding the available approaches and performance objectives for such an analysis.

1.3 Proposed framework

When fire events occur, local transportation authorities and national agencies become increasingly aware of the impact of fire on their bridge inventories. Complementing NFPA 502[1] Chapter 6 [1] with this report can help bridge designers and owners to make informed decisions about assessing the risk of the consequences from fire events based on the calculated response of the structural system to likely hazards. Though a wider range of methods are introduced, this study focuses on simpler design-basis tools that are computationally efficient and provide conservative evaluations of fire-induced behavior. The size and likelihood of the fire, its proximity to a given bridge, and the thermo-structural response of the bridge are considered in the approach. Fire hazards primarily focus on vehicle fires, though nearby material storage or other structures are also considered. The relative likelihood of vehicle fire hazards will consider proximity of the bridge to these hazards as well as the frequency or probability of their associated fires.

2 FIRE INTENSITY

Fire hazards that affect bridges are typically considered open-air, meaning that they are fuel-controlled and are assumed to have unlimited amounts of oxygen available for combustion (i.e., these fires are not ventilation controlled). Fires that are located underneath a bridge and are partially confined by the bridge superstructure overhead would still classify as an open-air fire since plenty of oxygen is available for combustion; although the fire and associated hot gases and smoke may directly impinge on the structural members. In this section, the intensity of design basis of open-air fire hazards is described in terms of peak heat release rate (HRR) (i.e., peak magnitude of the fire) and HRR time history (i.e., fire duration).

The fuel sources for fire potential design basis scenarios can include vehicles, hydrocarbon fuels (transported or stationary in storage), and other combustible solid fuels (also transported or stationary). NFPA 502[1] Chapter 6 (through the 2023 edition) [1] does not explicitly define any design fire scenarios for bridges. NFPA 502[1] Section A.6.3.2 suggests the following: (1) for bridges spanning moving traffic, the design fire scenario typically includes an HGV; and (2) for bridges spanning a freeway or interstate highway, the design fire scenario typically includes a flammable liquid tanker. No information is provided regarding the proximity of the bridge to the potential fire source or the intensity of fire exposure from that fire. This section directly addresses this need by developing a design basis for open-air fire scenarios. Note that per NFPA 502[1] Section 6.1.2, bridges or spaces under bridges that are fully enclosed and meet the definition of a tunnel per NFPA 502[1] Section 7.2 would instead be evaluated as a tunnel structure per NFPA 502[1] Chapter 7. The design basis provided in this report is not intended for bridge-like structural enclosures governed by NFPA 502[1] Chapter 7.

2.1 Peak heat release rate (HRR)

Determining the HRR of a design basis fire primarily depends on the combustion properties of the materials that are involved. For some widely studied fuels, such as liquid hydrocarbons, semi-empirical calculations can determine the HRR reliably using well characterized material properties. Fires that include vehicles or a combination of materials (such as tires, fabrics, plastics, computerized components, batteries, solid cargo, cellulosic material, or other combustible material) are more challenging to quantify due to uncertainties regarding actual quantity, combustion properties, and the ratio of fuel volume to exposed surface area. HRR calculations for these types of fires will rely more on an inventory method approach or the results of fire tests that examine the combustion of whole vehicles or a realistic combination of solid fuels.

2.1.1 Vehicle fires

Table A.11.4.1 in NFPA 502[1] Annex A [1] lists HRR values for several classes of vehicle fires, which are reproduced here in Table 2-1. These vehicle classes range from single passenger cars up to heavy goods vehicles (HGVs, which can carry a wide assortment of potential fuels) and tanker trucks carrying flammable liquids. Note that the design fire HRRs in the 2017 edition of NFPA 502[1] [12] increased compared to previous editions based on the inclusion of new experimental data. The specified HRRs in Table 2-1 apply to bridges as a starting point for developing a design basis fire intensity for vehicles on nearby roadways (especially for roads that pass underneath a bridge). Note that the data used to develop the HRRs in Table 2-1 were obtained from large-scale fire tests in laboratories and tunnels. Pending the availability of a similar compilation of open-air fire test results, the HRRs in Table 2-1 can provide an appropriate representation of design basis HRRs for vehicle fires that impact bridges.

Table 2-1: Peak heat release rates (HRR) for vehicle fires per NFPA 502[1] [1].

Vehicles	Experimental Peak HRR (MW)	Experimental Time to Peak HRR (min)	Representative Peak HRR (MW)	Representative Time to Peak HRR (min)
Passenger car[3]	5-10	0-54	8	10
Multiple passenger car	10-20	10-55	15	20
Bus	25-34	7-14	30	15
Heavy goods truck	20-200	7-18	150	15
Flammable tanker	200-300	-	300	-

As an alternative to Table 2-1, semi-empirical correlations between vehicle weight and associated fire HRR can be developed using the results of fire testing. For example, Guo et al. [15] developed a fit equation to correlate vehicle combustible mass, *m* (kg), with the fire's peak HRR, $\dot{Q}_{f,max}$ (MW), based on the results of fire tests summarized in Table 2-2 and Table 2-3:

$$\dot{Q}_{f,max} = \frac{a \cdot m}{b+m} \tag{2-1}$$

where the constants *a* and *b* have the values of 441.3 and 14,380, respectively [13]. The combustible mass for each vehicle type is assumed to vary from 30% of the vehicle tare weight to a maximum of the full payload capacity of the vehicle plus 30% of the tare weight. The combustible mass and corresponding $\dot{Q}_{max}$ for each generic type of vehicle per Guo et al. [13] are summarized in Table 2-4.

The total combustion energy E_{tot} (GJ) for vehicle fires could be calculated as a function of the peak HRR given the data in Table 2-3 and Table 2-4. The data used by Ingason [16] to develop the aforementioned tunnel fire design curves also utilized a different set of large-scale vehicle fire experiments and is used to generate an "upper bound" regression (E_{tot}^{up}, plotted with dashed line in Figure 2-1), while experimental data collated by Guo et al. [13] was used to develop a "lower bound" regression (E_{tot}^{low}, plotted with solid line in Figure 2-1):

$$E_{tot}^{up} = 3.31 \cdot \dot{Q}_{f,max}^{1.066} \tag{2-2a}$$

$$E_{tot}^{low} = 16.47 \cdot e^{0.01257 \cdot \dot{Q}_{f,max}} \tag{2-2b}$$

[3] Fire tests on passenger cars have historically been conducted on those with conventional internal combustion (gasoline or diesel) engines [13]. Recent fire tests by Sturm et al. [14] on electric vehicles powered by lithium ion batteries produced peak heat release rates that did not exceed the 10 MW upper bound per NFPA 502 [1].

Table 2-2: Summary of published data from vehicle fire tests for lower bound for total combustion energy estimation.

Combustible content involved	Estimated combustible weight (kg)	Theoretical calorimetric energy (GJ)	Peak HRR (MW)	Source
Car: Trabant Limousine	209	3.1	3.7	[17]
Car: Rover-Austin Metro LS	268	3.2	1.7	[17]
Car: Citroen BX 16RE	320	8	4.6	[17]
Pickup Truck: Wood Pallets	1937	26	24	[18]
Pickup Truck: Wood Pallets	1937	26	21	[18]
Pickup Truck: Plastic Barrels	1499	25	47	[18]
School bus with 40 seats	1565	41	29	[19]
HGV: Trailer + Furniture	3565	87	128	[19]
HGV: Trailer + Margarine	1965	35	23	[20]
Wood Pallets + Plastic Pallets	5460	99.2	150	[21]
Diesel	166.4	6.7	6	[22]
HGV: Wood Pallets + PE plastic pallets + Polyester Tarpaulin	11010	244	202	[22]
HGV: Wood Pallets + PUR Mattresses + Polyester Tarpaulin	6853	135	157	[22]
HGV: Furniture and fixtures + Rubber tires + Polyester Tarpaulin	8506	179	119	[22]
HGV: Wood Pallets + Corrugated paper cartons with interiors + Unexpanded polystyrene cups+ Polyester Tarpaulin	2849	62	66	[22]
10 HGV	71630	1500	370	[23]
14 HGV, 9 cars	102431	2145	380	[23]

Table 2-3: Summary of published data from vehicle fire tests for upper bound for total combustion energy estimation [16].

Combustible content involved	Theoretical calorimetric energy (GJ)	Estimated peak HRR (MW)
2-3 cars	17	8
Van	38	15
HGV: no "hazardous goods"	144	30
HGV: with high calorific potential	450	100
Tanker	960	200

Table 2-4: Representative combustible mass and peak HRR for common vehicle fires [13].

Vehicle types	Combustible Mass: Mean (kg)	Combustible Mass: Std. Dev. (kg)	Peak HRR: Mean (MW)	Peak HRR: Std. Dev. (MW)
Motorcycle	145	30	4	1
Car	1143	272	32	7
Pick-up Truck/Van	1977	514	52	11
Bus	9283	2748	170	23
HGV (2 Axle)	7923	2294	154	22
HGV (3 Axle)	12200	3545	199	23
HGV (4 Axle)	14803	4027	220	21
HGV (5 Axle)	16327	4535	231	21
HGV (6 Axle)	16327	4535	231	21
HGV (7 Axle)	16327	4535	231	21

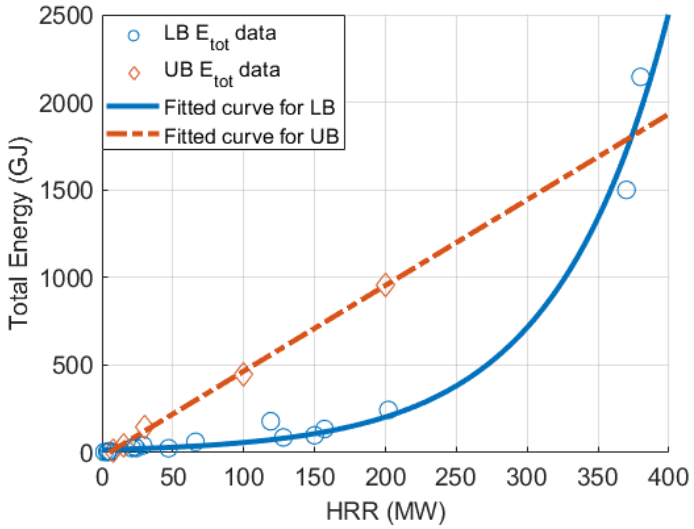

Figure 2-1: Graph. Estimated total combustion energy of vehicle fires with respect to HRR (upper bound, UB, per Ingason [16]; lower bound, LB, per Guo et al. [13]).

2.1.2 Hydrocarbon pool fires

As shown in Section 1, most of the severe bridge fire incidents from 1993 to 2023 have involved tanker trucks carrying large volumes of hydrocarbon fuel. Section 2.1.1 presents a representative HRR for a tanker truck, but methods exist to directly calculate the HRR of a hydrocarbon pool fire based on the fuel type, volume, and footprint. The pool footprint area and shape are associated with the fuel that is either contained within the tanker or spills onto the ground. Variables that affect the footprint area and shape include the assumed spill rate, the slope of the roadway, the presence of drainage, etc. For many fuel spills, a rectangular or trapezoidal footprint can account for sloping pavement in either one or two directions, respectively. The

footprint shape discussed here will focus on a rectangular shape for simplification. Note that the methods discussed here could also directly calculate the HRR of stationary storage tanks that contain liquid fuel.

Most of the available calculations for hydrocarbon pool fire characteristics are based on a circular pool footprint shape, which was used to generate the majority of pool fire test data in the published literature [24]. Similar expressions for non-circular pool fires are not widely available. Since the pool fire diameter, D_f (m), is a needed variable for most semi-empirical calculations, an effective diameter $D_{f,eff}$ (m) based on the equivalent area of the rectangular footprint can be obtained as follows:

$$if\ L_f/W_f \leq 2.5, D_{f,eff} = \sqrt{4 \cdot A_f/\pi} \tag{2-3a}$$

$$else, D_{f,eff} = \sqrt{4 \cdot 2.5 \cdot W_f^2/\pi} \tag{2-3b}$$

where A_f (m^2), L_f (m), and W_f (m) are the area, length (long edge dimension), and width (short edge dimension) of the rectangular pool fire footprint, respectively. These parameters are illustrated in Figure 2-2. Previous studies have indicated that using $D_{f,eff}$ for areas with aspect ratios greater than 2.5 may lead to inaccuracy when using the semi-empirical equations based on circular pools [25]. For rectangular fire footprints with an approximate aspect ratio (long edge to short edge) greater than 2.5, $D_{f,eff}$ is calculated by limiting the length to 2.5 times the width.

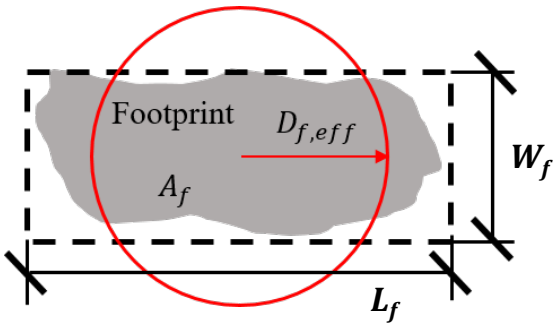

Figure 2-2: Illustration. Equivalent pool fire footprint.

The peak HRR $\dot{Q}_{f,max}$ of a hydrocarbon pool fire can be calculated as follows [26]:

$$\dot{Q}_{f,max} = \dot{m}''_{\infty} \cdot \Delta H_{c,eff} \cdot A_f \cdot (1 - e^{-\kappa\beta \cdot D_{f,eff}}) \tag{2-4}$$

where $\dot{m}''_{\infty}$ is the maximum mass loss rate per unit area (kg/m^2-sec), $\Delta H_{c,eff}$ is the effective heat of combustion (kJ/kg), and $\kappa\beta$ is an empirical coefficient (m^{-1}). The value of A_f for Eq. (2-4) is calculated as $\pi(D_{f,eff}/2)^2$, from the appropriate equation from Eq. (2-3). The values of these parameter are determined by the fuel type can be found in various reference manuals [26,27]. For example, gasoline has the following values: $\dot{m}''_{\infty}$ = 0.055±0.002 kg/m^2-sec; $\Delta H_{c,eff}$ = 43,700 kJ/kg, and $\kappa\beta$ = 2.1±0.3 m^{-1}.

2.1.3 Solid material fires: Inventory method

Beyond vehicle-based or hydrocarbon fuel fires, fire hazards for bridges can also include materials that are stored near, under, or on the bridge. For example, numerous reels of high-density polyethylene conduit that was stored underneath an I-85 overpass in Atlanta, GA caught fire in March 2017, causing the total collapse of the bridge span overhead [28]. A similar incident in November 2023 damaged overpasses on I-10 in Los Angeles, CA. As a result, the National Transportation Safety Board (NTSB) [29] and FHWA [30] both issued bulletins to raise awareness among bridge owners and designers regarding the concern of storing flammable materials underneath a bridge. As indicated in Table 1-1, the relative location of the potential fire hazard to the bridge is critical when identifying design basis fire scenarios. The summary in Section 1 identified that fire hazards underneath the bridge cause much more severe structural damage compared to fires located on the bridge deck.

The inventory method can calculate the total combustion energy of stored or stationary fuel sources. The total combustion energy is calculated by tabulating and summing the contributions of each material quantity to the combustion process. Inventory methods are widely accepted for estimating the fuel load for fire safety assessment of buildings [31,32]. This method was also applied for a study of a multi-span straight steel girder overpass bridge subjected to fire from a construction trailer underneath [33]. In that study, the total combustion energy was calculated as the summation of calorimetric energy for the quantity and type of combustion materials associated with a typical construction trailer, including the office housed inside. Table 2-5 provides a summary of the fuel constituents for the construction trailer from that study [33].

Due to natural combustion inefficiencies, not all the fuel load energy is converted into heat release. The peak HRR therefore is calculated using empirical expressions. For example, Ingason and Lonnermark [34] performed four large-scale fire tests in a tunnel on fuels ranging from wood pallets to furniture to corrugated paper cartons, with total fuel load ranging from 62 GJ to 247 GJ. These tests showed a range of peak HRR ($\dot{Q}_{f,max}$) per unit of fuel combustion energy from 0.85 MW/GJ to 1.15 MW/GJ. Another study by Lonnermark and Ingason [35] produced values of 0.5 MW/GJ to 1.2 MW/GJ for various types of burning vehicles including passenger cars and buses. For the study of the construction trailer fire scenario, an average value of 0.7 MW/GJ was used to represent the trailer and its contents. A similar approach could empirically convert total calorimetric energy of combustion materials to peak HRR when implementing an inventory method approach for other fuels whose fires may impact bridges.

Table 2-5: Example fuel load estimation for a typical construction trailer (adapted from [33]).

Component	Material	Length (m)	Width (m)	Thick. (mm)	Mass (kg)	Heat of Combustion (MJ/kg)	Fuel Load Energy (MJ)
Floor	OSB plywood	3.66	17.1	31.8	1,784	20.0	35,679
Floor	R20 fiberglass insulation	--	--	--	--	--	none
Floor	15.8-mm plywood decking	3.66	17.1	15.9	892	20.0	17,840
Walls	30G galvanized steel siding	--	--	--	--	--	none
Walls	9.5-mm plywood sheathing	41.5	4.11	9.50	1,462	20.0	29,244
Walls	R12 fiberglass insulation	--	--	--	--	--	none
Walls	Poly vapor barrier	--	--	--	--	--	none
Walls	Prefinished wood paneling	41.5	4.11	19.1	2,924	20.0	58,488
Roof	White PVC membrane	3.66	17.1	72.0	158	17.0	2,679
Roof	12.7-mm plywood sheathing	3.66	17.1	12.7	714	20.0	14,272
Roof	R20 fiberglass insulation	--	--	--	--	--	none
Roof	Poly vapor barrier	--	--	--	--	--	none
Roof	12.7-mm prefinished fiberboard	3.66	17.1	12.7	793	20.0	15,857
TOTAL					**8,727 kg**		**174,059 MJ**

2.2 HRR time history

The total amount of heat energy exposure for a bridge under fire is a function of the fire duration, including its growth, peak, and decay phases. The peak HRR addressed in Section 2.1 can be used to develop an HRR time history and calculate the total fire exposure and resulting temperature increase in the structural elements of a bridge. Most of the published approaches for developing HRR time histories focus on tunnel

fires and were developed using large-scale tests in tunnels and laboratories. The tunnel-focused expressions presented below can provide a generally conservative approximation of an open-air fire duration, which would not be expected to exceed a comparable tunnel fire duration due to increased availability of oxygen and a lack of confinement.

2.2.1 Linear curve for vehicle fires

Based on French tunnel design standards [16,36,37], the fire HRR can be assumed to have a linear growth rate, $\alpha_{g,L}$ (kW/s), from time zero to t_{max} (sec), followed by a constant peak HRR ($\dot{Q}_{f,max}$) value up to the time t_D (sec), after which the HRR begins a linear decay rate, $\alpha_{D,L}$ (kW/s), to zero at t_d (sec), which represents the total duration:

$$for\ 0 < t \le t_{max}, \qquad \dot{Q}_f(t) = \alpha_{g,L} \cdot t \tag{2-5a}$$

$$else, for\ t_{max} < t \le t_D,\ \dot{Q}_f(t) = \dot{Q}_{f,max}$$

$$else, for\ t_D < t \le t_d, \qquad \dot{Q}_f(t) = \dot{Q}_{f,max} - \alpha_{D,L} \cdot (t - t_D)$$

$$t_{max} = \frac{\dot{Q}_{f,max}}{\alpha_{g,L}} \tag{2-5b}$$

$$t_D = \frac{E_{tot}}{\dot{Q}_{f,max}} + t_{max} - \frac{\alpha_{g,L} \cdot {t_{max}}^2}{2 \cdot \dot{Q}_{f,max}} - \frac{\dot{Q}_{f,max}}{2 \cdot \alpha_{D,L}} \tag{2-5c}$$

$$t_d = t_D + \frac{\dot{Q}_{f,max}}{\alpha_{D,L}} \tag{2-5d}$$

where E_{tot} (kJ) is the total combustion energy. The parameters used in these equations are illustrated in Figure 2-3a. The rates of growth rate and decay differ according to the vehicle types, as summarized in Table 2-6. The example linear HRR time history curve for vehicle fire with peak HRR $\dot{Q}_{f,max}$ = 30 MW and total combustion energy E_{tot} = 144 GJ is shown in Figure 2-3a. The values of the linear growth and decay rates are chosen to be $\alpha_{g,L}$ = 50 kW/s and $\alpha_{D,L}$ = 16.7 kW/s, respectively.

Table 2-6: Vehicle input data for linear HRR time [16].

Type of vehicle	E_{tot} (GJ)	$\dot{Q}_{f,max}$ (MW)	t_{max} (min)	t_D (min)	t_d (min)	$\alpha_{g,L}$ (kW/s)	$\alpha_{D,L}$ (kW/s)
2-3 cars	17	8	5	25	45	27	6.7
1 van	38	15	5	35	55	50	12.5
1 HGV (no hazardous material)	144	30	10	70	100	50	16.7
1 HGV with high calorific potential (no hazardous material)	450	100	10	70	90	167	83
1 tanker (with hazardous material)	960	200	10	70	100	333	112

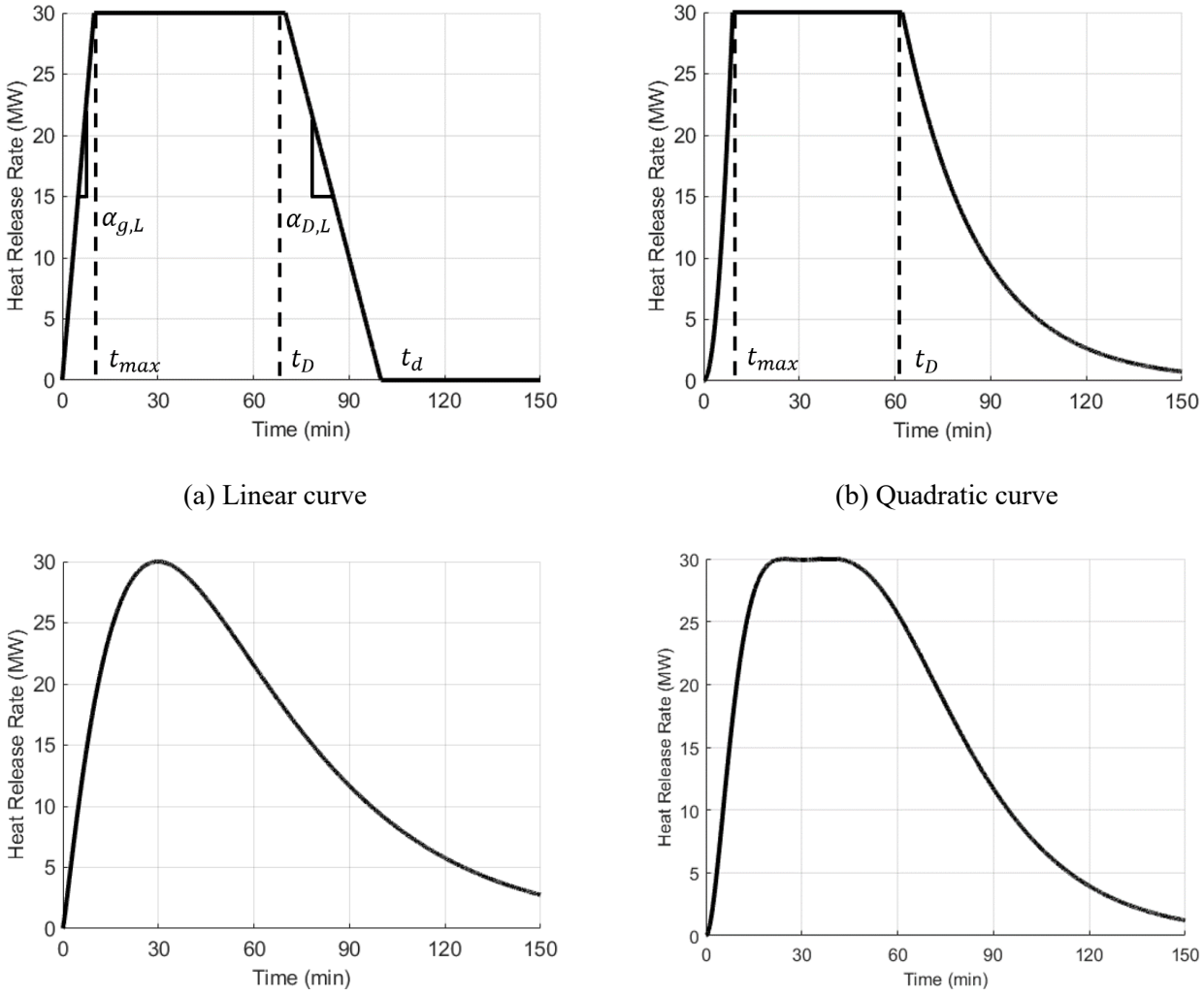

(a) Linear curve

(b) Quadratic curve

(c) Exponential curve

(d) Exponential curve with peak HRR plateau

Figure 2-3: Graphs. Example plots of HRR time history for a light HGV fire with $\dot{Q}_{f,max}$ = 30 MW and E_{tot} = 144 GJ.

2.2.2 Quadratic curve for vehicle fires

Ingason [16] proposed a time-dependent design fire curve for different types of vehicles with a quadratic growth from time zero to t_{max} (sec), a constant peak HRR ($\dot{Q}_{f,max}$) value to the t_D (sec), and an exponential decrease from the peak HRR value to zero. If $t_D \leq t_{max}$, then no constant peak HRR period is obtained.

$$\begin{aligned} &for\ 0 \leq t_{max}: && \dot{Q}_f(t) = \alpha_{g,q} \cdot t^2 \\ &else\ for\ t_{max} < t < t_D: && \dot{Q}_f(t) = \dot{Q}_{f,max} \\ &else\ for\ t \geq t_D: && \dot{Q}_f(t) = \dot{Q}_{f,max} \cdot e^{-\alpha_{D,q} \cdot (t - t_D)} \end{aligned} \tag{2-6a}$$

$$t_{max} = \sqrt{\dot{Q}_{f,max}/\alpha_{g,q}} \tag{2-6b}$$

$$t_D = \frac{\chi \cdot E_{tot}}{\dot{Q}_{f,max}} + \frac{2}{3} t_{max} - \frac{1}{\alpha_{D,q}} \tag{2-6c}$$

where χ is the combustion efficiency (conservatively taken as unity). The parameters used in the equations are illustrated in Figure 2-3b. The values of the growth rate ($\alpha_{g,q}$ in kW/s^2) and decay rate ($\alpha_{D,q}$ in s^{-1}) varies according to vehicle types (see Table 2-7). An example quadratic HRR time history curve for a light HGV fire per Table 2-6 with peak HRR $\dot{Q}_{f,max}$= 30 MW and total combustion energy E_{tot}=144 GJ is plotted in Figure 2-3b. Values for the growth rate $\alpha_{g,q}$ and decay rate $\alpha_{D,q}$ in this case taken as 0.1 kW/s^2 and 0.0007 s^{-1}, respectively, for a vehicle fire with $\dot{Q}_{f,max}$= 30 MW in Table 2-7.

Table 2-7: Design parameters for creation of design fire for traffic vehicles [16].

Type of vehicle	$\dot{Q}_{f,max}$ (MW)	$\alpha_{g,q}$ (kW/s^2)	$\alpha_{D,q}$ (s^{-1})
Car	4	0.01	0.001
Bus	30	0.1	0.0007
Truck*	15-130	-	-
Train	15	0.01	0.001
Subway car	35	0.3	0.001

*Since the fire load of a truck may vary greatly, no attempt was made to determine $\alpha_{g,q}$ and $\alpha_{D,q}$

2.2.3 Exponential curve for vehicle fires

Ingason [16] also proposed a method to estimate the HRR given as a single exponential function of time instead of three functions with sequential time intervals. This approach is only applicable to fuel-controlled fires and fires with a small or negligible constant peak HRR period. The inputs for this expression include the peak HRR ($\dot{Q}_{f,max}$) and the total calorific value (E_{tot}):

$$\dot{Q}_f(t) = \dot{Q}_{f,max} \cdot n \cdot r \cdot (1 - e^{-k \cdot t})^{(n-1)} \cdot e^{-k \cdot t} \tag{2-7a}$$

$$t_{max} = \ln(n)\,/k \tag{2-7b}$$

$$t_d = -\ln\,(1 - {\beta_d}^{1/n})/k \tag{2-7c}$$

where t_{max} (sec) and t_d (sec) are the time to reach the peak HRR and time to total fire duration respectively; the time width coefficient $k = \dot{Q}_{f,max}/E_{tot}$; amplification coefficient $r = (1 - 1/n)^{1-n}$; the ratio between the integrated energy and the total energy $\beta_d = E_{tot,t_d}/E_{tot}$ could arbitrarily vary between 0.95 and 1.00. The value of retard index *n* is estimated as follows:

$$n \approx 0.743 \cdot e^{2.9 \cdot \dot{Q}_{f,max} \cdot t_{max} \cdot E_{tot}} \tag{2-7d}$$

The example exponential HRR time history curve for vehicle fire with $\dot{Q}_{f,max}$ = 30 MW and E_{tot} = 144 GJ is shown in Figure 2-3c. The value of essential parameter *n* is chosen as 2.15.

0To represent the constant HRR period for steady-state liquid or wood crib fires, Ingason [16] derived an exponential curve with a plateau-shaped maximum period. Mathematically, it is a sum of two exponential curves:

$$\dot{Q}_f(t) = \dot{Q}_{f,max} \cdot (n_1 \cdot r_1 \cdot (1 - e^{-k_1 \cdot t})^{(n_1 - 1)} \cdot e^{-k_1 \cdot t} + n_2 \cdot r_2 \cdot (1 - e^{-k_2 \cdot t})^{(n_2 - 1)} \cdot e^{-k_2 \cdot t}) \quad (2\text{-}8a)$$

$$k_1 = \dot{Q}_{f,max} \cdot (r_1 + \eta \cdot r_2)/E_{tot} \quad (2\text{-}8b)$$

$$k_2 = \dot{Q}_{f,max} \cdot (r_1/\eta + r_2)/E_{tot}$$

$$n_2 = 7.17 \cdot {n_1}^{0.61} - 4.4 \quad (2\text{-}8c)$$

$$r_1 = 0.63 \cdot {r_2}^{2.28}$$

$$r_2 = (5.9 \cdot (n_1 \cdot r_1)^{0.66} - 3.54)/n_2$$

The value of n_1 arbitrarily varies between 2 and 10; r_2 is then solved by iteration, and n_2 and r_1 are then calculated. The example exponential HRR time history curve with plateau-shaped maximum period for vehicle fire with $\dot{Q}_{f,max}$ = 30 MW and E_{tot} = 144 GJ is shown in Figure 2-3d. The essential value n_1 was chosen as 3, and the value of η was estimated as 1.43 to obtain the constant plateau for the HRR curve.

2.2.4 Quadratic curve for hydrocarbon pool fire

Previously used in bridge fire studies by Quiel et al. [38], the HRR time-history curve for a hydrocarbon pool fire associated with a tanker truck spill can be expressed as a quadratic curve similar to that shown above in Section 2.2.2. The duration of the peak HRR ($\dot{Q}_{f,max}$) is calculated as the time t_b (sec) needed to consume fuel for combustion over the pool area (i.e., the "burn" time), A_f (m^2). The total time history of peak HRR is expressed as follows:

$$for\ 0 < t \le t_g, \dot{Q}_f(t) = \dot{Q}_{f,max} \cdot (t/t_g)^2 \quad (2\text{-}9a)$$

$$else\ for\ t_g < t \le (t_g + t_b), \dot{Q}_f(t) = \dot{Q}_{f,max}$$

$$else\ for\ (t_g + t_b) < t \le, (t_g + t_b + t_d), \dot{Q}_f(t) = \dot{Q}_{f,max} \cdot e^{-4 \cdot (t - t_g - t_b)/t_d}$$

$$t_b = \frac{\rho \cdot V_{fuel}}{\dot{m}'' \cdot A_f} \quad (2\text{-}9b)$$

where t_g (sec) is the time of fire growth (taken as the minimum of $t_b/5$ or 600 sec), t_d (sec) is the time of decay (taken as the minimum of t_b/2.5 or 1,200 sec); V_{fuel} (m^3) is the combusted fuel volume; ρ (kg/m^3) is the density of specific fuel; and $\dot{m}''$ (kg/m^2-sec) is mass loss rate per unit area related to both the fuel type and the equivalent diameter the footprint ($D_{f,eff}$). The mass loss rate per unit area, $\dot{m}''$ was introduced in Section 2.1.2, and is expressed as follows:

$$\dot{m}'' = \dot{m}''_{\infty} \cdot (1 - e^{-\kappa\beta \cdot D_{f,eff}}) \quad (2\text{-}10)$$

Again, the values of these two parameters for common hydrocarbon fuels are readily available in the published literature [26,27]. Note that reducing V_{fuel} can account for fuel lost due to drainage, runoff, absorption, evaporation, etc. during a fuel spill that leads to a subsequent fire. Figure 2-4a illustrates the HRR time history for gasoline pool fire with the footprint area of 20 m^2 (diameter = 5 m) and the volume of fuel for combustions of 3.78 m^3 (1,000 gallons).

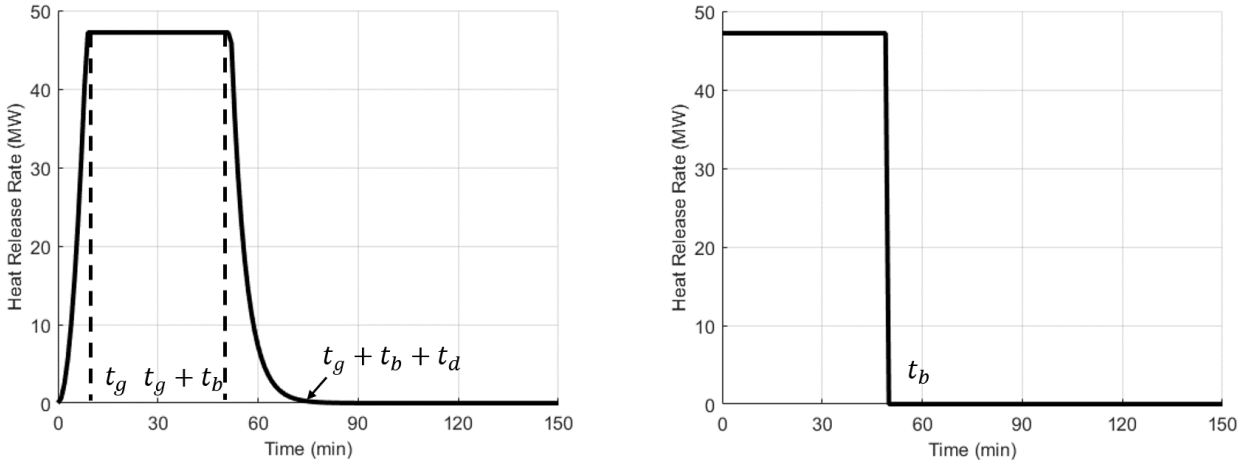

(a) Quadratic Curve (b) Simplified curve

Figure 2-4: Graphs. Example HRR time histories for a circular gasoline pool fire with A_f = 20 m^2 and V_{fuel} = 3.78 m^3.

2.2.5 Simplified approach

For simplification, the HRR time history can be expressed as having the peak HRR over a calculated duration time, thus neglecting the growth and decay phases. Though this approach does not represent the realistic ignition and decay of an actual open-air fire, it is straightforward and can provide an adequate estimation of total exposure for large fires, for which the growth and decay phases are typically much shorter than the duration of peak HRR. The duration of the fire depends on the type, volume, and exposed surface area of the fuel. The duration of the fire t_D can be calculated for the linear or quadratic vehicle fires (per Sections 2.2.1 or 2.2.2); or t_b can be calculated from the quadratic hydrocarbon pool fire equation (per Section 2.2.4). An illustration of the simplified HRR curve for a hydrocarbon pool fire (using the same example as in Section 2.2.4) is shown in Figure 2-4b. Alternatively, relevant fire test data in the published literature for a fuel source and quantity of interest could also be used to approximate the fire duration.

3 FIRE MODELING

To quantify fire exposure to structural elements, the analyst considers the proximity and orientation of an affected bridge to the fire resulting from a given fuel source. The HRR magnitude and time history of a design basis fire can provide input for calculating the resulting heat energy exposure to a nearby bridge. Flames and smoke are generated from the localized source of fuel (one or more vehicles, or a specified quantity of liquid or solid fuels with a given area footprint) and can subject the bridge elements to heat exposure via radiative emission from the flames and smoke, convection from hot gas and smoke, and direct flame impingement. The magnitude of this heat exposure is a function of the fire geometry (particularly the flame height and footprint area and shape), its HRR, and fuel type as well as the standoff and orientation of the heated target to the fire. Methods for calculating heat exposure from large fire hazards generally include computational fluid dynamics (CFD) modeling [39–43] and semi-empirical fire models [33,38,44,45]. Each of the methods is introduced in the following sections. The temperature increases of a bridge's primary structural elements due to the total calculated fire exposure will then determine its resulting structural response.

3.1 CFD modeling

CFD software packages, such as the Fire Dynamics Simulator (FDS) developed at the National Institute of Standards and Technology (NIST) [46], are often used to model tunnel fires [47–50] and were used in several studies to examine fire effects on bridges [39,41]. CFD models numerically solve a form of the Navier-Stokes equations appropriate for low-speed, thermally-driven flow with an emphasis on smoke and heat transport from fires. The model needs a sufficiently large volume and is discretized for a given fire size. "Open" boundaries are specified at the edges of the computational domain (except for the ground) with adequate distance from the fire so that its behavior is not artificially influenced by fluid flow that exits the domain. CFD models can account for both convective and radiative heat transfer from open-air fires, which is represented using either a specified HRR over a footprint (or "burner vent") area or by explicitly modeling the combustion reaction of the fuel. Measurements of radiative and convective heat flux from the fire and the temperature at the location of the structural member need the placement of appropriate devices within the model. CFD models can accommodate a wide range of standoffs. However, the volume of the model (and the computational size via volumetric discretization) will markedly increase with larger standoff distance between the fire and the target structure.

Some of the significant parameters to consider for the open-air bridge fire simulation in NIST's FDS software package are summarized in Table 3-1. For example, the "gray gas" assumption (i.e., the gas has an average absorption coefficient over the whole spectrum of radiation [51]) is more applicable in the Finite Volume Method (FVM) for radiative heat transfer in FDS over the "wide band" model for large fires that produces significant soot production. FDS solves the radiation transport equation by calculating radiation intensity over a discrete number of solid angles. The default value of 100 solid angles can provide adequate resolution for targets near a localized source of thermal radiation but can produce a sparse or non-uniform distribution of radiation energy on targets at further standoff (called the "ray effect" [52]). This issue can be mitigated by increasing the number of solid angles, but computing times will correspondingly increase. Several turbulence parameters will influence the behavior of the fire if wind is considered. For example, a large Smagorinsky constant adds an artificial viscosity to the flow, which mitigates the flow of hot gases

around solid objects. Within the turbulence model, the Prandtl and Schmidt numbers determine the thermal conductivity of the turbulent flow and the diffusivity of the airborne materials within that flow, respectively.

Table 3-1: Generalized summary of major input parameters for CFD simulation.

Categories	Parameters
Fuel Characteristics	Fuel type Chemical formula CO yield (g/g) Soot yield (g/g) Footprint dimension
Volumetric Meshing	Mesh grid dimensions (m)
Radiation Parameters	Radiation model Solid angle Polar angles Radiative source temperature (°C) Angle increment, f_n
Turbulence Parameters	Smagorinsky constant Prandtl number Schmidt number
Simulation Parameters	Total time period (sec) Time step increment, f_t FDS version

In summary, CFD analyses are robust and generate significant levels of numerical resolution. However, CFD analyses are also computationally expensive and are not necessarily practical in many applications for limited budgets and critical schedules. CFD modeling approaches used to analyze fire exposure for bridges become increasingly useful implementing experimental validation, where possible, or by engaging the relevant expertise needed to set up, execute, and post-process this type of model. Performing sensitivity studies that examine modeling parameters such as those listed in Table 3-1 help establish confidence in the resulting heat transfer predictions from open-air fires affecting bridge structures.

3.2 Semi-empirical fire models

Previous studies have also modeled open-air fires that affect bridges using semi-empirical analytical calculations of the fire characteristics (e.g., height, heat release rate, duration, and radiative intensity) [33,38,44]. The results of these models can estimate heat transfer (primarily in the form of radiation) from the fire to the structural elements. These approaches are less computationally intensive than CFD solutions and allow for using the fire intensity from Section 2 (HRR magnitude and time history) as input for calculating fire exposure to a nearby bridge. Due to their efficiency, these approaches offer the potential for conducting a parametric study of the many uncertainties in the fire scenario, which include the footprint shape and area (which will depend on the vehicle size, spill characteristics of a hydrocarbon fuel, or the layout of other stationary fuel sources) and the location of the fire relative to the bridge.

Figure 3-1 illustrates several common semi-empirical models for open-air fires: (a) point source (PS) [53], (b) modified point source (MPS) [24], (c) solid flame (SF) [53–55], (d) modified solid flame (MSF), and (e) modified discretized solid flame (MDSF) [24,33,56]. A point, a cylinder, or other geometric shapes can represent the fire footprint and height. By assigning the emissive power to the object and calculating the view factor (how the target could "see" the fire hazard), the radiative heat flux emission is calculated. The existing fire models with the scope of their applications for bridge fire analysis are summarized in Table 3-2. Generally, for a fire scenario located alongside the bridge, the calculation of radiative heat flux is sufficient since the structure will not trap or block the rising smoke and hot gas. When the fire is underneath the bridge, convection from engulfment of smoke and hot gas, and potential flame impingement is considered. The MDSF model is capable of accounting for both radiative impact and convection results from smoke and hot gases impinging the bridge superstructure.

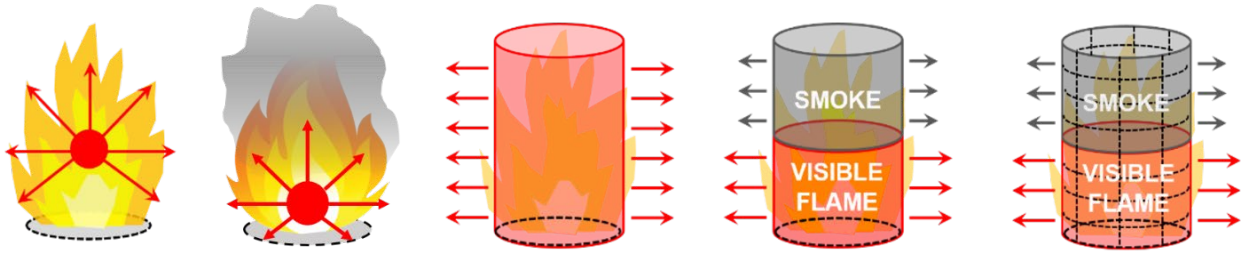

Figure 3-1: Illustrations. Analytical semi-empirical models for calculating heat flux from hydrocarbon pool fires.

Semi-empirical models and corresponding expressions are generally developed based on experiments on hydrocarbon pool fires with circular footprints. Hydrocarbon pool fires with equivalent HRR can represent more simplistically the fire scenarios with vehicles and other fuels rather than explicitly modeling the aggregate combustion of the various materials. Semi-empirical predictions of the intensity and geometry of hydrocarbon pool fires are well established from decades of previous research, and combustion properties for these fuels are readily available in the published literature. For example, a previous study by Guo et al. [47] used the equivalent footprint of a diesel pool fire to provide the same HRR as an actual vehicle and/or cargo fire. The rectangular footprint of the equivalent diesel pool fire was scaled from the vehicle footprint to obtain the same HRR as the pre-defined vehicle fire scenario. This equivalency to a hydrocarbon pool fire with a circular footprint is often needed when using most of the currently available semi-empirical models, which explicitly rely on input parameters associated with hydrocarbon fuel combustion characteristics. More experimental research is needed to enable a direct calculation of fire behavior from the combustion of other flammable materials or a combination of flammable materials.

Table 3-2: Generalized summary of semi-empirical and CFD fire modeling methods.

Fire modeling methods	Heat transfer modes	Fire Source	Comments
Point Source (PS)	Radiative heat flux	Any combustion materials	Generally suitable for larger standoff distances; used at any orientation to targets
Modified Point Source (MPS)	Radiative heat flux	Hydrocarbon pool fire*	Can accommodate closer standoff distances versus PS; used at any orientation to targets
Solid Flame Model (SFM)	Radiative heat flux	Hydrocarbon pool fire*	Generally suitable for larger standoff distances; only used for horizontal standoffs
Modified Discretized Solid Flame (MDSF)	Radiative and convective heat flux	Hydrocarbon pool fire*	Can accommodate any standoff distance, including direct engulfment; used at any orientation to targets
Computational Fluid Dynamics (CFD) Models	Radiative and convective heat flux	Any combustion materials	Can accommodate any standoff distance, including direct engulfment; used at any orientation to targets

*Note: Fire modeling for other flammable materials can be performed using a hydrocarbon pool fire with an equivalent HRR and footprint area.

3.2.1 Point source models

The PS model is among the simplest analytical methods for calculating radiation heat transfer from hydrocarbon pool fires to targets located outside the fire. Implementing the PS model involves the following steps: (1) determine the type of hydrocarbon fuel, and pool fire footprint size; (2) calculate the flame height, H_f, and select a vertical location for the point source emitter; (3) assign radiative power to the point source; and (4) calculate the radiation heat transfer via a closed-form expression that accounts for the distance and angle of orientation to the target. Following the calculation of the HRR and equivalent footprint of the pool fire, the flame height H_f can be calculated using one of several semi-empirical expressions that are available in the current literature, such as Heskestad's correlation [57]:

$$H_f = 0.235 \cdot \dot{Q}_{f,max}^{0.4} - 1.02 \cdot D_{f,eff} \tag{3-1}$$

where $\dot{Q}_{f,max}$ (kW) is the peak HRR per Eq. (2-4), and $D_{f,eff}$ (m) is the effective fire diameter per Eq. (2-3a).

In conventional PS model approaches, the point source is typically located at the geometric center of the three-dimensional fire shape. For a circular pool fire the PS is located at H_f /2 directly above the center of the circular footprint as presented in Figure 3-2a. The incident radiative heat flux experienced by a target located outside the pool fire footprint, $\dot{q}''$(kW/m^2), is calculated as follows:

$$\dot{q}'' = \frac{\chi_{r,ps} \cdot \dot{Q}_{f,max} \cdot \cos\theta}{4 \cdot \pi \cdot R^2} \tag{3-2}$$

where θ indicates the angle between the normal vector of the exposed target surface and the line of sight from the target to the point source location; R (m) is the length or "radius" of the line of sight from the point source to the center of the target surface, these geometrical parameters are explained with Figure 3-2a; and $\chi_{r,ps}$ is the point source radiative fraction. SFPE Handbook Chapter 66 [53] provides the following expression for $\chi_{r,ps}$:

$$\chi_{r,ps} = 0.21 - 0.0034 \cdot D_{f,eff} \tag{3-3}$$

The radiative fraction is a semi-empirical value was previously studied [53,58] based on a fit with experimental measurements of radiant heat flux from a wide range of hydrocarbon pool fires. Depending on the application, alternate expressions for χ_r as a function of pool diameter can also represent a single emissive power value for the entire fire for PS calculations. One prominent example is the expression for χ_r proposed by McGrattan et al. [58]:

$$\chi_r = 0.35 \cdot e^{-0.05 \cdot D_{f,eff}} \tag{3-4}$$

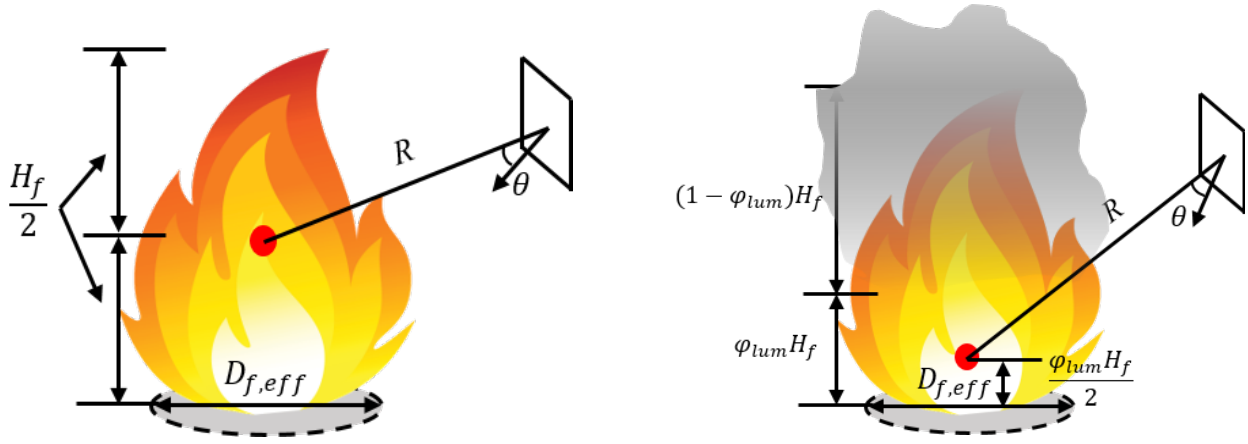

(a) Conventional point source (b) Modified point source

Figure 3-2: Illustrations. Heat transfer for (a) conventional point source model and (b) modified point source model.

3.2.2 Modified point source model

Placing the vertical location of the point source emitter at the half-height of the luminous zone, as shown in Figure 3-2b, can better capture the effects of smoke obscuration and the presence of the luminous zone in the lower portion of the fire. This location is calculated for gasoline and diesel pool fires as $(\varphi_{lum} \cdot H_f)/2$ above the ground. The value of φ_{lum} is obtained from Table 3-3 [59]. The radiative heat flux, $\dot{q}''$(kW/m^2), from the point source to a target surface is then calculated as follows:

$$\dot{q}'' = \frac{\chi_{r,mps} \cdot \dot{Q}_{f,max} \cdot \cos\theta}{4 \cdot \pi \cdot R^n} \tag{3-5}$$

where $\chi_{r,mps}$ is the radiative fraction for this modified point source (MPS) model. The MPS radiant heat flux predictions that utilize the radiative fraction proposed by McGrattan et al. [58] ($\chi_{r,mps} = \chi_r$ from Eq.(3-4)) generally compare well with experimental data and CFD simulations [24]. The exponent *n* applied to radius *R* in Eq. (3-5) is assigned a value of 2.2 based on calibration with the CFD results and experimental data to slightly reduce the calculated thermal radiation on targets at most standoffs while increasing it at very small standoffs. Again, using a value of $n = 2$ (thus reverting to Eq. (3-2)) would provide a conservative prediction for most standoffs (i.e., for $R > 1$ m). Also, note that the distance *R* from the point source to the target is different between the PS and MPS models for the same horizontal standoff distance *X* (measured from the center of the pool) due to the revised height of the point source location.

3.2.3 Conventional solid flame models

SFPE Handbook Chapter 66 [53] outlines two conventional solid flame (SF) models for calculating radiant heat flux from pool fires: Shokri and Beyler's Detailed Method (SBDM) and the Mudan and Croce Method (MCM). Both methods are implemented with the following steps: (1) determine the hydrocarbon fuel type and pool fire footprint size; (2) calculate the flame height, H_f; (3) calculate the view factor of the three-dimensional SF shape to the target via closed-form expression; (4) calculate emissive power of the SF shape; and (5) calculate the radiation heat transfer by multiplying emissive power with the view factor. The SBDM calculates H_f using Heskestad's correlation as presented in Eq. (3-1). For the MCM, H_f is calculated using the semi-empirical expression proposed by Thomas [60] (shown here for no wind tilt):

$$H_{f,MCM} = 42 \cdot [\dot{m}''_{\infty}/(\rho_a \cdot (g \cdot D_{f,eff})^{0.5})]^{0.61} \tag{3-6}$$

where ρ_a (kg/m^3) is the ambient air density, and g (m/s^2) is the gravitational acceleration.

Both the SBDM and MCM are formulated for cylindrical shapes with constant emissive power over their surfaces. The radiant heat flux experienced by a target located outside the pool fire is calculated as follows:

$$\dot{q}'' = E \cdot F_{12} \tag{3-7}$$

where E (kW/m^2) is the effective emissive power of the SF shape and F_{12} is the view factor from the fire to the target. Depending on the orientation of the target, the view factor can be $F_{12,V}$ for vertically oriented targets and $F_{12,H}$ for horizontally oriented targets as illustrated in Figure 3-3. These view factors are calculated as a function of the target location, orientation, and the SF geometry. As the target moves closer to the flame, the view factor approaches unity. The equations for $F_{12,V}$ and $F_{12,H}$ can be found in SFPE Handbook Chapter 66 [53] and are not reproduced here for brevity.

The derivation of F_{12} assumes that the target is horizontally aligned with the bottom or top of the cylinder (i.e., target locates at the bottom for the upper cylinder and locates at the top for the lower cylinder as in Figure 3-3). For targets at ground level or at a height equal to H_f, only one cylinder with the full flame height is needed and F_{12} will equal $F_{12,V}$ or $F_{12,H}$ with $H = H_f$. If the target's vertical location is between ground level and H_f, the overall SF cylinder is divided into two sub-cylinders at the target height, and the overall view factor F_{12} is the sum of their view factors (i.e., $F_{12,H1} + F_{12,H2}$ or $F_{12,V1} + F_{12,V2}$) when calculated with H_{f1} and $H_{f2} = H_f - H_{f1}$ as illustrated in Figure 3-3.

The effective emissive power of the SBDM model, E_{SBDM} (kW/m^2), is calculated using a fit equation of experimentally measured radiant heat fluxes from pool fires to external targets [55]:

$$E_{SBDM} = 58 \cdot (10^{-0.00823 \cdot D_{f,eff}}) \tag{3-8}$$

The effective emissive power of the MCM model, E_{MCM} (kW/m^2), is calculated as a weighted average of the luminous and smoke zone emissive power [54]:

$$E_{MCM} = E_{max} \cdot e^{-S \cdot D_{f,eff}} + E_s \cdot (1 - e^{-S \cdot D_{f,eff}}) \tag{3-9}$$

where E_{max} is the flame emissive power (taken as 140 kW/m^2); E_s is the emissive power of smoke (taken as 20 kW/m^2); and S is the extinction coefficient (0.12 m^{-1}) [53].

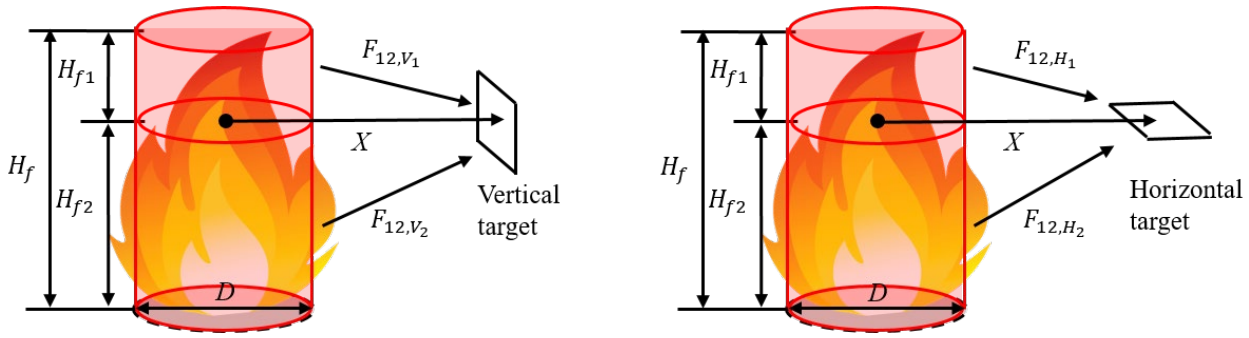

(a) Vertical target orientation

(b) Horizontal target orientation

Figure 3-3: Illustrations. Heat transfer for conventional solid flame models.

3.2.4 Modified discretized solid flame (MDSF) model

Calculating radiation heat transfer via the MDSF model also involves five steps: (1) determine the hydrocarbon fuel type and pool fire footprint size; (2) calculate fire geometry, particularly the overall flame height and the layering of luminous flame and smoke zones; (3) assign emissive powers that correspond to each zone; (4) apply an appropriately small mesh discretization to the flame and smoke surfaces (which will need an initial sensitivity analysis); and (5) calculate the radiation heat transfer as a summation of contributions from each discretized surface per its individual emissive power and view factor to the target. Quiel et al. [38] previously utilized a conservative formulation of the MDSF model in which the total height of the fire was vertically halved into the luminous and smoke zones, each of which was assigned a constant emissive power. The sections that follow present a brief review of this "first generation" MDSF model, followed by improvements in solid flame geometry and emissive power distribution for the "second generation" MDSF$_2$ model.

The flame height H_f for all MDSF models is calculated using Heskestad's correlation [57] per Eq. (3-1), and the surfaces of the extruded three-dimensional solid flame shape is discretized into radiation-emitting elements. Sizing of the surface element mesh should be determined via preliminary convergence analyses for the target standoffs of interest. Generally, the maximum discretized edge dimension is generally taken as 1% of the footprint perimeter, resulting in approximately square elements with 0.3 m maximum

dimension for a 10-m diameter circular fire. Each surface element i is assigned an emissive power, E_i (kW/m^2), based on its vertical location. As shown in Figure 3-4, the first generation MDSF represents a gasoline or diesel pool fire (which, like most hydrocarbon fuels, have significant soot yield when burning [61]) as vertically halved into a luminous visible flame lower zone and a smoke obscured upper zone. The shape of the footprint is either rectangular or circular as needed. This approach is a conservative simplification from previous experimental observations [54,62], which indicated that the luminous zone thickness for these fuels is typically less than half the total flame height.

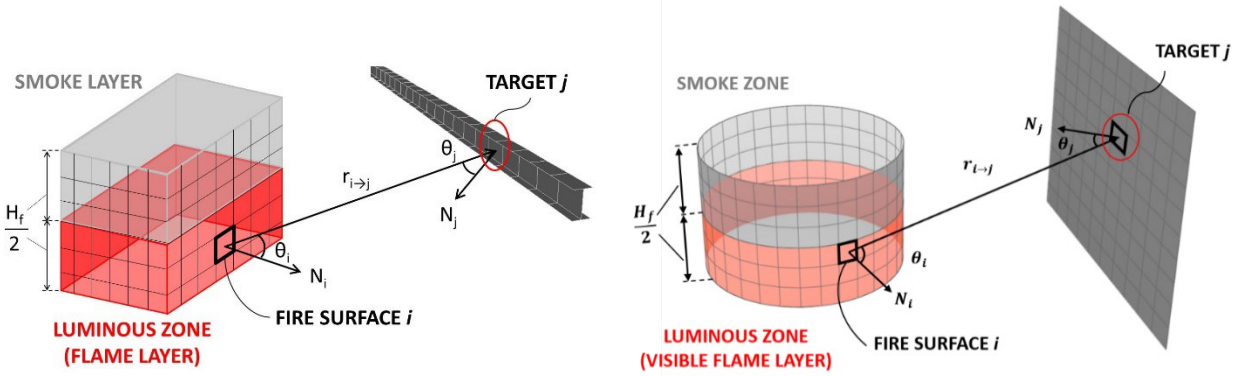

(a) Rectangular footprint (b) Circular footprint

Figure 3-4: Illustrations. Heat transfer from the first generation MDSF model [63] of an open-air hydrocarbon pool fire to a discretized target.

The emissive power of the visible flame zone, E_{flame}, and smoke obscured zone, E_{smoke}, are obtained directly from experimental literature or calculated based on semi-empirical expressions [53]. From experimental observations [62,64], values of E_{flame} approximately range from 80 to 140 kW/m^2 and values of E_{smoke} approximately range from 10 to 40 kW/m^2 are generally used depending on the fuel type and pool size. In a previous study of gasoline pool fires, Quiel et al. [38] used constant values of 100 kW/m^2 and 40 kW/m^2 for E_{flame} and E_{smoke}, respectively, as conservative approximations. The radiant heat flux from the MDSF model to a target j, $\dot{q}_j^{"}$(kW/m^2), located outside the pool fire is calculated as the summation of each discretized fire surface emissive power times the dimensionless view factor, $F_{i\to j}$, from that surface to the target:

$$\dot{q}_j^{"} = \Sigma_{i=1}^{n} E_i \cdot F_{i\to j} \tag{3-10a}$$

$$F_{i\to j} = \frac{A_i \cdot cos\theta_i \cdot cos\theta_j}{\pi \cdot r_{i\to j}^2} \tag{3-10b}$$

where E_i (kW/m^2) and A_i (m^2) are the emissive power and the area of the i^{th} element on the fire surface, respectively; $r_{i\to j}$ is the distance or "radius" from the center of fire surface element i to target j; θ_i represents the absolute angle between the radius vector and the fire element's normal vector; and θ_j is the absolute angle between the radius vector and the normal vector of the target surface. Fire surfaces with no view of the target impart no radiant heat flux. Targets that fall within the extruded fire shape (i.e., "engulfed" by the flames and smoke) are assigned a direct heat flux value based on experimental observation [33,38].

Choosing a value of 170 kW/m^2 in the luminous zone is in accordance with the value provided in SFPE handbook [65] as well as an experimental study of heat flux on objects engulfed in large hydrocarbon pool fires by Russell and Canfield [66]. The heat flux for targets engulfed in the smoke-obscured zone is modeled as decreasing linearly from 170 kW/m^2 at the top edge of the luminous zone to E_{smoke} at the top of the smoke layer. This approach is conservative since it assumes a high intensity of direct heat flux to engulfed elements over the full footprint and height of the fire.

To improve the spatial distribution and intensity of predicted radiant heat flux based on experimental observations, the "second generation" MDSF$_2$ model (Figure 3-5a) consists of two three-dimensional objects that together are more representative of realistic pool fires [67–71]: a flame cylinder-plus-cone (which is assigned a constant emissive power over its surface), and a smoke cylinder plus cone "hat" which obscures the top portions of the flame shape.

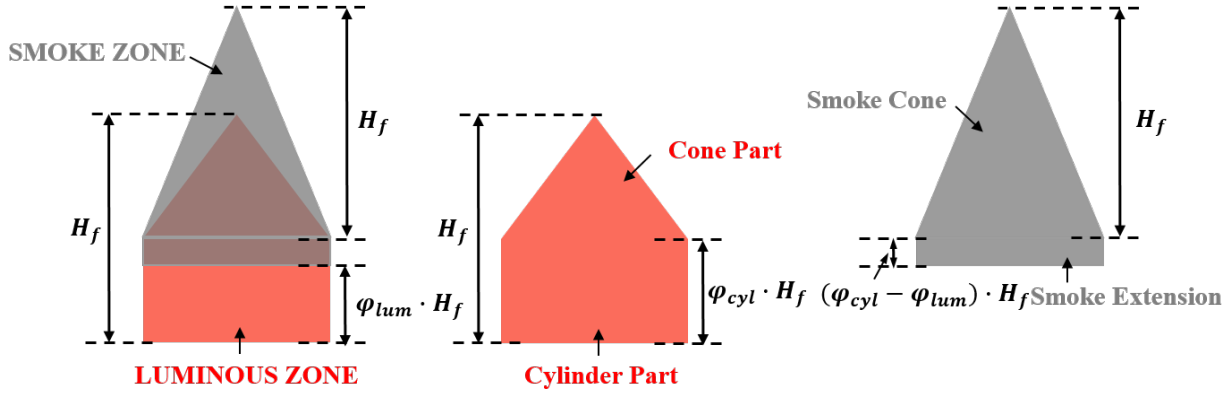

(a) Proposed MDSF$_2$ model (b) Solid Flame Shape (c) Smoke Hat

Figure 3-5: Illustrations. Flat elevation of the proposed MDSF$_2$ model with a circular footprint (shown without mesh discretization for clarity) [24].

Based on previous work by Zhou et al. [72] and Shen et al. [73], the geometry of the flame shape in Figure 3-5b has a total height H_f per Eq. (3-1). Zhou et al. [72] proposed a constant value of $0.4H_f$ for the height of the cylinder based on the results laboratory-scale pool fire tests with heptane [74]. Shen et al. [73] utilized a semi-empirical expression that calculates the cylinder height relative to the pool fire diameter based on laboratory-scale tests with natural gas flames [75]. In this study, the height of the cylinder is set equal to the maximum luminous zone height based on experimental observations for the selected fuel. For example, previous experiments by Munoz et al. [62] indicated that for pool diameters less than 5 m, the luminous zone is located below $0.45H_f$ for gasoline pool fires and $0.30H_f$ for diesel pool fires. Based on these observations, the assigned values of φ_{cyl} in Figure 3-5b for gasoline and diesel are 0.45 and 0.30, respectively, for all pool diameters. More experiments are needed to determine φ_{cyl} values for other types of hydrocarbon fuel. In the absence of experimental data, the cylinder heights proposed by Zhou et al. [72] or Shen et al. [73] could provide alternatives.

The smoke hat is positioned such that the base of its cone aligns with the base of the flame cone (at $\varphi_{cyl} \cdot H_f$) as shown in Figure 3-5a. The height of the smoke hat's cone equals H_f, which correlates with experimental data and FDS results. The smoke hat's cylinder extends downward from the base of its cone to obscure a portion of the flame cylinder according to experimental observations. In Figure 3-5a, the ratio of luminous height to the total flame height is denoted as φ_{lum}, the value of which is a function of fuel type and pool diameter. In this study, the value of φ_{lum} is calculated using semi-empirical expressions per Munoz et al. [59], which are summarized in Table 3-3.

Table 3-3: Luminous ratio (φ_{lum}) of the MDSF$_2$ model per [59]

Variable Name	Parameters	Gasoline	Diesel
φ_{lum}	$D_{f,eff} \leq 5$ m	0.45	0.30
	5 m < $D_{f,eff} \leq 20$ m	$aD_{f,eff}^{b} - c$	$aD_{f,eff}^{b} - c$
	$D_{f,eff} > 20$ m	0.05	0.05
Constants	a	1.80	1.26
	b	-0.377	-0.257
	c	0.533	0.533

For pool fires with diameters less than 5 m, $\varphi_{lum} = \varphi_{cyl}$ and the smoke cylinder's downward "extension" is negligible. As the pool diameter increases from 5 m to 20 m, the value of φ_{lum} decreases and the smoke extends downward to obscure more of the flame cylinder [58,62]. For pool fire diameters greater than 20 m, most of the flame shape is covered by smoke and φ_{lum} = 0.05. More experimental testing is needed to develop these luminous height relationships for a wider range of hydrocarbon fuels.

Separate emissive powers are assigned to the flame and smoke portions of the MDSF$_2$ model to represent the realistic distribution of radiative emission from hydrocarbon pool fires. Flame emissive power, E_{flame} (kW/m^2), is calculated as an emitted fraction of peak HRR and is uniformly applied to all discretized surfaces of the flame shape in Figure 3-5b:

$$E_{flame} = \frac{\chi_{r,f} \cdot \dot{Q}_{f,max}}{A_{f,M}} \tag{3-11}$$

where $\dot{Q}_{f,max}$ (kW) is the peak HRR per Eq. (2-4); $A_{f,M}$ (m^2) is the total surface area of the flame shape; and $\chi_{r,f}$ is the radiative fraction of the flames. Semi-empirical expressions for the radiative fraction of the entire fire, χ_r, were previously proposed by others [53,58] based on fit with experimental measurements of radiant heat flux from a wide range of hydrocarbon pool fires. These χ_r expressions, similar to what McGrattan et al. [58] proposed in Eq.

(3-4), are typically a function of pool diameter and are often used for PS or SF calculations that assume a single emissive power value for the entire fire. To calculate $\chi_{r,f}$, the McGrattan et al. expression is generalized to account for the radiative emissions from only the flame portion of the MDSF$_2$ model:

$$\chi_{r,f} = \chi_{r,f_{max}} \cdot e^{-k \cdot D_{f,eff}} \tag{3-12}$$

values of $\chi_{r,f\,max}$ and k were selected as 0.37 and 0.025 m^{-1}, respectively, by Zhu and Quiel [24] for open-air gasoline and diesel pool fires. The values of $\chi_{r,f\,max}$ and k were calibrated using experimental data and FDS results. The proposed $\chi_{r,f}$ expression produces consistently larger values for the flames compared to those predicted for the entire fire in either Eq. (3-3) and (3-4). Note that $\chi_{r,f}$ in this study is only proposed for gasoline and diesel pool fires – application to other fuel types will need further investigation.

As shown in Figure 3-5, the smoke hat will obscure the upper portions of the MDSF$_2$ model's flame shape above $\varphi_{lum} \cdot H_f$ and provide a lower emissive power. Figure 3-6 shows that the emissive power of the visible surfaces of the MDSF$_2$ model is vertically divided into three regions:

1. At $0 < H < \varphi_{lum} \cdot H_f$, the emissive power of the unobscured luminous zone equals E_{flame} per Eqs. (3-11) and (3-12).
2. At $\varphi_{lum} \cdot H_f < H < \varphi_{cyl} \cdot H_f$, the emissive power in the smoke cylinder extension linearly transitions in the upward direction from E_{flame} to a maximum value of E_{smoke}. If $E_{flame} > E_{smoke}$, then E_{smoke} = 40 kW/m^2 per Munoz et al. [62]. If $E_{flame} < E_{smoke}$, then $E_{smoke} = E_{flame}$ as a limiting value and the emissive power in this region is therefore constant.
3. At $\varphi_{cyl} \cdot H_f < H < (1+\varphi_{cyl}) \cdot H_f$, the emissive power in the smoke cone linearly decreases from E_{smoke} to zero as the smoke whirl cools with increasing vertical distance from the flames.

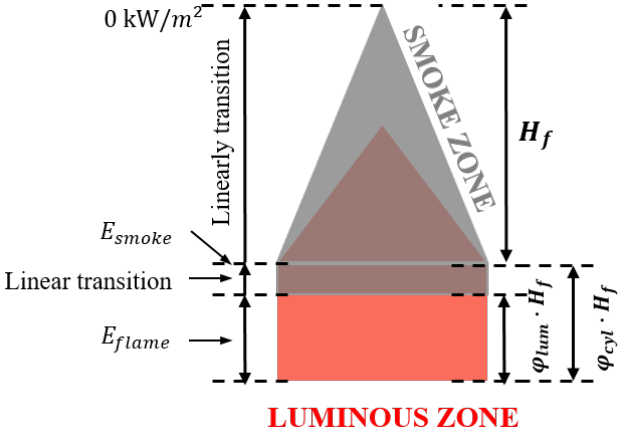

Figure 3-6: Illustration. Emissive power distribution for the MDSF$_2$ model (shown without mesh discretization for clarity) [24].

Like the first generation MDSF model, the total thermal radiation delivered to a target located outside the three-dimensional fire shape is a summation of the contributions from all discretized surfaces that have a view of the target. The radiant heat flux from the MDSF$_2$ model to target surface j is calculated via a slightly revised form of $F_{i\to j}$ in Eq. (3-10b):

$$F_{i\to j} = \frac{A_i \cdot \cos\theta_i \cdot \cos\theta_j}{\pi \cdot r_{i\to j}^{m}} \tag{3-13}$$

The revision pertains to the view factor $F_{i\to j}$, in which the exponent applied to the radial standoff distance is now denoted as variable m. In this study, a value of 2.3 was assigned to m based on calibration against

experimental data and CFD results per Zhu and Quiel [24]. Compared to Eq. (3-10b), the revised view factor in Eq. (3-13) slightly reduces the calculated thermal radiation on targets at most standoffs while increasing it at very small standoffs. Note that assigning a value of 2 for m (thus reverting to Eq. (3-10b)) would provide a conservative prediction for most standoffs (i.e., for $r_{i\to j} > 1$ m).

Based on a preliminary convergence study, the $MDSF_2$ models used in this study are meshed to have 100 elements around their circumference and 200 elements over the full height $[(1+\varphi_{cyl}) \cdot H_f]$ of the flame-plus-smoke shape shown in Figure 3-6. The spacing of the vertical mesh is tailored to accommodate the transitions from the visible flame to the smoke zone and from the cylinder to the cone. For this study, the $MDSF_2$ model was programmed in MATLAB[4] [76] to calculate the summation of heat flux contributions from all discretized surfaces that have a view of the target.

For the case that fire occurs directly beneath a bridge with a low clearance or considering an intense fire with large H_f may cause the bridge overhead to interrupt and partially engulf the $MDSF_2$ geometry. A conservative adaption to the $MDSF_2$ model to this scenario is shown in Figure 3-7. When the smoke cone is interrupted by the bridge deck, its shape is warped into an inverted truncated cone which spans vertically from the lower edge of the smoke layer up to the bridge deck. The new interrupted shape has the same volume as the original cone, thus ensuring conservation of mass via soot production and setting a radius for smoke spread underneath the bridge deck. E_{smoke} is still set to 40 kW/m^2 at the base of the inverted truncated cone. The linear decrease of E_{smoke} in the upward direction has the same function as for the unconfined smoke cone shown previously in Figure 3-6. E_{smoke} at the top of the new truncated shape in Figure 3-7 therefore has the same value as the original unconfined smoke cone at that same height. The emissive power for the flame surfaces is calculated using Eq. (3-11). Since the flame is interrupted as shown in Figure 3-7, the flame surface area (A_f) decreases versus that shown previously in Figure 3-6, thus increasing E_{flame} for the flame shape in Figure 3-7.

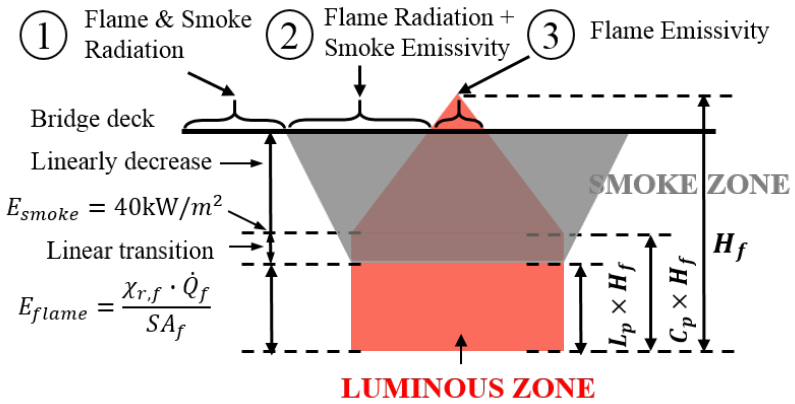

Figure 3-7: Illustration. $MDSF_2$ model (shown without mesh discretization for clarity) with the smoke zone interrupted by a bridge deck overhead [33].

[4] The U.S. Government does not endorse products or manufacturers. They are included for informational purposes only and are not intended to reflect a preference, approval, or endorsement of any one product or entity.

Targets located outside the smoke layer (Region 1 in Figure 3-7) receive heat flux from the smoke and flame surfaces using Eqs. (3-10a), (3-11), (3-12), and (3-13) in the same way as used in the original $MDSF_2$ model, which assumes that the smoke obscures the flame surfaces underneath. Targets that are engulfed by the new smoke shape (Region 2) receive a direct flux (accounting for convective effects) from the smoke as E_{smoke}. Since they are within the turbulent smoke layer, these targets can also see the flame surfaces on the flame cone and receive their associated radiation heat flux.

For targets engulfed by the flame cone (Region 3), $\dot{q}_j^{''}$ is set equal to the lesser of E_{flame} per Eq. (3-11) and an empirical engulfed-in-flame direct heat flux of 170 kW/m^2. The engulfed value conservatively combines direct flame radiation and convective heat transfer into a single heat flux that is based on experimental measurements on objects engulfed in a hydrocarbon fire. If the girders are engulfed by the flame cylinder at a location below the smoke layer, then smoke effects are neglected and all girders within the flame cylinder receive the full engulfed-in-flame heat flux. Note that the flame shapes are not warped in a similar way as the smoke shape – for simplification, they are conservatively assumed to engulf the elements with which they intersect [77]. A more refined model for flame impingement at the underside of the bridge, such as that proposed by Franchini et al. [78], could be utilized as an alternative for greater precision.

3.3 Standard fire curves

Standard fire curves are widely used by the construction industry to quantify the fire resistance of structural and non-structural assemblies and components. These temperature time histories consist of a rapid initial increase followed by a steady period at high temperature with no decay phase. When applied to a structural assembly, the standard fire curve is intended to heat the specimen until a "failure" condition is eventually reached. The equations for the temperature-time curve for ISO 834[5] [79] and ASTM E119[6] [80], which are commonly used for fire resistance evaluations for building assemblies, are provided below:

$$T_{ISO834} = 345 \cdot log_{10}(8t + 1) + T_0 \tag{3-14}$$

$$T_{ASTM\ E119} = 750 \cdot (1 - e^{-3.8 \cdot \sqrt{t_h}}) + 170.41 \cdot \sqrt{t_h} + T_0 \tag{3-15}$$

where T_0 (°C) is the ambient temperature (typically assumed to be 20 °C). For the ISO 834[5] fire curve, t (min) is the time in minutes; for the ASTM E119[6] fire curve, t_h (hr) is the time in hours. Open-air fire hazards for bridges (which are usually fuel controlled and have unlimited oxygen supply) are expected to ramp-up more rapidly than a building compartment fire (which is predominantly ventilation controlled). The ASTM E1529[7] standard hydrocarbon fire curve [81] could apply more relevantly for evaluating the fire resistance of bridge components and assemblies. ASTM E1529[7] stipulates that either of the following equivalent heat exposures be applied to a specimen after 5 min following ignition: steady state heat flux exposure of 158 kW/m^2 ± 8 kW/m^2, or steady state temperature exposure of 1095 °C ± 85 °C. Other

[5] Use of ISO 834, Fire resistance tests, is not a Federal requirement.

[6] Use of ASTM E119, Standard Test Methods for Fire Tests of Building Construction and Materials, is not a Federal requirement.

[7] Use of ASTM E1529, Standard Test Methods for Determining Effects of Large Hydrocarbon Pool Fires on Structural Members and Assemblies, is not a Federal requirement.

applicable standard fire curves may include the hydrocarbon fire or external fire per Eurocode 1[8], Part 1-2 [82] depending on the estimated intensity of the fire event:

$$T_{Hydrocarbon\ fire} = 1080 \cdot (1 - 0.325 \cdot e^{-0.167 \cdot t} - 0.675 \cdot e^{-2.5 \cdot t}) + T_0 \quad (3\text{-}16)$$

$$T_{External\ fire} = 660 \cdot (1 - 0.687 \cdot e^{-0.32 \cdot t} - 0.313 \cdot e^{-3.8 \cdot t}) + T_0 \quad (3\text{-}17)$$

where t (min) is the time in minutes. The standard fire curves introduced above are plotted for comparison in Figure 3-8. These curves are very useful as a comparative platform for developing relative fire resistance ratings of structural and non-structural components and assemblies. However, these curves are prescribed as approximations of the ramp-up and peak thermal demand from an assumed fire type (building enclosure fire, hydrocarbon fire, external fire, etc.), and they therefore have no direct correlation to the HRR magnitudes and durations that were discussed in Section 2. These curves also do not consider spatial orientation or standoff to a given fire hazard and therefore are not compatible with the fire modeling approaches discussed in Section 3.2. The implementation of a standard fire curve as a tool for bridge fire evaluation would need significant assumptions about implementing a burnout or decay phase as well as the spatial contour of application over the length of the bridge element relative to the localized fire hazard. Standard fire curves are therefore not suggested as a representation of a design basis fire. However, hourly ratings based on standard fire testing or analysis can help an analyst compare the relative effectiveness of fire resistance mitigation solutions based on the thermal demand obtained from a design basis fire scenario. This approach is somewhat similar to the complementary use of the Rijkswaterstaat (RWS) standard fire curve in NFPA 502[1] Chapter 7 [1] to develop hourly ratings for assemblies in tunnels while also considering design basis fire scenarios with prescribed HRR (see Table 2-1).

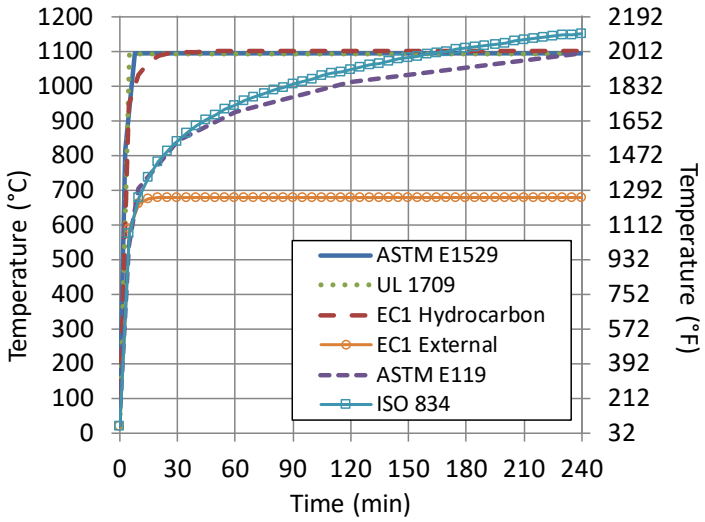

Figure 3-8: Graph. Temperature time histories of select standard fire curves.

[8] Use of Eurocode 1, Part 1-2: Actions on structures is not a Federal requirement.

4 BRIDGE FIRE FREQUENCY

NFPA 502[1] Chapter 6 [1] states that an "engineering analysis" is needed to determine whether the collapse of the bridge due to fire would have an adverse impact on life safety or other unacceptable implications. For a localized open-air fire hazard, the need for an "engineering analysis" and potential bridge fire mitigation depends on the relative influence of the intensity of the fire and its proximity to the bridge, as well as the geometry and construction of the bridge itself.

To identify the critical bridges that warrant analysis against fire hazards, Kodur and Naser [83] previously proposed an approach to calculating an importance factor that accounts for the bridge vulnerability, fire hazard likelihood, traffic demand, and loss consequences. Though straightforward and efficient, the values of the weighted factors used in that framework are somewhat qualitative and do not directly evaluate the likelihood or severity of specific fire hazards for specific bridges. More research is needed to quantify the likelihood of a fire hazard with a given intensity as a function of bridge location and the surrounding infrastructure. For example, previous work by Zhu et al. [44] used a fire model and bridge-to-fire orientation geometry to rank the criticality of vulnerability to a tanker truck fire for all steel girder overpasses in the MacArthur Maze complex interchange in Oakland, CA. The study identified that the overpasses that collapsed due to a 2007 tanker truck fire event were the two most fire-critical spans in the entire interchange.

This section extends the previous work by Zhu et al. [44] to develop a methodology that quantifies the vulnerability of highway bridges to structurally significant fires (i.e. fires that have the potential to cause structural damage) based on their intensity, the structure type of the bridge (i.e., steel girder, concrete bulb-tee girder, concrete box beam, etc.), and traffic presence on and around the bridge. Developing zones of influence for structurally significant fire sizes can help preliminarily judge what warrants a more detailed fire hazard assessment (and potential mitigation actions) for a particular bridge or among an inventory of bridges. Also, using traffic information on nearby roadways or the presence of stationary fuel sources can help quantify the frequency of structurally significant fires within the zone of influence.

4.1 Proposed framework

The proposed framework for quantifying fire frequency utilizes the following three steps:

(1) Develop fire-induced damage isotherms based on thermal analysis of typical structural elements
(2) Delineate zones of influence for vehicle fires of various intensities
(3) Calculate the frequency of structurally significant bridge fires within the zone of influence

In the first step, rather than assessing the damage for various bridge types with complex thermo-structural analyses, thermal analyses are performed for typical structural bridge elements to determine whether a given fire intensity reaches a critical temperature. The critical temperature implicitly indicates a degree of fire-induced damage based on published standards and testing. In the second step, the thermal impact on the bridge element from a vehicle fire hazard is calculated via the Modified Point Source Model (MPS) (presented previously in Section 3.2.2). By combining the structural-fire vulnerability curves with MPS heat exposure results, a "structurally critical" zone of influence can be drawn as a three-dimensional volume around the bridge structure. Essentially, a fire hazard with a given intensity could cause a given degree of damage to the bridge if it were to occur within that three-dimensional shape. The third step involves assessing the likelihood of that fire hazard occurring within its three-dimensional zone of influence. For vehicle-based fire hazards, the likelihood of the fire hazard is estimated by considering traffic data over

roadways that pass through the zone of influence and the rate of traffic accidents that result in fire. For stationary fire hazards, the likelihood of fire occurrence is estimated by quantifying the amount, spatial distribution, and flammability of the potential fuel sources as well as their proximity to an ignition source. In this report, the primary focus considers vehicle-based fire hazards. This proposed methodology is demonstrated with the MacArthur Maze interchange later in this report.

4.2 Fire damage vulnerability (FDV) assessment

This section demonstrates the development of a fire damage vulnerability (FDV) diagram for typical highway overpass bridges (supported by either steel girders or precast/prestressed concrete bulb-tee girders). Bridges with other girder types (such as precast/prestressed concrete tub girders) or supported with other primary elements (such as cables or trusses) could use the general methods outlined in this report to evaluate the FDV. However, analysis of those other structural types (particularly long-span bridges) is more complicated to evaluate and are therefore outside the scope of this baseline illustration.

A fragility curve is a convenient tool for quantifying FDV of a given hazard intensity. Specifically, fragility F_{ls} as a function of a given intensity measure *IM* can evaluate the probability of reaching or exceeding specific damage measures *DM* under a certain level of hazard intensity:

$$F_{ls}(IM) = p[DM|IM] = p[D \geq C_{ls}|IM] \tag{4-1}$$

where D (demand) represents the statistical characteristics of the response of the structural system to the event with intensity *IM*, and C_{ls} describes the capacity of the structure with respect to a pre-defined limit state ls. Fragility curves can be developed for successive levels of damage by considering escalating *DM* thresholds. If successive *DM* states exhibit clear delineations as the *IM* increases, then the fragility-based approach is simplified as a deterministic diagram that maps the expected damage level in response to a given intensity measure.

The thermo-structural response of a bridge to fire hazards depends on its span length, span arrangement (i.e., simply supported versus continuous), structural geometry, structural materials, and applied loading (including gravity and live loads as well as restraint of thermal expansion). Also, the thermo-mechanical failure modes and thresholds (including flexural or shear failure, concrete cracking, loss of prestressing forces, etc.) are not yet fully quantified in the existing experimental literature, especially for prestressed concrete bridge structures [5]. Previous studies such as those by Wright et al. [41] and Quiel and Zhu [33] have considered the thermo-structural impact of a select number of fire scenarios on composite steel girder overpass bridges. These studies used detailed numerical models to quantify fire-induced damage – though effective, the computational cost associated with these thermo-structural analyses may not be conducive to rapid evaluation of bridge-fire vulnerability by practicing engineers. Hence, this study develops FDV diagrams for bridges under fire using thermal analyses of the structural elements, which significantly reduces the numerical complexity of the evaluation approach. Critical temperature limits, which are well-defined for both steel and concrete structural elements in references such as NFPA 502[1] [1] and ASTM E1529[7] [81], can provide an implicit means of quantifying structural damage in terms of temperature increase [44]. Specifically, critical temperatures represent a threshold beyond which a structural element is at increased risk of permanent damage [84].

4.2.1 Typical highway bridge cross-section for thermal analysis

For this study, thermal analysis was performed for the following typical bridge girders: a straight steel I-shape plate girder and a precast/prestressed concrete bulb-tee girder. As an advantage, the temperature threshold provided in the specifications measures the maximum value of the specimen, which is not sensitive to the sizes. For the steel girder, variations in the thickness of the steel plates will not sufficiently change their resistance to fire-induced temperature increase because they are still relatively thin versus their large amount of exposure surface. For the concrete girder, the concrete cover to the outermost layers of reinforcement would remain the same regardless of other dimensions, and this layer is the focus of the temperature change criteria used to quantify damage in this study implicitly. Hence, a generic cross-section (see Figure 4-1) was selected for both a steel and concrete girder based on those used in current practice for a simply supported bridge with a span of 30.5 m (100 ft).

The steel girder dimensions are obtained using eSPAN 140[4] [85], a free web-based tool developed by the Short Span Steel Bridge Alliance for the preliminary design of simple-span and modular steel girder bridge spans up to 42.7 m (140 ft) in compliance with the AASHTO LRFD Bridge Design Specifications, 7th Edition[9] [86]. The I-shaped cross-section has the following dimensions: 1016 mm × 12.7 mm (40 inch × ½ inch) web, 457 mm × 25.4 mm (18 in. × 1 in.) top flange, and 457 mm × 50.8 mm (18 in. × 2 in.) bottom flange. The girder steel is assumed to be ASTM A709[10], Grade 50 [87], with a density of 7850 kg/m^3 (490 pcf). The steel girder is assumed to be composite with a 229-mm (9-inch) thick normal-weight concrete (NWC) deck slab.

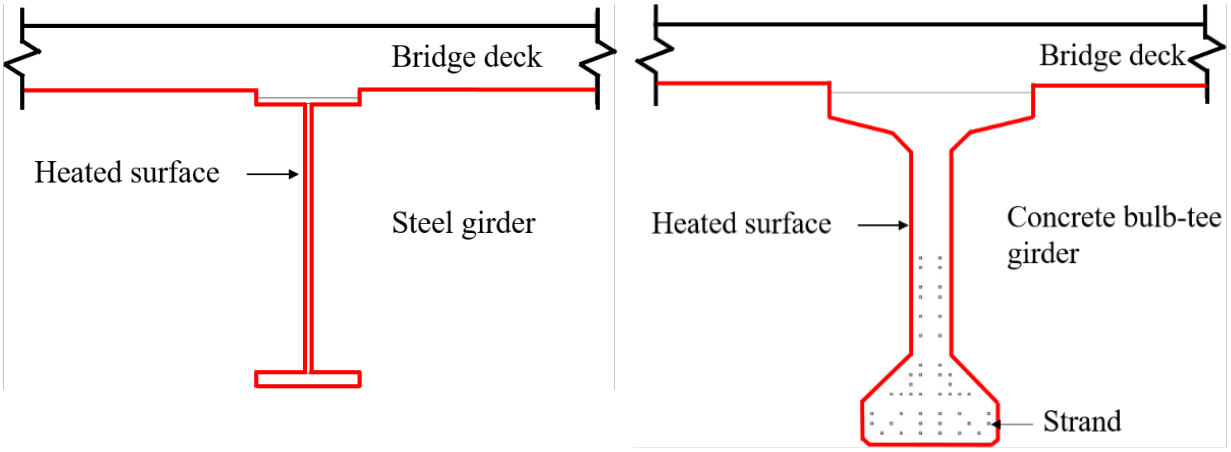

(a) Steel plate girder (b) Precast concrete bulb-tee girder

Figure 4-1: Illustrations. Representative bridge girder sections for thermal analysis.

[9] Use of AASHTO LRFD Bridge Design Specifications, 7th Edition, is no longer a Federal requirement.
[10] Use of ASTM A709, Standard Specification for Structural Steel for Bridges, is not a Federal requirement.

The precast concrete bulb-tee girder cross-section is based on the design example of BT-72 provided by the PCI Bridge Design Manual, 4th Edition[11] [88]. The section has a depth of 1828 mm (72 in.) below the deck (again assumed to be composite NWC with 229 mm [9-in.] thickness) and is prestressed with a total of 46 seven-wire, low-relaxation stands with 12.7-mm (½-in.) diameter. The nominal compressive strength for the NWC in this girder is taken as 44.8 MPa (6.5 ksi). The minimum thickness of the concrete cover to the outermost layer of strands is 50.8 mm (2 inches).

4.2.2 Damage state definitions

The damage to the bridge girder is implicitly assessed using temperature increase as the primary metric. Note that the critical temperature criteria applied in this study demonstrate using the proposed approach. Other alternative metrics could be used in future applications. ASTM E1529[7] [81], "Standard Test Methods for Determining the Effects of Large Hydrocarbon Pool Fires on Structural Members and Assemblies", states that a structural steel member under fire evaluation is regarded to have "failed" once its average temperature exceeds 538 °C (1,000 °F) or its maximum temperature exceeds 649 °C (1,200 °F). ASTM E119[6] [80], "Standard Test Methods for Fire Tests of Building Construction and Materials", cites similar "failure" temperature limits for flexural elements at 593 °C (1,100 °F) for average temperature and 704 °C (1,300 °F) for the maximum temperature. From a material performance standpoint, both Eurocode 3[12], Part 1-2 [89] and Appendix 4 of American Institute of Steel Construction (AISC) 360-22[13] [90] stipulate that the yield strength of mild structural steel will begin to decrease once its temperature exceeds 400 °C (752 °F). Based on these references, this study utilizes the critical temperature limits in Table 4-1 for fire-induced damage, though others could be used depending on the objectives of the assessment.

Critical temperature thresholds regarding fire-induced damage to concrete bridge girders are more limited. For example, NFPA 502[1] Chapter 6 [1] contains little information regarding critical temperatures for fire evaluation of bridges and elevated highways. However, the following information for thermal protection of tunnel structures is provided for road tunnels in NFPA 502[1] Chapter 7 [1]: (1) prevent concrete spalling; (2) prevent the concrete surface temperature from exceeding 380 °C (716 °F); and (3) prevent the temperature of the reinforcement (assuming minimal cover of 25 mm) from reaching 250 °C (482 °F). There is currently no consensus approach for a temperature-based prediction of fire-induced spalling in structural concrete [91]. According to ASTM E119[6] [80] for loaded restrained concrete beams in building construction, the tension steel at any section is not to exceed 427 °C (800 °F) for cold-drawn prestressing steel or exceed 593 °C (1,100 °F) for mild reinforcing steel. Based on these references, this study utilizes the critical temperature limits in Table 4-1 for fire-induced damage for concrete bridge girders.

More research is needed via testing and thermo-structural numerical analysis to further establish appropriate threshold damage levels for concrete girders. Note that these criteria are not applied to the concrete deck in either cross-section. Rather, the focus of this evaluation is on the girders as the primary load-bearing

[11] Use of the PCI Bridge Design Manual, 4th Edition, is not a Federal requirement.

[12] Use of Eurocode 3, Part 1-2: Design of steel structures is not a Federal requirement.

[13] Use of AISC 360, Specification for Structural Steel Buildings, is not a Federal requirement.

element. Similar criteria could apply to different types of bridge structures such as concrete box beams, steel tub girders, steel trusses, or cable-supported bridges.

Table 4-1: Summary of critical temperature limits used for the representative girder cross-sections.

Representative Cross-Section Type	Damage Severity	Critical Temperature Description	Source Reference
Steel Plate I-Girder with Composite Deck	Structurally critical damage	Maximum temperature exceeds 649 °C (1,200 °F) at any location of the steel girder cross-section	ASTM E119[6] [80]
Steel Plate I-Girder with Composite Deck	Potential structural damage	Maximum temperature exceeds 400 °C (752 °F) at any location of the steel girder cross-section	AISC 360-22[13] Appendix 4 [90]
Prestressed Concrete Bulb-Tee Girder with Composite Deck	Structurally critical damage	Maximum temperature exceeds 427 °C (800 °F) at any prestressing strand or 593 °C (1,100 °F) at any mild steel reinforcement	ASTM E119[6] [80]
Prestressed Concrete Bulb-Tee Girder with Composite Deck	Potential structural damage	Maximum temperature exceeds 380 °C (716 °F) at any concrete surface or 250 °C (482 °F) at any steel reinforcement	NFPA 502[1] Chapter 7 [1]

4.2.3 Damage classification development

Note again that the cross-sections in Figure 4-1 are used here as representative examples to demonstrate how to develop the thermal analysis and FDV diagram. The depth and dimensions of both the steel plate girder and concrete bulb-tee girder will vary based on loading, span, boundary conditions, and support conditions. However, the degree of heat transfer into these cross-sections due to fire exposure will be very similar regardless of these variations over the same time duration. For the steel girder, variations in the thickness of the steel plates will not sufficiently change their resistance to fire-induced temperature increase because they would still be relatively thin versus their large amount of exposure surface. For the concrete girder, the concrete cover to the outermost layers of reinforcement would remain the same regardless of other dimensions, and this layer is the focus of the temperature change criteria used to quantify damage in this study implicitly. In future research, implementing structural analysis with the results of the thermal analysis as input would indeed need to consider changes in girder cross-section, loading, span, and boundary conditions. For this study, the simplified approach of using temperature increase as an implicit measure of damage enables the use of representative sections to adequately represent the response of a much wider inventory of bridges that use these types of girders.

A two-dimensional thermal analysis of the representative girder cross-sections was performed using the finite element (FE) software SAFIR[4] [92] to calculate temperature increase due to fire exposure. The cross-section is discretized into two-dimensional-solid elements (or fibers), and thermal exposure "frontiers" are applied to the fire-exposed surfaces. The web and flanges of the steel plate girder prototype were discretized to have ten fibers over their width and one fiber through their thickness. This relatively coarse discretization pattern is possible due to the relatively high thermal conductivity of the steel material [93]. Discretization of the concrete cross-section was performed with GiD[4] [94], an interactive graphical user interface used to mesh geometric shapes for numerical simulation. The mesh of the concrete cross-section used quadrilateral elements with maximum edge dimensions of 5 mm (0.2 inch), which is adequate for developing thermal

gradients due to lower thermal conductivity [95]. The slabs for both the steel and concrete cross-sections also used quadrilateral elements with maximum edge dimensions of 5 mm (0.2 inch).

Temperature-dependent thermal properties of the steel girder (including the thermal conductivity and specific heat) are modeled in accordance with Eurocode 3[12], Part 1-2 [89], while those for NWC (assumed with calcareous aggregate) and steel reinforcement are modeled in accordance with Eurocode 2[14], Part 1-2 [96]. Convective coefficients for the fire-exposed and unexposed surfaces are 25 kW/m^2 and 9 kW/m^2 per Eurocode 1[8], Part 1-2 [82]. The emissivity of fire-exposed steel and concrete surfaces is taken as 0.7 per the Eurocode, and the emissivity of hot gases from fire exposure is taken as 0.67 per Buchanan [31].

As a conservative approximation, the entire perimeter of each cross-section is assumed simultaneously exposed to the thermal impact (as shown with the exposure frontier in Figure 4-1 on the underside of the deck), which represents full engulfment by the fire plume. Note that realistic fires might only "see" a portion of the girder cross-section; however, the change in heated perimeter will have an insignificant impact on the maximum temperature developed in the heated cross-section (which is used as the benchmark for this assessment). The fire intensity is quantified as incident heat flux onto the heated surface over an exposure duration. To generate the map for damage classification, a Monte Carlo Simulation (MCS) was performed with the thermal FE models, in which the magnitude of the heat flux $\dot{q}''$ was randomly chosen from 1 to 300 kW/m^2, while the exposure duration was randomly selected from 1 to 90 min. A stochastic analysis with a sample size of 1,000, developed using the Latin Hypercube Sampling (LHS) [97], is adequate to develop a well-populated field of cases for damage classification [33].

The results of the thermal analysis are sorted into their respective damage levels according to the aforementioned temperature criteria limits for each girder type. These points are then marked according to each damage level and plotted on axes of heat flux versus exposure time, as shown in Figure 4-2a and Figure 4-3a. These plots show clear but nonlinear boundaries between the damage states, the equations for which would be difficult to determine. By replotting the data in ln-ln scale in Figure 4-2b and Figure 4-3b, the boundaries between damage states become linearized and can be detected using the Support Vector Machine (SVM) algorithm, a supervised machine learning approach [98]. This algorithm draws a hyperplane that minimizes overlap between two regions of data points. A linear kernel is utilized as the basis for SVM analysis in the ln-ln plots of Figure 4-2b and Figure 4-3b:

$$w_1 \cdot \ln(\dot{q}) + w_2 \cdot \ln(t) + b = 0 \tag{4-2}$$

where w_1 and w_2 are weighting factors, and b is the bias term. The resulting linear boundaries between each damage level are plotted with dashed lines in Figure 4-2b and Figure 4-3b, and the value of the coefficients associated with each boundary are summarized in Table 4-2. These boundaries ensure that at least 98% of all data points corresponding to a given damage level will fall into the correct region on these plots. These boundaries per Eq. (4-2) are then replotted, as shown in Figure 4-2a and Figure 4-3a, as a nonlinear function. These isotherms represent deterministic FDV curves, which represent fragility limits,

[14] Use of Eurocode 2, Part 1-2: Design of concrete structures is not a Federal requirement.

for each damage state and provide a high degree of accuracy for separating damage states as a function of fire intensity.

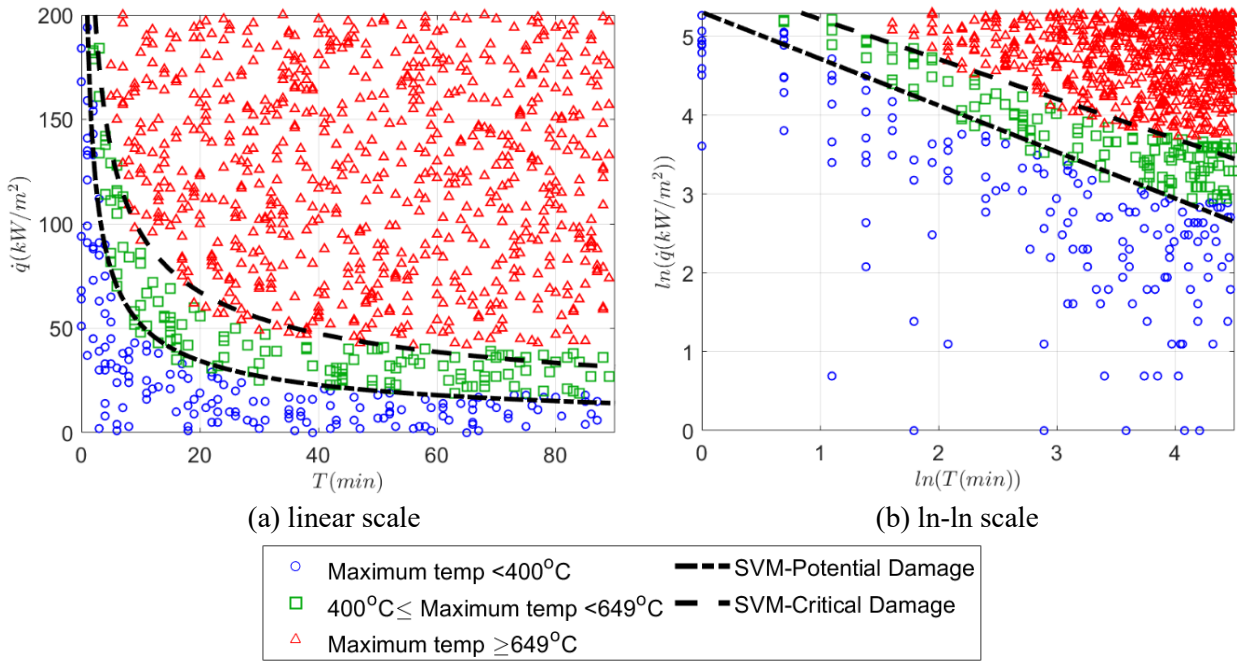

(a) linear scale (b) ln-ln scale

Figure 4-2: Graphs. Damage classification of the representative steel girder based on thermal analysis, including boundaries between damage levels per Support Vector Machine (SVM) analysis.

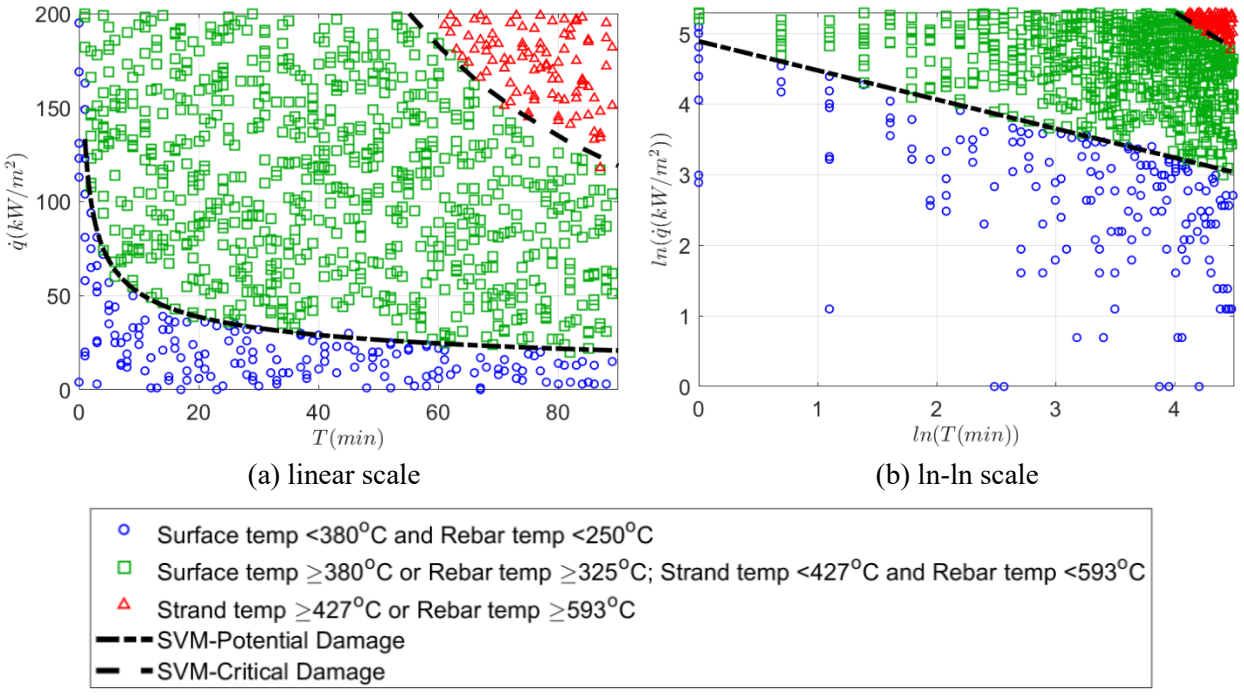

(a) linear scale (b) ln-ln scale

Figure 4-3: Graphs. Damage classification of the representative concrete girder based on thermal analysis, including boundaries between damage levels per Support Vector Machine (SVM) analysis.

Table 4-2: Linear SVM coefficients for damage state boundaries in ln-ln space.

Bridge type	Boundary	w_1	w_2	b	Slope $(-w_1/w_2)$
Steel girder	Potential damage	2.46	4.16	-22.09	-0.591
	Critical damage	2.70	5.34	-30.58	-0.506
Concrete girder	Potential damage	2.01	4.86	-23.80	-0.413
	Critical damage	5.34	5.06	-48.25	-1.055

Note that the thermal analysis performed for the concrete bulb-tee girder cross-section does not account for loss of concrete cover due to thermally induced spalling, which can accelerate the temperature increase of the embedded reinforcement. Experimental testing by Carlton et al. [99] on normal weight concrete panels under one-sided high intensity thermal exposure indicated that fire-induced spalling is likely to occur once the concrete surface temperature reaches approximately 450 °C. The potential damage temperature thresholds for the concrete girder would therefore not be influenced by spalling and are therefore utilized in later sections of this paper for comparison with the potential damage thresholds of the steel girder. The critical damage thresholds for reinforcement temperature in the concrete girder, however, are likely to be reached after the concrete surface temperature has exceeded 450 °C, and it is therefore likely that the concrete may spall before those thresholds are reached. The critical damage metrics for the concrete girder shown in Figure 4-3 and Table 4-2 are therefore not suggested for general application unless spalling is prevented and the concrete cover is preserved throughout fire exposure. More research is needed to incorporate the potential onset of spalling and develop reduced thresholds for "critical" structural damage of these concrete elements.

4.3 Influence zones for structurally significant fires

The exposure from a given fire hazard can correspond to a thermally induced damage state for the representative girders by calculating the magnitude and duration of heat flux exposure to the girder and then plotting that point within the damage maps in Figure 4-2a and Figure 4-3a. For this study, the computationally efficient MPS model is implemented to obtain the heat flux intensity on a given target based on a fire's size (quantified in terms of heat release rate or HRR, in MW) as well as its standoff distance and orientation (i.e., angle of exposure) to that target. The standoff radius (or zone of influence) at which a given fire intensity is located to cause a particular level of damage to a bridge girder is developed by coupling the damage classification maps in Figure 4-2a and Figure 4-3a with the calculated heat flux and duration from the MPS model of that fire at a range of locations. These influence zones, corresponding to "potential" or "critical" structural damage, can form a three-dimensional shape around the bridge within which any fire with the corresponding fire size would cause that specified level of damage.

It should be noted that the MDSF model per Section 3.2.4 could have been used in this assessment as an alternative to the MPS model but at significantly more computational effort. The MDSF model is more conducive when examining a smaller set of fire scenarios in greater detail, since it provides a more precise contour of heat flux exposure to the bridge elements as a three-dimensional fire object [24]. The MPS model per Section 3.2.2, however, can provide conservative predictions of peak fire exposure with very minimal computational effort [24]. This assessment focuses on the peak heat flux experienced by the bridge element for a large suite of fire locations and sizes; therefore, the MPS model is therefore appropriate.

4.3.1 Thermal impact quantification via the MPS model

To apply the MPS model to bridge fire scenarios, the user accounts for the relative orientation of the fire to targets that it can "see" and the heat. For example, a vehicle fire located on the bridge deck will heat the top of the deck, but the girders are shielded from direct fire exposure and are therefore considered to be minimally heated by the fire. The fire needs a direct line of sight to the structural targets to apply heat flux to their exposed surfaces. For the evaluation in this study, the fire is located underneath or alongside the bridge so that the girders are always directly heated for each scenario. Generally, the following scenarios are listed to further clarify the MPS model application.

a) **Vehicle fire above the bridge deck**: point source emitter location following the description in this section, but the radiation to the bridge girder is blocked by the bridge deck.
b) **Vehicle fire alongside the bridge:** point source emitter location and radiative heat flux calculation following the description in this section.
c) **Vehicle fire and the MPS point emitter underneath the bridge deck:** the same as (b).

For many long-span bridges, which is beyond the scope of this study, fires on the deck of the bridge will have a direct view of primary structures such as trussing or cables, and the same methods proposed for this study could apply to those elements. For example, a previous study by Mueller et al. [100] examined the effects of a fire (modeled using the aforementioned PS model) on the deck of a cable-stayed bridge.

The maximum heat flux that the bridge girder can receive is capped at 170 kW/m^2, which was demonstrated by experimental measurements as a practical upper bound for objects engulfed in a hydrocarbon fire [53]. The girders underneath the bridge deck are represented as line elements that run through their geometric centroid for thermal impact calculation, and each girder is discretized into 0.6-m (2-ft) segments along its length. The distributions of the peak heat flux on the bridge girders subjected to a 100 MW fire underneath and alongside the bridge is illustrated in Figure 4-4a and b, respectively. The enlarged dot on each figure represents the location of the emitter for the MPS model.

The total combustion energy E_{tot} (GJ) of the fire is calculated as a function of peak HRR and is based on the experimental data for vehicle combustion. This study adopts the upper bound value via Eq. (2-2a) in Section 2.1.1. The full HRR time history of the fire adopts the quadratic curve from Section 2.2.4.

4.3.2 Locations of structurally significant fires

The trial locations of the fire hazard of given intensity are systematically arranged in a three-dimensional grid over a quarter area underneath and alongside the prototype bridge, which is assumed with a 36-m (120-ft) span, as presented in Figure 4-5. Note that the span is merely representative, and the results of this evaluation could be applied to a straight girder overpass bridge of any span since the results of the thermal analysis are for the cross-sectional location with maximum exposure. The first point of the three-dimensional grid is at the plan center of the bridge, at a clearance of 1.52 m (5 ft) from the bottom of the bridge girder. Increments of 1.52 m (5 ft) are then applied in the plane's length and width directions (pictured in Figure 4-5) and downward as additional layers with increased clearance. Note that the locations shown in Figure 4-5 do not account for potential obstruction by the abutments, bracing, etc. to the fire's view of the girders. When applying these methods, the analyst should account for realistic obstructions of heat transmission from the fire to the target girders.

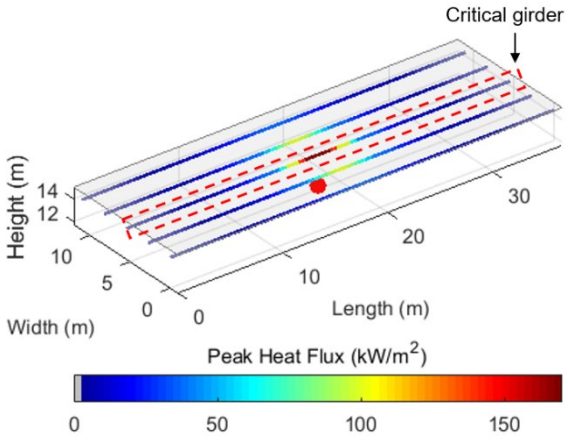

(a) Fire located directly underneath the bridge

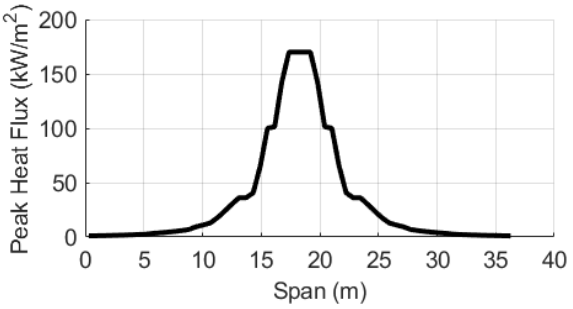

(b) Heat flux of critical girder in (a)

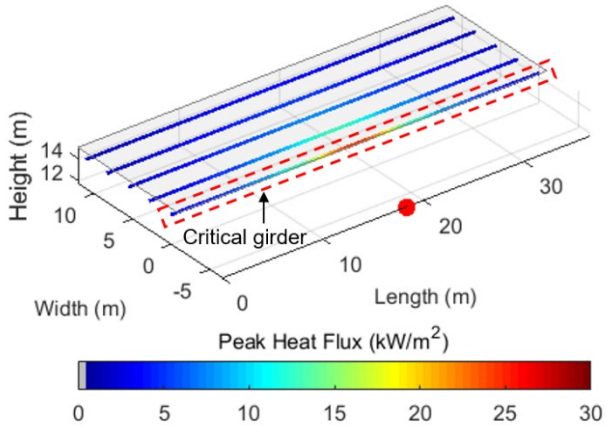

(c) Fire located alongside and underneath the bridge

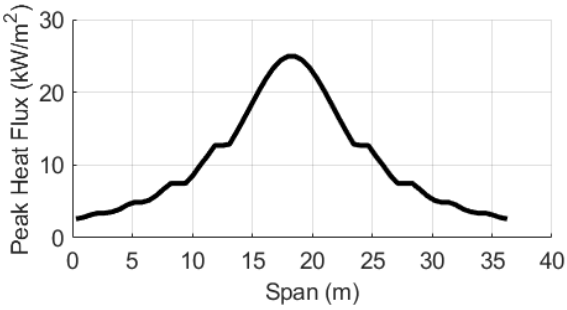

(d) Heat flux of critical girder in (c)

Figure 4-4: Illustrations. Heat flux distribution from the MPS model for a 100 MW fire source.

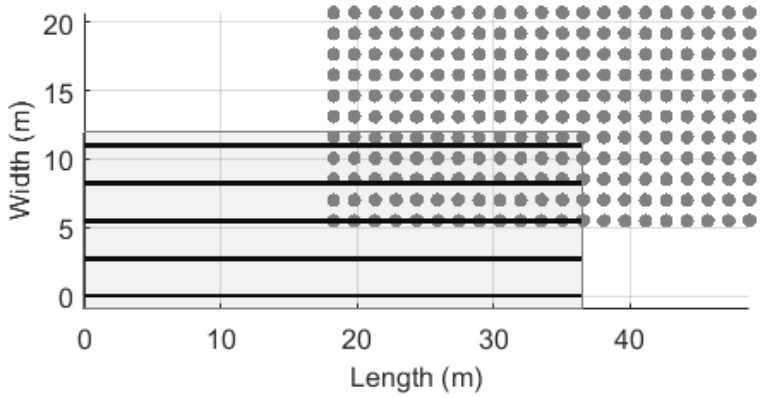

Figure 4-5: Graph. Plan of trial locations for a vehicle fire relative to the bridge footprint (with each location evaluated at varying clearance underneath the bridge).

At each fire location, the MPS model is then used to obtain the heat flux distribution at all discretized targets on each girder. As shown in Figure 4-6, the bridge segment receiving the highest peak heat flux ($\dot{q}''_j$) is then selected for bridge thermal damage assessment. The exposure time (t_j) is calculated using energy equivalency (i.e., the area under the heat flux time history curve) between the quadratic exposure curve per Ingason [16] and the simplified "pulse" duration approach (with no ramp-up or ramp-down), as illustrated in Figure 4-6. The peak heat flux and exposure time are then used to enter the damage classification maps for the girder type of interest to determine the corresponding damage state. As illustrated in Figure 4-6, a 150 MW fire with 4.56-m (15-ft) clearance underneath the plan center of the bridge span with the representative steel girder will cause a structural "critical" damage state in the worst-case girder.

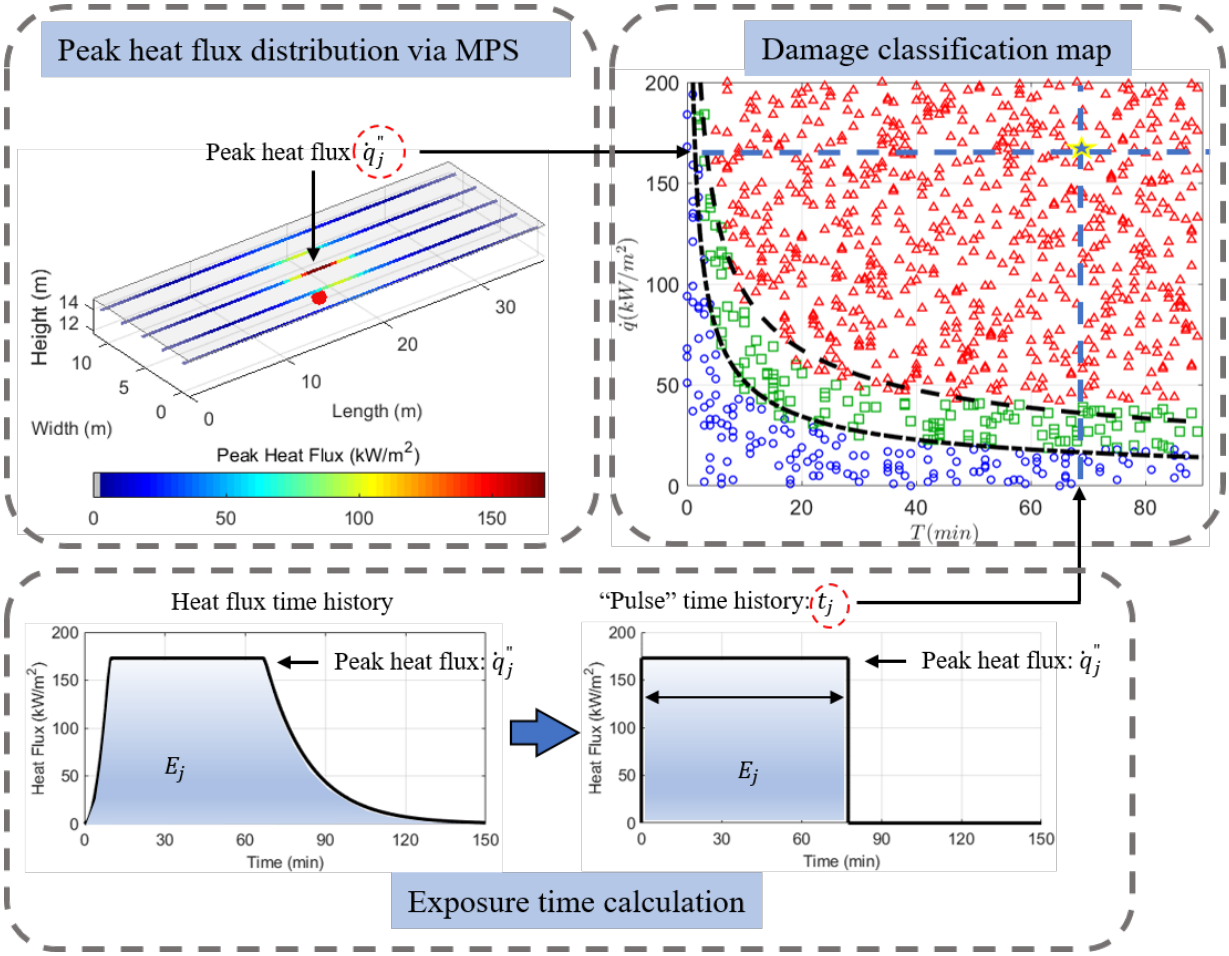

Figure 4-6: Illustration. Fire damage assessment procedure for a steel girder bridge.

This damage assessment process can be repeated at all trial fire locations, and the furthest points that cause a particular damage state for a given fire hazard and girder type can be used to develop a corresponding three-dimensional influence zone. Illustrated in Figure 4-7a, the locations of the fire hazard of 150 MW that cause structurally "critical" damage to any point on any steel girder in the prototype bridge are circled and are wrapped with a three-dimensional convex hull shape. Inside this hull, a fire hazard over 150 MW would raise the maximum temperature of the girder to 649 °C. To simplify the derivation of the three-dimensional

shape, the convex hull can be replaced by a rectangular prism, as shown in Figure 4-7b, whose plan dimensions and vertical clearance are the same as the hull. The dimensions of the prism can be described with three key geometric parameters:

- X standoff is measured as the furthest distance from the longitudinal ends of the bridge at which a fire hazard of a particular magnitude would cause the damage state of interest to any girder at the minimum 1.52-m (5-ft) clearance.
- Y standoff is measured as the furthest transverse distance from the edge of the bridge deck at which a fire hazard of a particular magnitude would cause the damage state of interest to any girder at the minimum 1.52-m (5-ft) clearance.
- Clearance is measured as the maximum vertical distance from the bottom of the bridge girder at which a fire hazard of a particular magnitude would cause the damage state of interest to any girder.

The influence zones for "potential" and "critical" damage to the representative steel girder bridge when subjected to a 150 MW fire are illustrated in Figure 4-7b, with corresponding parameters listed in Table 4-3 and Table 4-4, respectively. Note that the "potential" damage region indicates that the bridge girders would experience at least this level of damage for a 150 MW fire that was located inside the corresponding rectangular prism. Within the smaller subregion, the damage due to the 150 MW fire would be upgraded to structurally "critical." Similar influence zone parameters for "potential" damage to the representative concrete bulb-tee girder bridge are provided in Table 4-5.

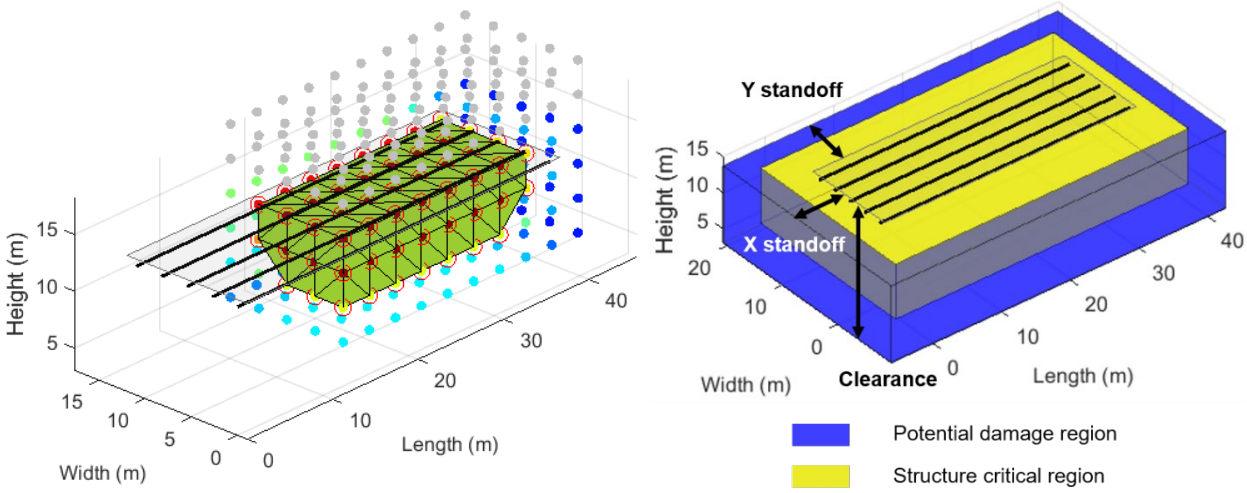

(a) Convex hull (cut-away for two-thirds of the span only) (b) Rectangular prism (shown for the full span)

Figure 4-7: Illustrations. Derivation of fire-induced damage influence zones for the representative steel girder bridge subjected to a 150 MW vehicle fire hazard.

Table 4-3: Dimensions of rectangular prismatic influence zones corresponding to "critical" structural damage for the representative steel girder bridge.

HRR (MW)	X standoff (m)	Y standoff (m)	Clearance (m)
10	0.00	0.38	3.05
20	1.52	1.14	3.05
30	1.52	2.67	4.57
40	1.52	2.67	6.10
50	1.52	2.67	6.10
60	1.52	2.67	6.10
70	3.05	4.19	6.10
80	3.05	4.19	7.62
90	3.05	4.19	7.62
100	3.05	4.19	7.62
110	3.05	4.19	7.62
120	3.05	5.72	7.62
130	3.05	5.72	7.62
140	3.05	5.72	7.62
150	3.05	5.72	7.62
160	3.05	5.72	9.14
170	3.05	5.72	9.14
180	4.57	5.72	9.14
190	4.57	5.72	9.14
200	4.57	5.72	9.14
210	4.57	5.72	9.14
220	4.57	7.24	9.14
230	4.57	7.24	9.14
240	4.57	7.24	9.14
250	4.57	7.24	9.14
260	4.57	7.24	9.14
270	4.57	7.24	9.14
280	4.57	7.24	9.14
290	4.57	7.24	9.14
300	4.57	7.24	9.14

Table 4-4: Dimensions of rectangular prismatic influence zones corresponding to "potential" structural damage for the representative steel girder bridge.

HRR (MW)	X standoff (m)	Y standoff (m)	Clearance (m)
10	1.52	1.14	3.05
20	1.52	2.67	4.57
30	3.05	4.19	6.10
40	3.05	4.19	7.62
50	3.05	5.72	7.62
60	3.05	5.72	9.14
70	4.57	5.72	9.14
80	4.57	5.72	9.14
90	4.57	7.24	9.14
100	4.57	7.24	10.67
110	4.57	7.24	10.67
120	4.57	7.24	10.67
130	4.57	8.76	10.67
140	6.10	8.76	10.67
150	6.10	8.76	10.67
160	6.10	8.76	12.19
170	6.10	8.76	12.19
180	6.10	8.76	12.19
190	6.10	8.76	12.19
200	6.10	8.76	12.19
210	6.10	8.76	12.19
220	6.10	8.76	12.19
230	6.10	8.76	12.19
240	6.10	8.76	13.72
250	7.62	8.76	13.72
260	7.62	8.76	13.72
270	7.62	8.76	13.72
280	7.62	8.76	13.72
290	7.62	8.76	13.72
300	7.62	8.76	13.72

Table 4-5: Dimensions of rectangular prismatic influence zones corresponding to "potential" structural damage for the representative concrete girder bridge.

HRR (MW)	X standoff (m)	Y standoff (m)	Clearance (m)
10	0.00	1.14	4.34
20	1.52	2.67	5.87
30	1.52	2.67	7.39
40	1.52	4.19	7.39
50	3.05	4.19	8.92
60	3.05	4.19	8.92
70	3.05	4.19	8.92
80	3.05	5.72	8.92
90	3.05	5.72	10.44
100	3.05	5.72	10.44
110	4.57	5.72	10.44
120	4.57	5.72	10.44
130	4.57	7.24	10.44
140	4.57	7.24	10.44
150	4.57	7.24	10.44
160	4.57	7.24	11.96
170	4.57	7.24	11.96
180	4.57	7.24	11.96
190	4.57	7.24	11.96
200	4.57	8.76	11.96
210	4.57	8.76	11.96
220	6.10	8.76	11.96
230	6.10	8.76	11.96
240	6.10	8.76	11.96
250	6.10	8.76	11.96
260	6.10	8.76	11.96
270	6.10	8.76	11.96
280	6.10	8.76	13.49
290	6.10	8.76	13.49
300	6.10	8.76	13.49

4.4 Fire frequency and lower bound design-basis fire intensity

The influence zones for fires with varying intensities can be used to determine the lower bound fire intensity that should be considered in the design process for a target bridge span and to calculate the fire frequency corresponding to the given damage state (i.e., "potential" or "critical"). As illustrated in Figure 4-8, the influence zones are applied to an overpass bridge span, with thick lines representing the girders underneath the bridge deck. The lowest fire intensity influence zone that touches any roadway passing underneath would represent the lower bound fire intensity that should be considered design or evaluation or the target overpass. For example, gradually increasing the fire intensities will enlarge the influence zone (i.e., from

the innermost rectangular prism for HRR_a to the middle rectangular prism for HRR_b in Figure 4-8), thus capturing a large potential area through which associated vehicles could pass.

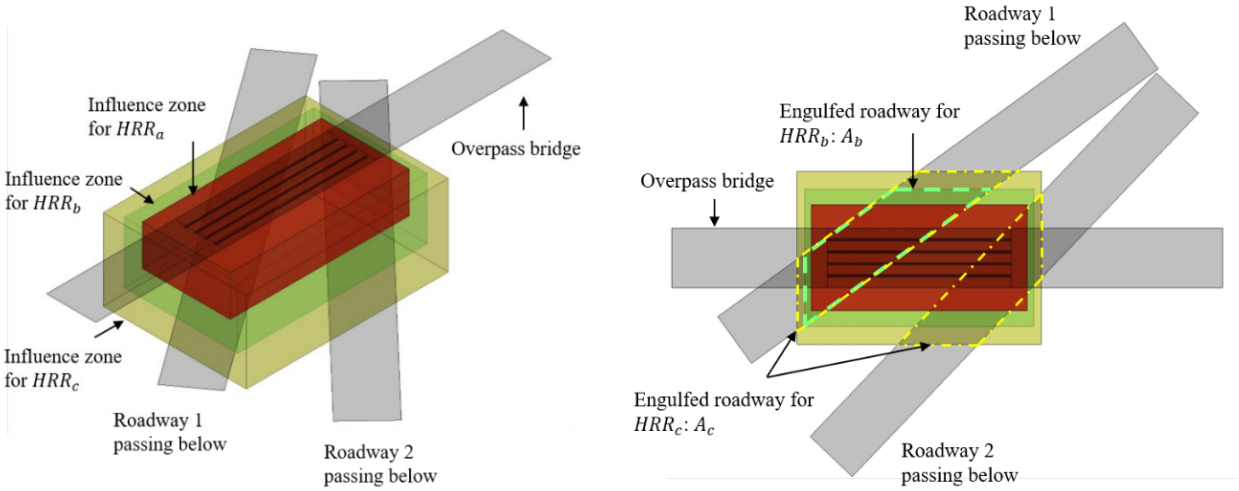

(a) Detect lower bound fire intensity prism intersections (b) Outline distances for fire frequency

Figure 4-8: Illustrations. Influence zone application to calculate fire frequency for an overpass crossing two roadways below.

The frequency of having a structurally significant vehicle fire (i.e., causing either "potential" or "critical" structural, damage) within the corresponding influence zones can be quantified by accounting for the length and associated traffic volume of the roadway that passes through the rectangular prism for a specific fire intensity. Referring to the plan view of the interchange in Figure 4-8b, the region framed with dashed lines on Roadway 1 indicates the length of roadway where a vehicle fire at intensity HRR_b would damage the target overpass. Enlarging the influence zone to the outer rectangular prism for higher intensity HRR_c would then intersect a larger dash-dot enclosed region on Roadway 1 as well as on Roadway 2 where a vehicle fire at that intensity would damage the target overpass. Using these dashed intersected regions, the number of structurally significant fires at fire intensity HRR_i within a year, $f_{ss,i}$, can be calculated:

$$f_{ss,i} = \Sigma(AADT \cdot L_{(A_i - A_{i-1})} \cdot TFR \cdot P(HRR \geq HRR_i) \cdot 365) \tag{4-3}$$

where A_i represents the area of the intersected regions of the roadway underneath the target bridge for fire intensity HRR_i ; $AADT$ (vehicles/day) is the annual average daily traffic; $L_{(A_i - A_{i-1})}$ (miles) is the incremental length of the region from A_{i-1} to A_i between successive fire intensities; TFR is the traffic fire rate (fires per million vehicle-miles); and $P(HRR \geq HRR_i)$ is the probability that the fire intensity will exceed HRR_i, which can be calculated via the cumulative density function $CDF(HRR_i)$:

$$P(HRR \geq HRR_i) = 1 - CDF(HRR_i) \tag{4-4}$$

The annual number of structurally significant fires, f_{ss}, can then be calculated as the summation of contributions from the fire of various intensities:

$$f_{ss} = \Sigma_{i=1}^{n} f_{ss,i} \tag{4-5}$$

A detailed demonstration of this calculation is provided in the Section 5 via case study.

5 DESIGN FIRE LOAD QUANTIFICATION

5.1 Case study: MacArthur Maze highway interchange

The MacArthur Maze complex highway interchange (as shown in the aerial snapshot in Figure 5-1a) is used as a case study to demonstrate the application of the influence zones, the calculation process of the fire frequency corresponding to a given damage level, and the calculation of a design fire load. Figure 5-1b illustrates the model extraction of the interchange (with all bridge spans marked as shaded panels). Note that all relative vertical locations of the roadways are included in this model, as detailed in the previous study by Zhu et al. [44]. The overpass spans on roadway R1 that collapsed in 2007 were supported by steel girders very similar to the representative cross-section shown earlier in Section 4.2.1. The collapse was caused by a severe fire (with an estimated HRR of 300 MW [38], shown on the cover photo of this report) from a tanker truck crash on roadway R6, just below the R1 overpasses as shown in Figure 5-1.

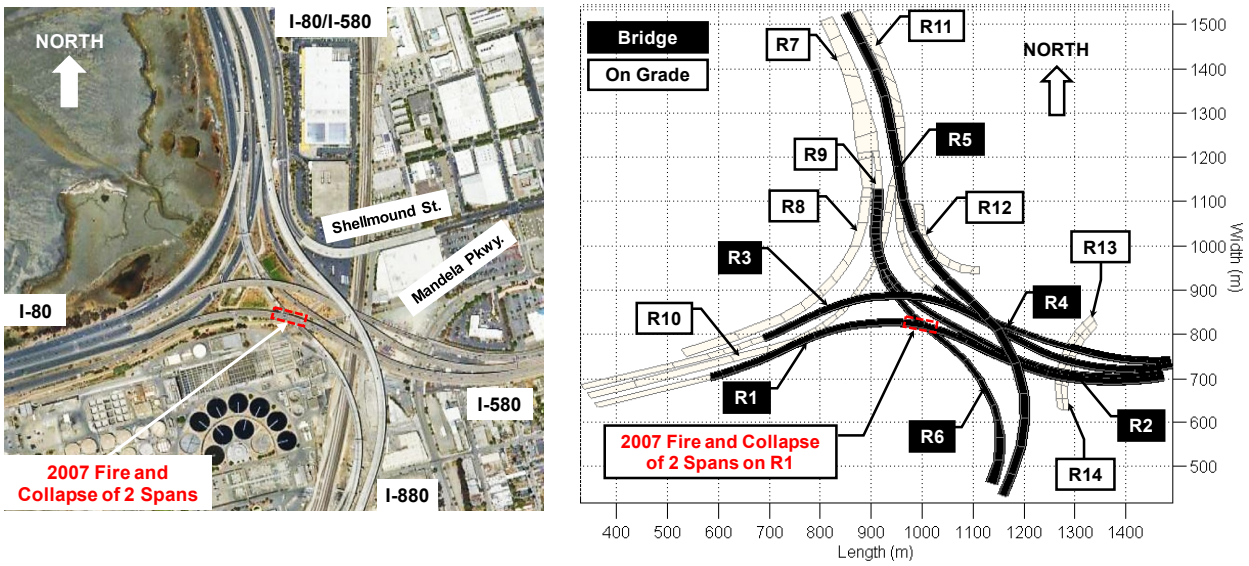

(a) Aerial image (background from [101]) (b) Model extraction

Figure 5-1: Illustrations. Snapshots of the MacArthur Maze complex interchange, with each roadway labelled for the purposes of this study.

5.2 Structurally significant fire intensity

Figure 5-2a highlights a portion of the interchange, with prismatic influence zones corresponding to "critical" structural damage for fire hazard sizes ranging from 10 to 300 MW (nested from smallest to largest) placed underneath the two R1 spans that collapsed during the 2007 fire event. The rectangular prism for the 80 MW fire is the smallest shape that intersects the R6 roadway underneath the R1 overpasses. Therefore, the conclusion could be made that fire hazards over 80 MW on the R6 roadway within this prismatic influence zone could severely damage the target bridge spans. Larger fires (for example, at 250 MW with the prismatic influence zone shown in red) can induce "critical" structural damage at a further standoff distance, as shown in Figure 5-2b. This figure indicates the minimum fire intensity that could lead to "critical" structural damage with respect to its location on the R6.

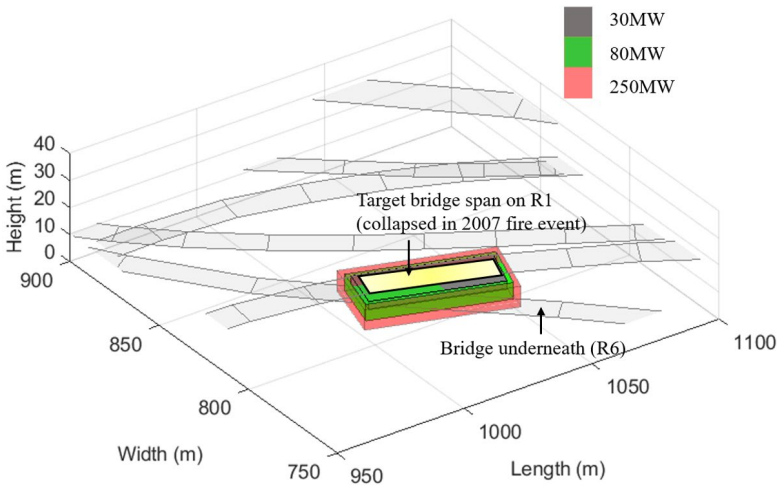

(a) "Critical" structural damage prisms per Table 4-3 for the R1 steel girder overpasses

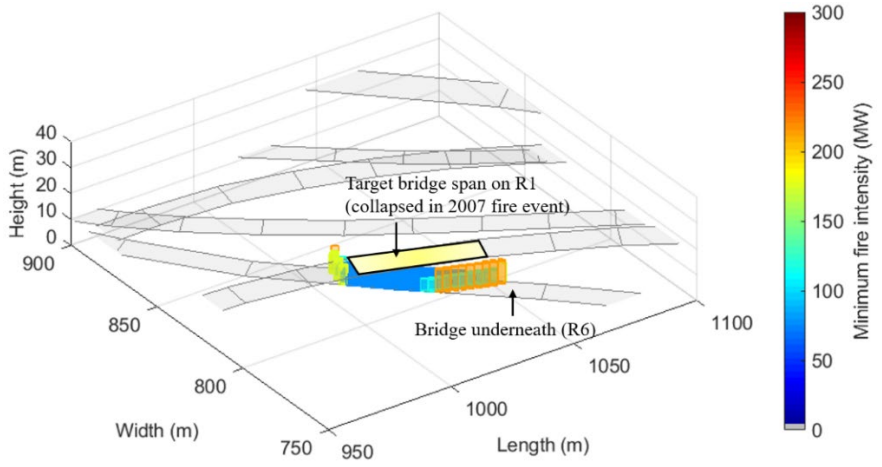

(b) Minimum fire intensity locations that would cause "critical" structural damage

Figure 5-2: Illustrations. Application of the "critical" structural influence zones for the MacArthur Maze R1 spans that collapsed during the 2007 fire event.

By applying the same approach for all the bridge spans in the MacArthur Maze highway interchange, the distribution of the minimum fire intensities that could cause "critical" structural damage is presented in Figure 5-3a. The results show that only a 40 MW fire is needed to cause structural "critical" damage for some overpass spans (i.e., the spans of R9 crossing over R10 and spans of R3 crossing over R2 and R6) due to their lower clearance. Other overpass spans are affected by roadways that are close by but do not cross directly underneath. For example, some overpasses on R5 will be damaged by fire intensities ranging from 100 to 170 MW that occur on R11, which runs below and alongside. Alternatively, the fire intensities in Figure 5-3a can be correlated to the vehicle fire intensities in NFPA 502[1] Chapter 6 [1] to provide a more intuitive map of fire-induced damage for each overpass span according to vehicle type. For example, the 10–20 MW fire size typically represents a fire for multiple passenger cars, while HGV fires range from 40 MW to 200 MW. The resulting map of the MacArthur Maze is shown in Figure 5-3b. This contour figure indicates that an HGV fire is needed to threaten the structural safety (structurally "critical" damage) of the spans collapsed 2007 fire hazard.

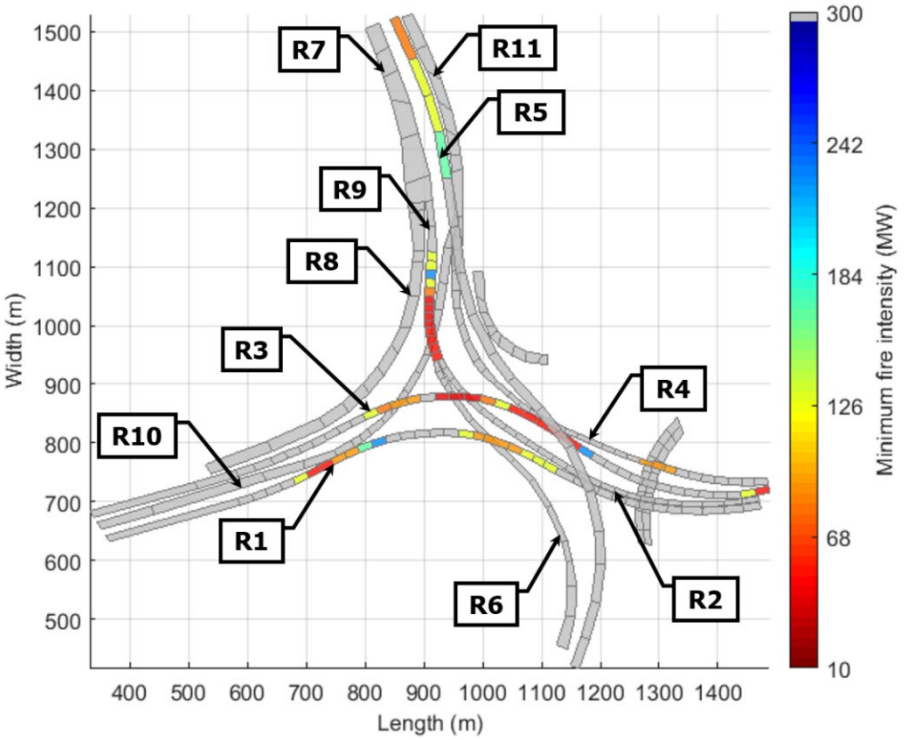

(a) By fire intensity (MW)

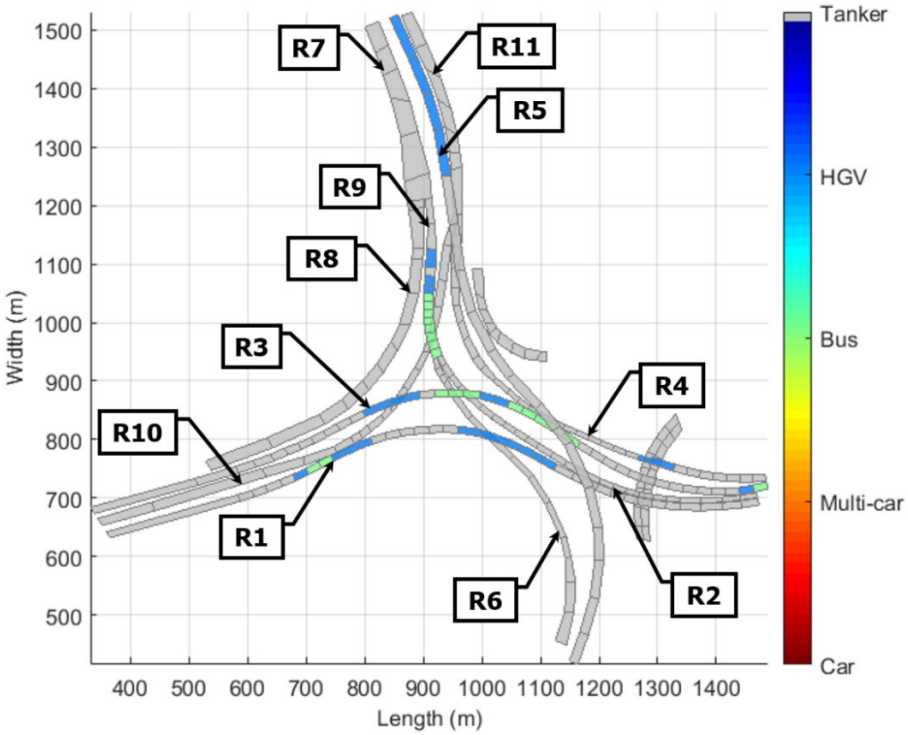

(b) By vehicle type (per NFPA 502[1])

Figure 5-3: Illustrations. Map of minimum fire intensity that would cause "critical" structural damage to the MacArthur Maze highway interchange (all overpass bridges use steel plate girders).

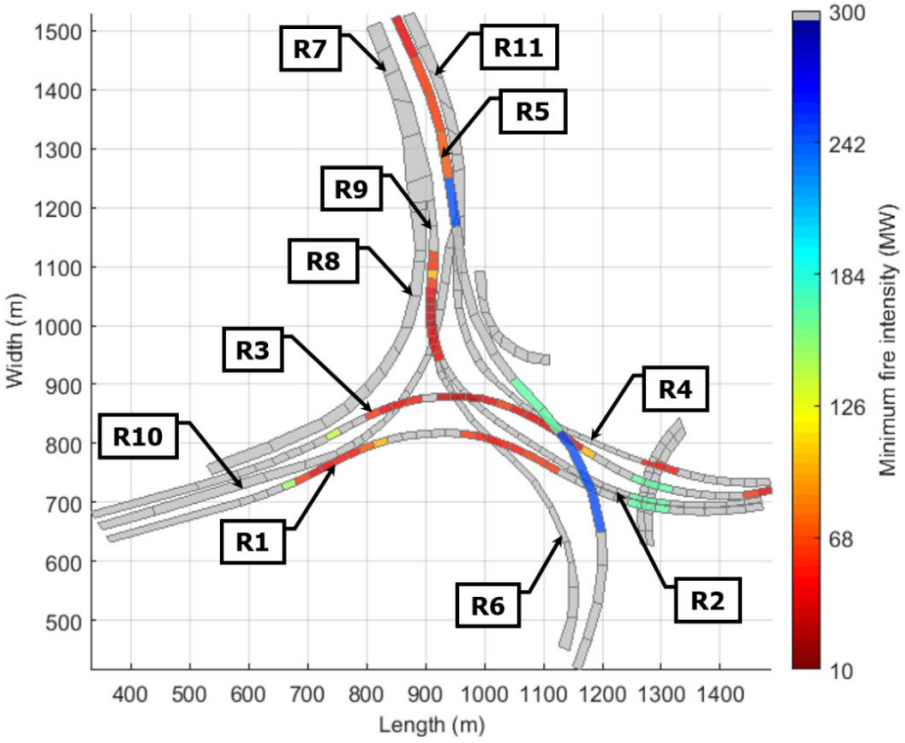

(a) By fire intensity (MW)

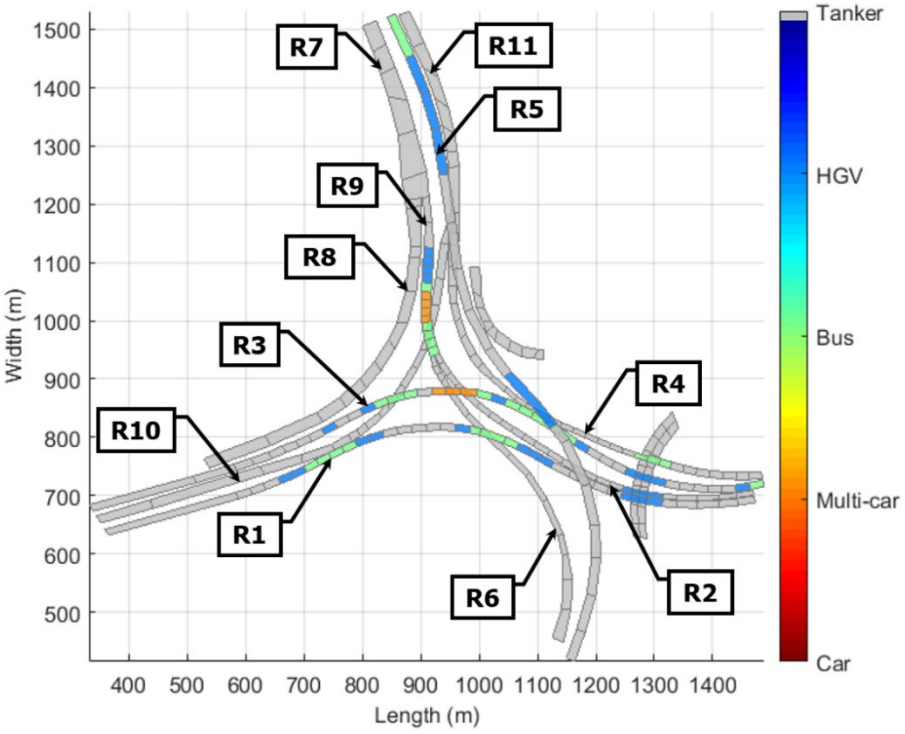

(b) By vehicle type (per NFPA 502[1])

Figure 5-4: Illustrations. Map of minimum fire intensity that would cause "potential" structural damage to the MacArthur Maze highway interchange (all overpass bridges use steel plate girders).

Depending on the damage tolerance or design objectives of the analyst, the influence zones for "potential" structural damage levels from Table 4-4 could also be applied. Since the influence zones for "potential" damage are larger, Figure 5-4 shows that more overpass spans are susceptible to fire, and the minimum fire size that would cause potential damage is smaller than that shown in Figure 5-3 for critical damage. Note that Figure 5-3 and Figure 5-4 are based on the steel girder influence zones since all overpasses in the MacArthur Maze utilized that type of bridge construction. If prestressed concrete bulb-tees had been used for these overpasses, the influence zones for "potential" structural damage levels from Table 4-5 could be applied to obtain a similar map, as shown in Figure 5-5.

5.3 Fire frequency calculation

Per Section 4.4, the calculation of structurally significant fire frequency relies on the traffic information as an input. For this study, the annual average daily traffic (AADT) of R1 to R14 in the MacArthur Maze interchange was obtained from the publicly available Caltrans database for the period between July 2006 and July 2007 (just before the 2007 fire event that caused the R1 collapse) [44]. Using the same approach as in Zhu et al. [44], the traffic volume reported at the inflow and outflow of all roadways in the interchange is correlated to their number of lanes and traffic directions. Traffic volumes at transitions between roadways that merge or fork are estimated by ensuring a conservation of traffic volume that enters or exits the transition. The resulting estimates for AADT on each roadway are summarized in Table 5-1.

The value of the traffic fire rate, R_f, can vary according to region, time period, vehicle type density, roadway geometry, road conditions, etc. [13]. For example, 0.056 fires per million vehicle-km is indicated by the Fatal Accident Reporting System (FARS) database for the period of 2003 to 2008 [102]. Similarly, a value of 0.03 fires per million vehicle-km (i.e. one fire per 19 million vehicle miles) is reported by NFPA [103]. For tunnel roadways, the fire rate can be estimated as 0.01 fires per million vehicle-km per PIARC data for tunnels in eight countries in 2016 [104]. This study uses 0.056 fires per million vehicle-km as a conservative upper-bound estimation for all calculations herein.

The traffic composition for each roadway, which is used to calculate the probability of exceeding a specific fire intensity, is also summarized in Table 5-1. The total truck volume and truck percentage are first calculated using the same strategy for the AADT, again based on the Caltrans database for the period between July 2006 and July 2007. A generic breakdown by vehicle type (based on data provided by PennDOT [13] for typical highways) is applied to the total traffic as follows: 0.35% motorcycles, 79.05% cars, 13.99% pick-up trucks and vans, 0.99% buses, 2.73% 2-axle trucks, 0.91% 3-axle trucks, 0.21% 4-axle trucks, 1.73% 5-axle trucks, 0.041% 6-axle truck and 0.003% 7-axle trucks. It should be noted that vehicle breakdown percentages specific to this site (and specific to each roadway within the site) could be substituted in future assessments; however, the generic breakdown applied to all roadways in this example is suitable for demonstrating this approach. The truck percentages for R1 through R14 are proportionally distributed according to the per-axle truck percentages. The percentages of motorcycles, passenger cars, pick-up trucks, and buses are then redistributed according to the corresponding categories of the PennDOT traffic breakdown, with the summation equal to the total percentage excluding trucks. The combustion weight of each type of vehicle is used to estimate the peak HRR and can range from 30% of the vehicle tare weight up to the full payload capacity of the vehicle plus 30% of the tare weight [13]. For this study, the mean values and standard deviations of combustion weight are calculated as one-third of the difference between the mean value and upper/lower bound, as presented in Table 5-1.

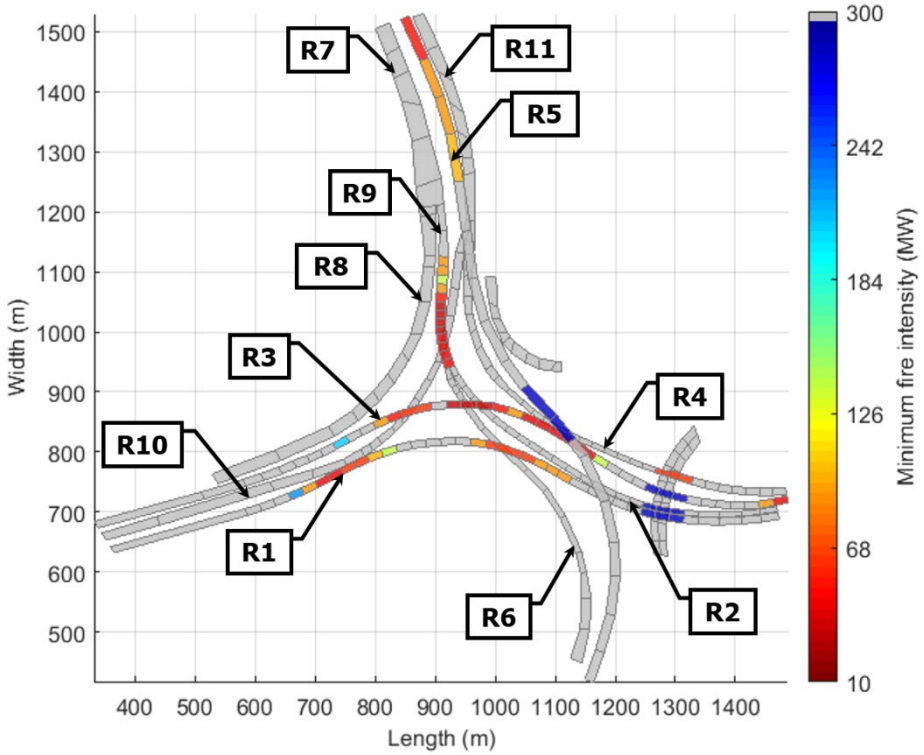

(a) By fire intensity (MW)

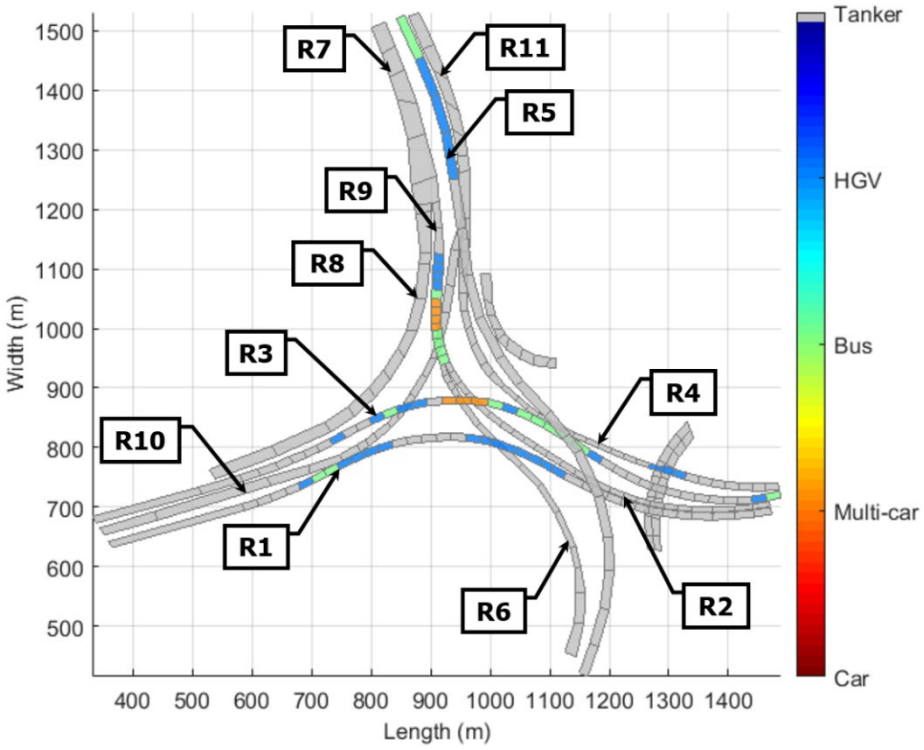

(b) By vehicle type (per NFPA 502[1])

Figure 5-5: Illustrations. Map of minimum fire intensity that would cause "potential" damage to the MacArthur Maze highway interchange if all overpass bridges used concrete bulb-tee girders.

The breakdowns of AADT (Table 5-1) and HRR (Table 5-2) by vehicle type are used to develop a continuous cumulative density function relative to peak HRR for each roadway, which can be generated via one million stochastic HRR samples by using a Monte Carlo Simulation (MCS). The cumulative probability of a specific HRR value is calculated by dividing the number of samples below a given HRR by the total number of samples. For example, Figure 5-6 illustrates the probability density distribution and cumulative probability distribution of roadways R1 and R6. Note that the probability of fire intensity exceeding 80 MW (i.e., the lower bound fire intensity that could cause "critical" structural damage for the collapsed R1 spans in the MacArthur Maze interchange) is 10% given the traffic composition of R6, where the 2007 fire event was located.

The resulting frequency of structural significant fires for each overpass bridge span in MacArthur Maze interchange is plotted in Figure 5-7 according to damage level. Higher frequencies indicate greater vulnerability to fire, thus needing more attention for fire resistant design or evaluation. For example, the structurally "critical" fire frequency for the R1 spans that collapsed due to the 2007 fire event is 0.0029/year, while the "potential" damage frequency is 0.0092/year. Other overpasses that may need attention include the spans of R3 crossing over R6 and R2, for which the "critical" and "potential" damage frequencies are 0.0163/year and 0.026/year (i.e., return periods of 61.3 years and 38.5 years) respectively. These maps indicate that the relative probability of bridge fire damage could be combined with the loss function to enable risk assessment for performance-based decision making. As shown in Figure 5-8, similar maps of fire frequency can be developed is the overpasses instead utilized concrete bulb-tee girders.

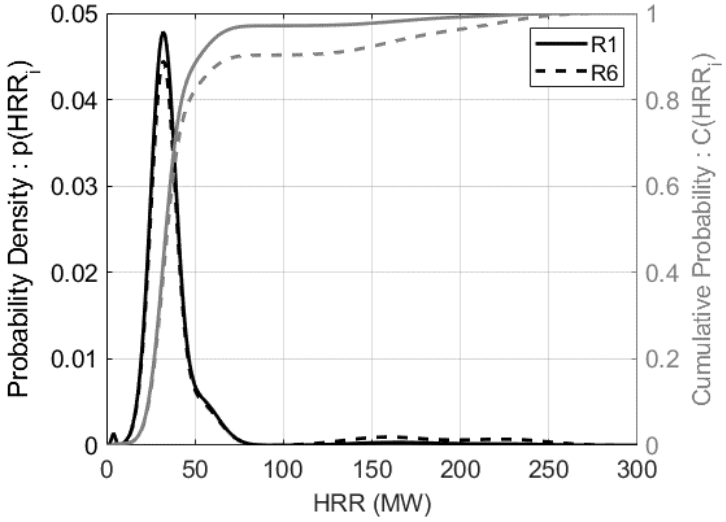

Figure 5-6: Graph. Probability density and cumulative probability distribution of vehicle fire HRR for roadways R1 and R6 in the MacArthur Maze interchange.

Table 5-1: AADT breakdown by vehicle type for the case study of the MacArthur Maze highway interchange.

Roadway Label	AADT	Motorcycle %	Car %	Pickup Truck or Van %	Bus %	2-axle Truck %	3-axle Truck %	4-axle Truck %	5-axle Truck %	6-axle Truck %	7-axle Truck %
R1	51,650	0.360	82.190	14.550	1.030	0.907	0.303	0.070	0.576	0.014	0.001
R2	33,234	0.360	81.870	14.490	1.020	1.094	0.365	0.084	0.694	0.016	0.001
R3	50,938	0.360	82.040	14.520	1.030	0.992	0.331	0.076	0.630	0.015	0.001
R4	32,729	0.360	81.580	14.440	1.020	1.261	0.421	0.097	0.800	0.019	0.001
R5	29,865	0.340	77.160	13.660	0.970	3.823	1.275	0.293	2.427	0.057	0.004
R6	26,508	0.340	76.420	13.530	0.960	4.247	1.417	0.326	2.696	0.063	0.005
R7	96,875	0.350	79.840	14.130	1.000	2.267	0.756	0.174	1.439	0.034	0.002
R8	37,132	0.360	80.470	14.240	1.010	1.903	0.635	0.146	1.208	0.028	0.002
R9	59,742	0.350	79.450	14.060	0.990	2.493	0.832	0.191	1.583	0.037	0.003
R10	21,814	0.360	80.370	14.230	1.010	1.962	0.654	0.150	1.245	0.029	0.002
R11	54,543	0.360	81.090	14.350	1.020	1.541	0.514	0.118	0.978	0.023	0.002
R12	45,408	0.360	82.080	14.530	1.030	0.970	0.324	0.074	0.616	0.014	0.001
R13	14,904	0.360	82.080	14.530	1.030	0.970	0.324	0.074	0.616	0.014	0.001
R14	14,904	0.360	82.080	14.530	1.030	0.970	0.324	0.074	0.616	0.014	0.001

Table 5-2: HRR breakdown by vehicle type for the case study of the MacArthur Maze highway interchange.

HRR (MW)	Motorcycle	Car	Pickup Truck or Van	Bus	2-axle Truck	3-axle Truck	4-axle Truck	5-axle Truck	6-axle Truck	7-axle Truck
Mean Peak Value	4	32	52	170	154	199	220	231	231	231
Standard Deviation	1	7	11	23	22	23	21	21	21	21

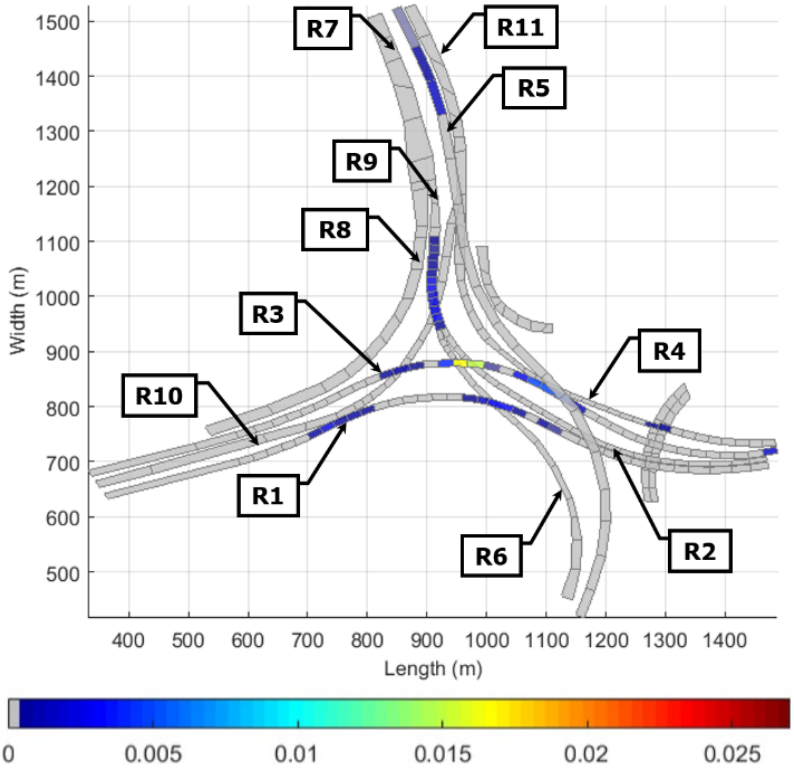

(a) Critical Damage

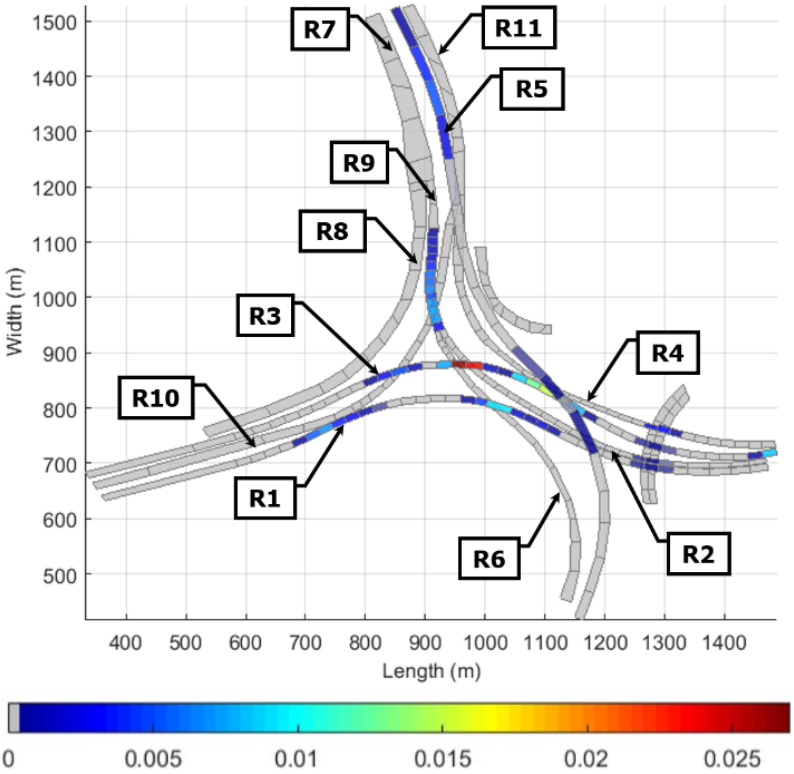

(b) Potential Damage

Figure 5-7: Illustrations. Map of frequency for structurally significant fires for the MacArthur Maze interchange (all overpass bridges use steel plate girders).

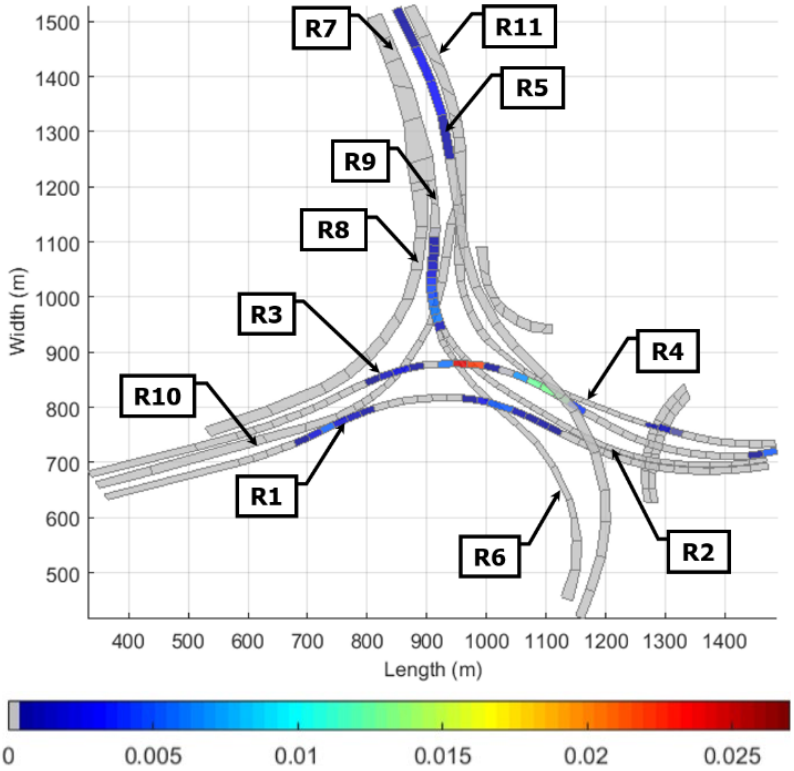

Figure 5-8: Illustration. Map of frequency for fires that would cause "potential" structural damage to the MacArthur Maze interchange if all overpass bridges used concrete bulb-tee girders.

5.4 Risk-based design fire load

For building compartments, the design fire load calculation per NFPA 557[15] [105] consists of two steps: (1) quantify the mean and standard deviation of the fire load through either occupancy-based methods or survey-based methods; and (2) apply a risk objective to estimate a conservative fire load value based on the resulting cumulative probability function. The risk objective, F, is calculated as follows:

$$F = 1 - R_s/f_{ss} \tag{5-1}$$

where R_s is the risk performance criteria for hazardous structural events; and f_{ss} is the annual frequency of structurally significant fires. For the case of a compartment fire in a building, the value of R_s would be taken as no greater than 10^{-6}/year and corresponds to a "collapse" limit state, while f_{ss} would be calculated as the product of fire frequency per fuel unit area and floor area. For a bridge, the value of f_{ss} can be taken as the structurally "critical" fire frequency per Section 4.4, while R_s is the failure probability indicated by the reliability index. The AASHTO LRFD Bridge Design Specification, 9th Edition[2] [2] cites the target reliability index for bridge structural components as 3.5 for a strength limit during a service life of 75 years. For example, this approach is consistent with that used in the HL-93 design live load rating calculation.

[15] NFPA 557, Standard for Determination of Fire Loads for Use in Structural Fire Protection Design, is not a Federal requirement.

The 3.5 reliability index is therefore suggested for this case study, and the fire load is assumed to follow a normal distribution for simplification. The resulting risk performance criteria R_s is 3.06×10^{-6} per year.

The challenge of determining the representative design fire load for bridge evaluation includes selecting the fire intensity thresholds, determining the governing fire locations, and applying the associated risk criteria. To avoid these decisions, the metric of design fire load can instead be reformulated as the maximum heat flux that results from possible fire hazards and their corresponding exposure duration. To arrive at this metric for a given bridge, the following procedure is used:

1. Using NFPA 502, the largest listed fire hazard size for bridges is 300 MW (i.e., a flammable tanker truck fire). The influence zone for a considered damage level at the 300 MW fire size is therefore fitted to the underside of the given bridge as the upper bound (i.e., representing the largest possible prism). For illustration, Figure 5-9 shows the 300 MW influence zones for "critical" structural damage as rectangular prisms for a target span on (a) R1 and (b) R3 in the MacArthur Maze.

2. All roadways below that intersect the 300 MW influence zone of the given bridge provide potential locations where vehicle fire hazards can be located. Figure 5-9 outlines these intersected roadways with yellow dashed lines. Potential fire locations, plotted as gray dots, can be distributed over the surface of these intersected areas. In this case, the locations are evenly distributed at a uniform 5-ft spacing both longitudinally and transversely.

3. Gray-dotted fire locations from all intersected roadways are then stochastically sampled. For this study, each gray-dotted location in the intersected roadway areas is assumed to have an equal likelihood of vehicle fire (though particular locations could be weighted according to available information about the intersected roadway geometry, traffic accident frequency, or other user objectives). The fire intensity for each location is simultaneously sampled from the HRR distribution for the intersected roadway based on its traffic composition (e.g., see Figure 5-6 for R6). When multiple roadways are intersected the influence zone as shown in Figure 5-9b, one of the intersected roadways is selected first based on the relative vehicle fire rate. For example, the fire rates (per day) of the engulfed region on R2, f_{R2}, is calculated as $L_{R2} \cdot AADT_{R2} \cdot TFR$, where TFR is the traffic fire rate (fires per million vehicle-miles from Eq (5-3)). Then, the roadway is randomly selected using the weights of f_{R2}/f_{R6}, after which a gray-dotted location is randomly selected on that roadway.

4. A large number of fire scenarios (approximately 1,000) are generated for the target bridge span with Latin Hypercube Sampling (LHS) and MCS [97]. The maximum heat flux on the target bridge (per Section 3.2) and the fire exposure durations (per Section 2.2) can be calculated for each fire scenario based on their location and intensity. A design fire load for the damage level under consideration can thereby be selected as a statistical threshold per risk objective *F* across the aggregated dataset for all fire scenarios. Due to its computational simplicity versus other methods, the Modified Point Source (MPS) model per Section 3.2.2 is used in this study to efficiently calculate the heat flux on the target bridge from each fire scenario based on its HRR and the minimum standoff from the fire's point source location to any point on the girders of the target bridge. The fire duration is calculated for this study using Ingason's quadratic curve for vehicle fires per Section 2.2.2. Note that different methods could

be chosen based on the fire type, computational demands for the large number of fire scenarios, or based on project-specific information available to the user.

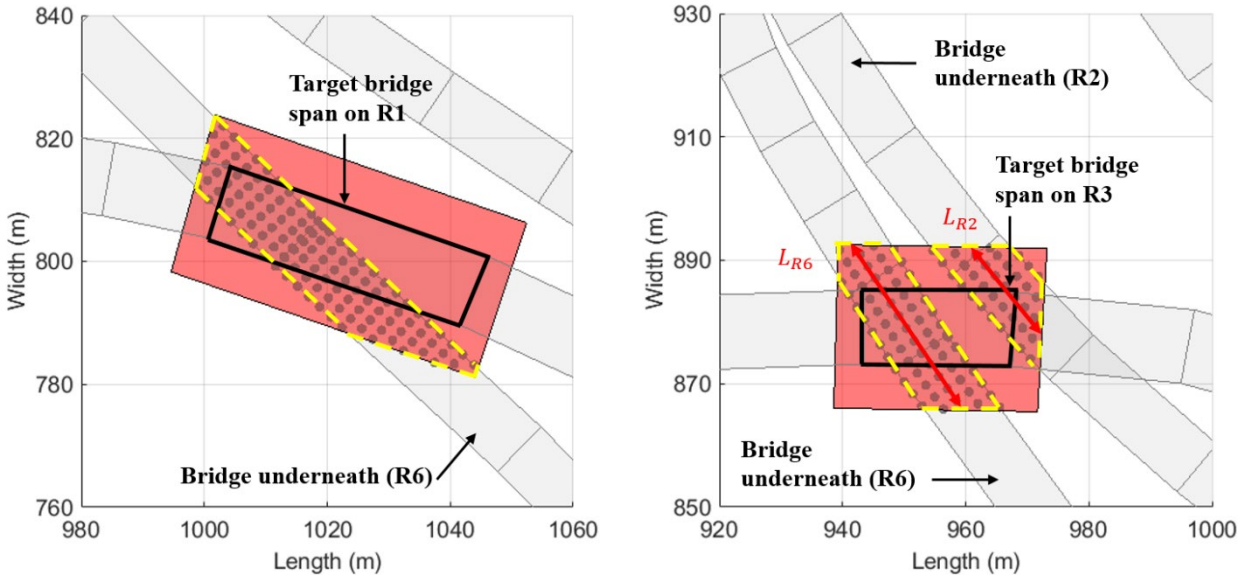

(a) Target bridge span on R1 (b) Target bridge span on R3

Figure 5-9: Illustrations. Potential fire locations selected for bridge design fire load quantification. (the plotted influence zone prism corresponds to a 300 MW tanker truck fire hazard).

As shown in Figure 5-10, the maximum heat flux experienced by the target span on R1 for fires on R6 as shown in Figure 5-9a is primarily concentrated in the interval of 0 to 50 kW/m^2 (due to the large frequency of passenger cars and buses), with a smaller concentration between 120 and 150 kW/m^2 (due to the frequency of larger truck fires). The risk objective F can then calculated as 0.9989 via Eq. (5-1), in which R_S= 3.06×10^{-6}/year and f_{ss}= 0.0029/year, and plotted as a horizontal line at the top of the y-axes in Figure 5-10. The intersection of that line with the cumulative probability curve for maximum heat flux indicates the design heat flux for that risk objective at "critical" structural damage for the steel girder overpass bridge. For this example, the intersection indicates a design heat flux value of 150 kW/m^2. As shown in Figure 5-11, the maximum heat flux experienced by the target span on R3 for fires on R2 and R6 as shown in Figure 5-9b has a significant concentration at the maximum "engulfed" heat flux of 170 kW/m^2, with a smaller concentration at the 10 to 50 kW/m^2 range. The shape of this histogram indicates that this bridge span has a high potential of being engulfed by fire end experiencing "critical" structural damage due to its low clearance to roadways below which have a relatively large area and traffic volume. The risk objective for this R3 span is calculated as 0.9998, where R_S is unchanged but with f_{ss}= 0.0163/year. The design heat flux would thereby be taken as 170 kW/m^2.

It should be noted that the value of the risk performance criteria R_S = 3.06×10^{-6}/year is conservative and will tend to push the design heat flux to the maximum possible value for the target span. Moreover, the "critical" structural frequency (f_{ss}) calculation is also based on the thermal criterion for the bridge girder cross-sections per Section 4.2, which uses the maximum temperature at single location of one girder as the benchmark. In this case, the performance of the entire structure is not analyzed and can offer redundancy, but such an evaluation needs a significant amount of additional analysis and computational effort.

The histogram and cumulative density function (CDF) of fire exposure duration for the R1 and R3 target spans are also plotted in Figure 5-10b and Figure 5-11b, respectively. Based on the selected quadratic time history model, the fire duration shows much less variability based on the fire size and vehicle type, thus generally ranging from 60 to 80 min. For design purposes, the design value could be conservatively and consistently taken as 90 min to simplify the design fire quantification process. Again, the selection of a different fire type or time history calculation approach would impact this selection.

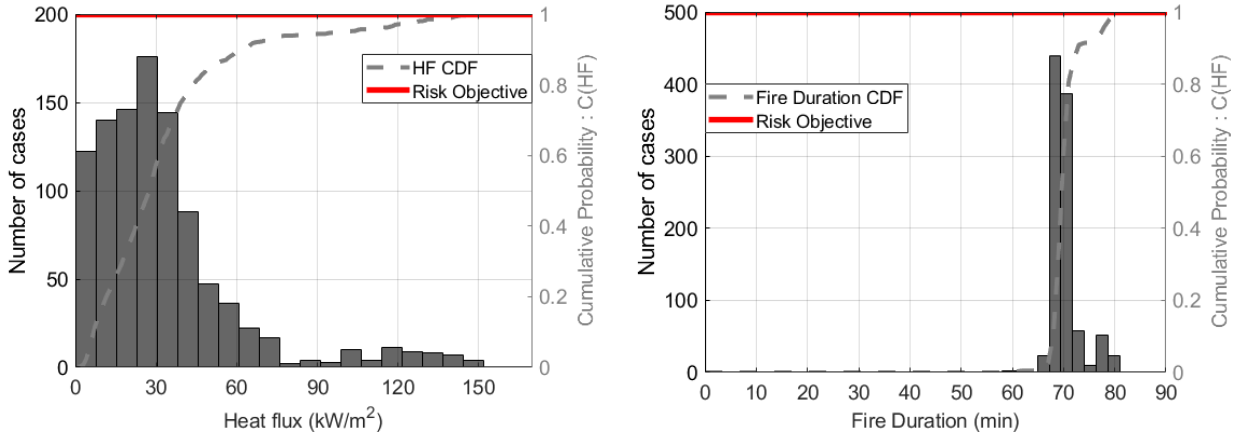

(a) Maximum heat flux (b) Exposure time

Figure 5-10: Graphs. Histogram and cumulative probability for design fire quantification for bridge span on R1.

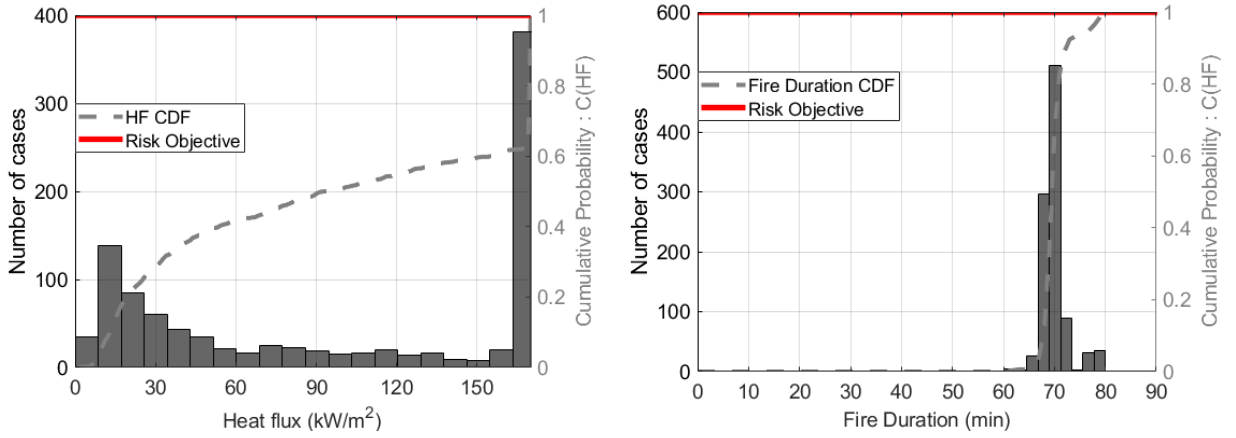

(a) Maximum heat flux (b) Exposure time

Figure 5-11: Graphs. Histogram and cumulative probability for design fire quantification for bridge span on R3.

This quantification process can be applied to every bridge span in the MacArthur Maze highway interchange, and the resulting map of the design fire load in terms of maximum heat flux is plotted in Figure 5-12. The spans of R3 crossing over R2, R6, and R10, as well as multiple spans of R9 crossing over R10, should be designed for the thermal impact of 170 kW/m^2 from potential fire hazards over their lifecycle. Likewise, the spans of R5 that are above and alongside R11 could be designed using a smaller design load ranging from 20 to 60 kW/m^2. These results indicate not only a design fire load in terms of heat flux but

also suggest relative vulnerability to vehicle fire hazards. A similar evaluation could be performed for fire hazards from stationary fuels, for which an associated fire frequency would need to be determined and applicable fire models would need to be selected. A similar evaluation could also be conducted for other types of bridge structures, such as those supported by cables or trusses, by developing a different set of fire damage classifications and influence zones for the elements of interest.

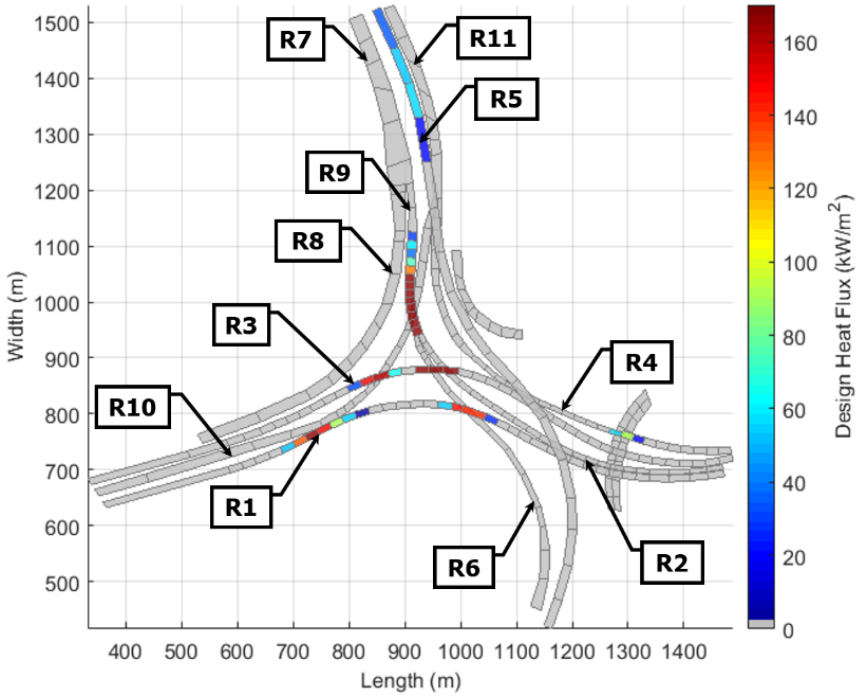

Figure 5-12: Illustration. Map of design heat flux for steel girder overpass bridges in the MacArthur Maze highway interchange.

5.5 Simplified design fire calculation

The approach for quantifying design fire load, as illustrated for MacArthur Maze interchange, needs large suites (i.e. thousands) of stochastic analyses and may not be conducive for practicing engineers to determine fire vulnerability for common overpass girder bridges, particularly during the early stages of an evaluation or design process. In this section, large sets of pre-calculated data are therefore used to provide a conservative closed-form expression of design fire load for overpass girder bridges based on the fundamental characteristics of the overpass, the relative standoff to potential vehicle fire locations, and the traffic of the nearby roadways below.

Spatial parameters that influence the design heat flux include the bridge clearance, relative location of the fire in the longitudinal and transverse directions, and the relative angle of roadway orientations. In terms of the traffic, the AADT and truck percentage on the roadways with potential fire locations are the primary variables. To streamline the development of the closed-form expression, a preliminary sensitivity analysis was performed to investigate the relative importance of these parameters and identify those that would carry the most weight in the resulting calculation of design fire load. The preliminary data set was obtained via MCS considering the five independent variables as illustrated in Figure 5-13a: Δy, θ, Δz, AADT, and truck

percentage (TP). Note that Δx is omitted since the roadway underneath is assumed to be unlimited in length. The value of Δy, θ, and Δz, which describe the relative position of the fire locations to the target bridge span, are randomly and uniformly selected from the intervals of 0–100 ft, 0–90°, and 5–30 ft, respectively. The AADT and truck percentage are similar selected from ranges of 10,000 to 200,000 and 0% to 20%, respectively.

A total of 1,000 cases are generated via LHS with MCS with these five inputs and then used to determine the design fire load per the process introduced in Section 4.4. Available methods for conducting such a sensitivity analysis include the sample-based method of the standard regression coefficient, the linearization method of the Perturbation method, the Cotter method and global methods of Sobol's indices, Borgonovo indices, or ANCOVA indices [106], as well as machine learning method such as the random forest [107]. In this study, the method of Borgonovo indices is applied due to the relative simplicity of its output compared to other methods. Borgonovo indices of the input parameters measure the expected shift in the probability distribution of the output when the input is set to a fixed value. This method is suitable for evaluating nonlinear problems and can accommodate both dependent and independent variables, which is well suited for the consideration of bridge fire hazards in this study.

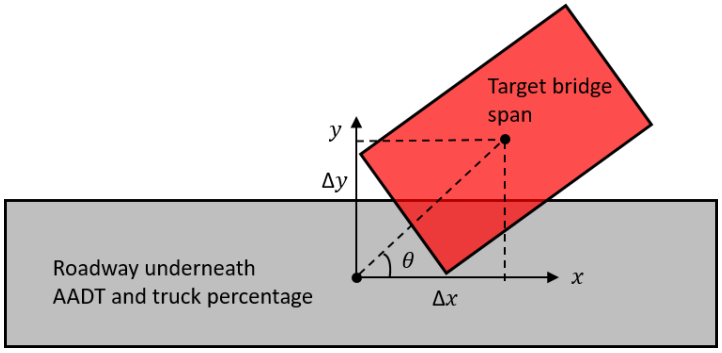

(a) For sensitivity analysis

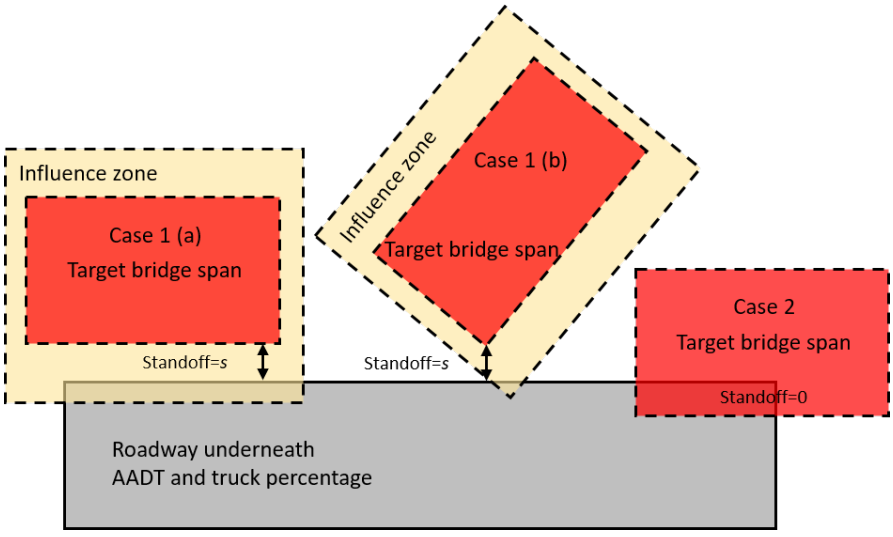

(b) For closed-form expression development

Figure 5-13: Illustrations. Plan view of the relative position of an overpass bridge span to roadways underneath.

The Borgonovo indices of the five aforementioned inputs are plotted in Figure 5-14, which shows that clearance Δz has the greatest impact on the design fire load, with Δy ranking second. The effects of the rotation angle θ, AADT, and TP on the design fire load are comparable but lesser. The rotation angle combined with the Δy determines the closest plane distance from the bridge to the roadways underneath (i.e., to the area of the roadways engulfed by the influence zone of interest). The truck percentage influences the maximum HRR value to select in the stochastic analysis for the design fire load quantification. The AADT affects the "critical" structural fire frequency, which is calculated via Eq. (4-5). Hence, the closed-form expression could initially select upper-bound values for the truck percentage and AADT of 20% and 200,000/year, respectively, as a conservative estimation. The rotation angle is also conservatively neglected, and the bridge is therefore considered parallel to the roadway underneath. Correspondingly, the relative plane location is described with a single parameter s, which represents the horizontal standoff in plan from the bridge to the roadway below as illustrated in Figure 5-13b. For example, when the target bridge span overlaps the roadway underneath (as shown in Figure 5-13a and Case 2 of Figure 5-13b), the lateral standoff s is considered to be zero. When the target bridge span has a standoff s to the roadway, the parallel Case 1(a) would be more critical than the rotated bridge span in Case 1(b) because the overlapped area would be the larger with zero angle of relative rotation.

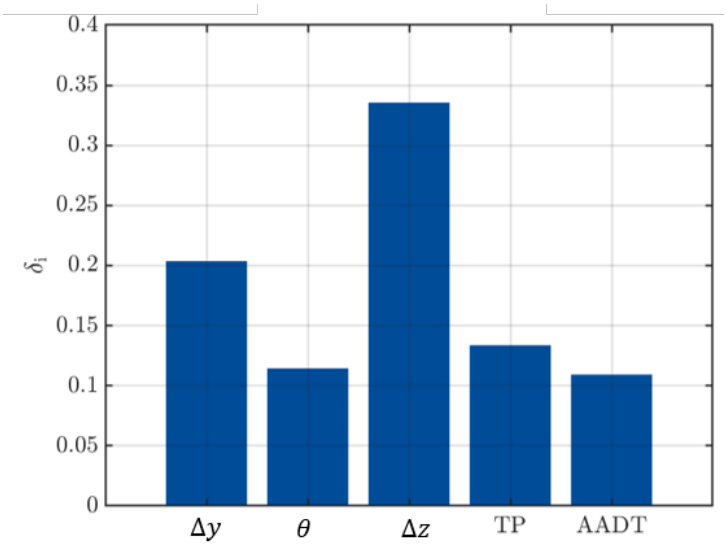

Figure 5-14: Chart. Histogram of Borgonovo indices of major parameters for design fire heat flux quantification.

From the sensitivity analysis above, the design-basis fire load, $\dot{q}_D^{''}$ (kW/m^2), can be determined as a function of the horizontal standoff distance, s (m), from the fire footprint to the nearest bridge element and the vertical clearance from the bridge element to the fuel source at the base of the fire, Δz (m). The value of standoff s is systematically varied from 0 (i.e., directly underneath the bridge) to 27.43 m (90 ft), and the value of clearance Δz is systematically varied from 1.52 m (5 ft) to 12.2 m (40 ft). The resulting value of $\dot{q}_D^{''}$ for each pairing of Δz and s is calculated following the process introduced in Sections 3 and 4, then plotted as dots in Figure 5-15. The results indicate that the design load stays at its maximum "engulfed" value (170 kW/m^2) when the standoff and clearance are small and then decreases as these two parameters

increase. These data points are then fitted with a polynomial equation, combined with a plateau at the engulfed value:

$$\textit{for } s \le 2\ m \textit{ and } \Delta z \le 6.4\ m: \quad \dot{q}_D'' = 170 \tag{5-2a}$$

$$\textit{for } s > 2\ m \textit{ or } \Delta z > 6.4\ m: \quad \dot{q}_D'' = 170 + p_1 \cdot \bar{s}^a + p_2 \cdot \overline{\Delta z}^b + p_3 \cdot \bar{s}^a \cdot \overline{\Delta z}^b \tag{5-2b}$$

$$\textit{normalized standoff:} \quad \bar{s} = s/7.16 \tag{5-2c}$$

$$\textit{normalized clearance:} \quad \overline{\Delta z} = (\Delta z - 1.52)/7.32 \tag{5-2d}$$

The values for the parameters in Eq. (5-2b) are based on a surface fit as shown below in in Figure 5-15 (which has an R-squared value of 0.944 versus the data points): p_1 = -148.7, p_2 = -118.4, p_3 = 108.3, a = 1.49, and b = 3.42.

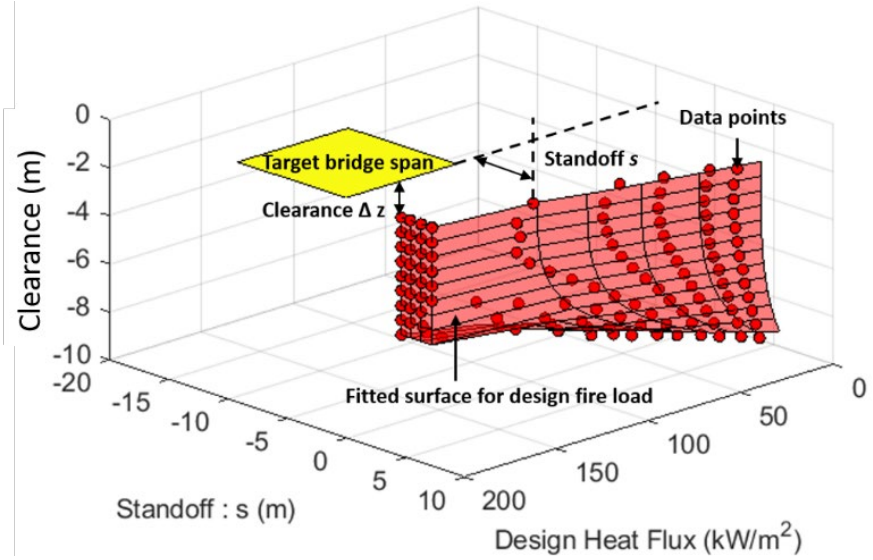

Figure 5-15: Graph. Design fire load as a function of clearance and standoff beneath a bridge, with fitted surface plotted per Eq. (5-2).

This closed-form expression is used to calculate the design fire load of each bridge span of the MacArthur Maze interchange, and the resulting map is presented in Figure 5-16. Compared to the stochastic analysis results in Figure 5-12, the closed-form expression is more conservative but shows good overall agreement. Hence, the closed-form expression can provide a conservative preliminary estimate of the design fire load in terms of maximum heat flux. For a more precise value, however, the stochastic method per Sections 5.1 through 5.4 can be applied.

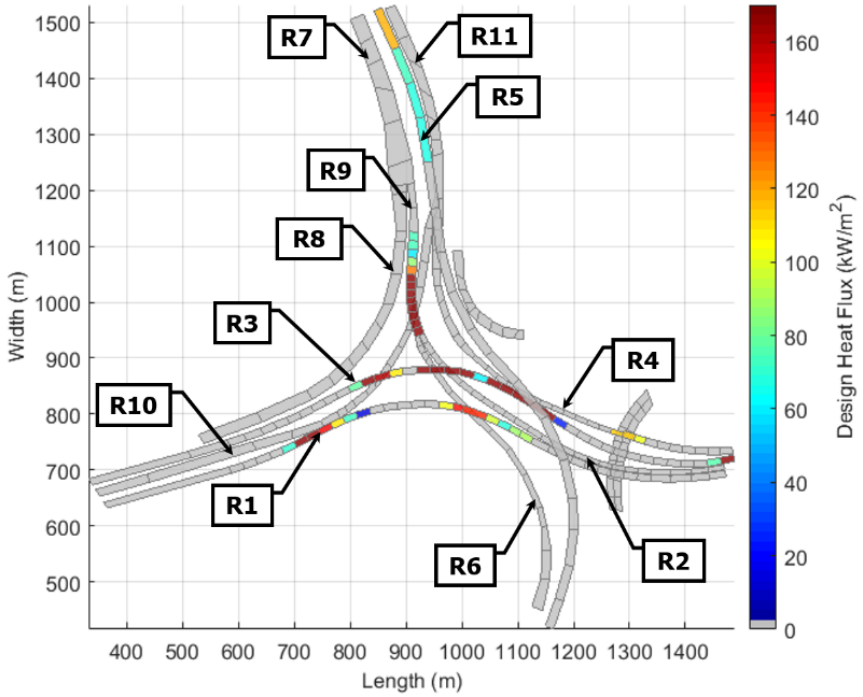

Figure 5-16: Illustration. Map of design heat flux for the MacArthur Maze highway interchange at a "critical" structural damage threshold per Eq. (5-2) (all overpass bridges use steel plate girders).

6 SUMMARY AND CONCLUSIONS

This report provides information for evaluating the vulnerability of highway bridges to structurally significant fire hazards. Specifically, the results of this study address the selection of a design fire scenario which accounts for the types of vehicles passing under or near the bridge, as well as any other stationary fuel sources that are stored or staged near the bridge. Thermal exposure from the design fire can provide the thermal load in a performance-based structural-fire engineering evaluation of the bridge's primary structural system (to satisfy the "engineering analysis" per NFPA 502[1] Chapter 6 [1]).

Available methods to calculate the fire intensity in terms of peak HRR and time history were presented in Section 2 for a variety of fire configurations and fuel types that can affect bridges. The fire's HRR time history is then used to calculate the heat transfer to the bridge's structural elements, as presented in Section 3. The time history of heat flux (units: kW/m^2) experienced by the exposed surfaces of the structural element on a direct line of sight to the fire is considered the thermal load. In this study, two typical bridge girder sections are evaluated for their response to heat exposure from typical fires: a steel I-section plate girder, and a prestressed concrete bulb-tee girder. The thermo-structural response of a bridge to fire hazards depends on its span length, supports (i.e., simply supported vs. continuous), section geometry, structural materials, applied loading, and boundary conditions. Critical temperature limits cited from available references [1,80,81,89,90,96] are used to indicate the onset of structural damage in terms of temperature increase [44]. This study implements two levels of damage severity based on thermal response as a method to rapidly screen bridges for vulnerability to a given fire hazard. The standoff radius (or zone of influence) at which a given fire intensity can be located to cause a particular level of damage to a bridge girder is determined by coupling these damage classifications with the calculated heat flux time history from fires at a range of locations. These influence zones, corresponding to a particular level of structural damage, are visually represented as a three-dimensional prism that surrounds the bridge's structural elements.

The exposure frequency of a highway bridge to fire-induced structural damage is used as a metric for risk assessment. Section 4 outlines a performance-based framework to develop this metric as a function of the bridge's relative location to potential fire locations as well as the likelihood of having a fire with a given intensity at those locations. The frequency of having a structurally significant fire within the influence zones for a target bridge is quantified by examining the length and associated traffic volume of roadways that pass through the zone's rectangular prism for a given fire intensity. A design fire load is then selected using a risk-based approach that couples the frequency of structurally significant fires with a risk objective consistent with the expected failure probability of bridge components in the service lifetime. Section 5 presents a case study demonstrating this approach. A simplified closed-form expression is developed to calculate the maximum heat flux and exposure duration as the design fire load. The most critical parameters influencing the design fire load are the standoff and clearance from the closest roadways or other fuel locations to a given bridge span.

The results of this study are applicable for estimating the vulnerability of highway bridge structures to potential fire hazards. The design-basis fire load provides the input for a thermo-structural evaluation of vulnerable bridges, by which the bridge's structural response to that fire exposure can be calculated. Once the potential consequences of design-basis fire exposure are determined (in terms of collapse resistance and/or the residual post-fire condition), then decisions can be made regarding potential strategies for mitigating the risk of fire-induced damage.

7 REFERENCES

[1] NFPA. NFPA 502: Standard for road tunnels, bridges, and other limited access highways. Quincy, MA: National Fire Protection Association; 2023.

[2] AASHTO. AASHTO LRFD Bridge Design Specifications, 9th Edition. Washington, D.C.: American Association of State Highway and Transportation Officials; 2020.

[3] Lee GC, Mohan SB, Huang C, Fard BN. Technical Report MCEER-13-0008: A Study of U.S. Bridge Failures (1980-2012). Buffalo, NY: MCEER, University at Buffalo, State University of New York; 2013.

[4] Wardhana K, Hadipriono FC. Analysis of Recent Bridge Failures in the United States. J Perform Constr Facil 2003;17:144–50. https://doi.org/10.1061/(ASCE)0887-3828(2003)17:3(144).

[5] Garlock M, Paya-Zaforteza I, Kodur V, Gu L. Fire hazard in bridges: Review, assessment and repair strategies. Engineering Structures 2012;35:89–98. https://doi.org/10.1016/j.engstruct.2011.11.002.

[6] Kodur V, Aziz E, Dwaikat M. Evaluating Fire Resistance of Steel Girders in Bridges. Journal of Bridge Engineering 2013;18:633–43. https://doi.org/10.1061/(ASCE)BE.1943-5592.0000412.

[7] Kodur V, Gu L, Garlock MEM. Review and Assessment of Fire Hazard in Bridges. Transportation Research Record 2010;2172:23–9. https://doi.org/10.3141/2172-03.

[8] Aziz EM. Response of Fire-Exposed Steel Bridge Girders. Doctoral Dissertation. Michigan State University, 2015.

[9] Miller M. Fire-damaged Route 22 eastbound bridge at I-81 near Harrisburg to reopen this month, PennDOT says. Pennlive Patriot-News 2013. https://www.pennlive.com/midstate/2013/11/fire-damaged_i-81_ramps_near_h.html (accessed March 18, 2022).

[10] Liberty Bridge Fire. CBS Pittsburgh 2016. https://pittsburgh.cbslocal.com/tag/liberty-bridge-fire/ (accessed March 8, 2022).

[11] 11 Alive staff. The fire that caused the I-85 bridge to collapse was four years ago today. 11 Alive 2021. https://www.11alive.com/article/news/local/i-85-bridge-fire-collapse-was-four-years-ago-today/85-7dd0ccb8-6f43-4e87-81fd-21075c2c7a27 (accessed March 8, 2022).

[12] NFPA. NFPA 502: Standard for road tunnels, bridges, and other limited access highways. Quincy, MA: National Fire Protection Association; 2017.

[13] Guo Q, Quiel SE, Naito CJ. Traffic-based quantitative risk analysis of structural fire damage to roadway tunnel linings. Structure and Infrastructure Engineering 2021:1–17. https://doi.org/10.1080/15732479.2021.1993936.

[14] Sturm P, Fößleitner P, Fruhwirt D, Galler R, Wenighofer R, Heindl SF, et al. Fire tests with lithium-ion battery electric vehicles in road tunnels. Fire Safety Journal 2022;134:103695. https://doi.org/10.1016/j.firesaf.2022.103695.

[15] Guo Q, Carlton A, Quiel SE, Naito CJ. Stochastic Thermal Demand and Resulting Capacity Loss of Concrete Tunnel Liners Subjected to Vehicle Fires. Transportation Research Record 2020;2674:293–304. https://doi.org/10.1177/0361198120914612.

[16] Ingason H. Design fire curves for tunnels. Fire Safety Journal 2009;44:259–65. https://doi.org/10.1016/j.firesaf.2008.06.009.

[17] Ingason H. Design Fires in Tunnels. Proc. of Safe & Reliable Tunnels, Innovative European Achievements, Lausanne, Switzerland: 2006, p. 77–95.

[18] Chuang Y-J, Tang C-H, Chen P-H, Lin C-Y. Experimental Investigation of Burning Scenario of Loaded 3.49-Ton Pickup Trucks. Journal of Applied Fire Science 2005;14:27–46.

[19] Haack A. Fire protection in traffic tunnels: General aspects and results of the EUREKA project. Tunnelling and Underground Space Technology 1998;13:377–81.

[20] Brousse B, Voeltzel A, Boltlan YL, Ruffin E. Ventilation and fire tests in the Mont-Blanc tunnel to better understand and the catastrophic fire of 24 March 1999. Proc. of Tunnel Fires and Escape From Tunnels, 3rd International Conference, Washington, D.C.: 2001, p. 211–22.

[21] Cheong MK, Cheong WO, Leong KW, Lemaire AD, Noordijk LM. Heat Release Rate of Heavy Goods Vehicle Fire in Tunnels with Fixed Water Based Fire-Fighting System. Fire Technology 2014;50:249–66.
[22] Ingason H, Li YZ, Lönnermark A. Runehamar tunnel fire tests. Fire Safety Journal 2015;71:134–49.
[23] Lönnermark A. On the Characteristics of Fires in Tunnels. Doctoral Dissertation. Lund University, 2005.
[24] Zhu Z, Quiel SE. Near-Field Radiant Heat Flux from Open-Air Gasoline and Diesel Pool Fires: Modified Point Source and Discretized Solid Flame Models. Fire Technology 2021. https://doi.org/10.1007/s10694-021-01097-y.
[25] Sjöström J, Amon F, Appel G, Persson H. Thermal exposure from large scale ethanol fuel pool fires. Fire Safety Journal 2015;78:229–37. https://doi.org/10.1016/j.firesaf.2015.09.003.
[26] Babrauskas V. Chapter 26: Heat Release Rates. In: Hurley MJ, editor. SFPE Handbook of Fire Protection Engineering, vol. I. 5th Edition, New York, NY: Society of Fire Protection Engineering; 2016, p. 799–904.
[27] Iqbal N, Salley MH. NUREG-1805: Fire Dynamics Tools (FDTs): Quantitative Fire Hazard Analysis Methods for the U.S. Nuclear Regulatory Commission Fire Protection Inspection Program. Washington, D.C.: US Nuclear Regulatory Commission; 2004.
[28] NTSB. NTSB/HAB-18/02: Fire Damage to Bridge and Subsequent Collapse, Atlanta, Georgia. Washington, D.C.: National Transportation Safety Board; 2017.
[29] NTSB. SA-073: Protecting Bridges From Fire Damage and Collapse. Washington, D.C.: National Transportation Safety Board; 2018.
[30] Biondi E, Kalla H. Memorandum: Documentation and Treatment of Materials Stored Under a Highway Bridge. Washington, D.C.: Federal Highway Administration; 2023.
[31] Buchanan AH, Abu A. Structural design for fire safety. Second edition. Chichester, West Sussex, United Kingdom: John Wiley & Sons Inc; 2017.
[32] Khorasani NE, Garlock M, Gardoni P. Fire load: Survey data, recent standards, and probabilistic models for office buildings. Engineering Structures 2014;58:152–65. https://doi.org/10.1016/j.engstruct.2013.07.042.
[33] Quiel SE, Zhu Z. Numerical Evaluation of a Sample Steel Girder Bridge for a Construction Trailer Fire Underneath (ATLSS Report No. 18-03). Bethlehem, PA: Advanced Technology for Large Structural Systems (ATLSS) Engineering Research Center; 2019.
[34] Ingason H, Lönnermark A. Heat release rates from heavy goods vehicle trailer fires in tunnels. Fire Safety Journal 2005;40:646–68.
[35] Lönnermark A, Ingason H. Recent Achievements Regarding Heat Release and Temperatures during Fires in Tunnels. Safety in Infrastructure, Budapest: 2004, p. 9.
[36] Lacroix D. New French recommendations for fire ventilation in road tunnels. 9th International Conference on Aerodynamics and Ventilation of Vehicle Tunnels, Aosta Valley, Italy,: 1997.
[37] Marlair G, Lemaire T, Ohlin M. Fire Scenarios and Accidents in the Past – Draft Final Report (1) task 2.1,part1, UPTUN WP2 Report. 2008.
[38] Quiel SE, Yokoyama T, Bregman LS, Mueller KA, Marjanishvili SM. A streamlined framework for calculating the response of steel-supported bridges to open-air tanker truck fires. Fire Safety Journal 2015;73:63–75. https://doi.org/10.1016/j.firesaf.2015.03.004.
[39] Alos-Moya J, Paya-Zaforteza I, Hospitaler A, Loma-Ossorio E. Valencia bridge fire tests: Validation of simplified and advanced numerical approaches to model bridge fire scenarios. Advances in Engineering Software 2019;128:55–68. https://doi.org/10.1016/j.advengsoft.2018.11.003.
[40] Bajwa CS, Easton EP, Adkins H, Cuta J, Klymyshyn N, Suffield S. The MacArthur Maze Fire and Roadway Collapse: A “Worst Case Scenario” for Spent Nuclear Fuel Transportation? ASME 2012 Pressure Vessels and Piping Conference, American Society of Mechanical Engineers; 2012, p. 261–9.

[41] Wright W, Lattimer B, Woodworth M, Nahid M, Sotelino E. NCHRP 12-85: Highway Bridge Fire Hazard Assessment, Draft Final Report. Blacksburg, VA: Virginia Polytechnic Institute and State University; 2013.
[42] Peris-Sayol G, Paya-Zaforteza I, Alos-Moya J, Hospitaler A. Analysis of the influence of geometric, modeling and environmental parameters on the fire response of steel bridges subjected to realistic fire scenarios. Computers & Structures 2015;158:333–45. https://doi.org/10.1016/j.compstruc.2015.06.003.
[43] Alos-Moya J, Paya-Zaforteza I, Garlock MEM, Loma-Ossorio E, Schiffner D, Hospitaler A. Analysis of a bridge failure due to fire using computational fluid dynamics and finite element models. Engineering Structures 2014;68:96–110. https://doi.org/10.1016/j.engstruct.2014.02.022.
[44] Zhu Z, Quiel SE, Carlton A, Mueller KA, Marjanishvili SM. Performance-based prioritisation of fire protection for steel girder overpasses in a complex highway interchange. Structure and Infrastructure Engineering 2020;16:394–411. https://doi.org/10.1080/15732479.2019.1666884.
[45] Bennetts I, Moinuddin K. Evaluation of the Impact of Potential Fire Scenarios on Structural Elements of a Cable-Stayed Bridge. Journal of Fire Protection Engineering 2009;19:85–106. https://doi.org/10.1177/1042391508095091.
[46] McGrattan KB, McDermott RJ, Weinschenk CG, Forney GP. Fire Dynamics Simulator, Technical Reference Guide, Sixth Edition. Special Publication (NIST SP) - 1018 2013.
[47] Guo Q, Root KJ, Carlton A, Quiel SE, Naito CJ. Framework for rapid prediction of fire-induced heat flux on concrete tunnel liners with curved ceilings. Fire Safety Journal 2019;109:102866. https://doi.org/10.1016/j.firesaf.2019.102866.
[48] Ang CD (Edmund), Rein G, Peiro J, Harrison R. Simulating longitudinal ventilation flows in long tunnels: Comparison of full CFD and multi-scale modelling approaches in FDS6. Tunnelling and Underground Space Technology 2016;52:119–26. https://doi.org/10.1016/j.tust.2015.11.003.
[49] Cheong MK, Spearpoint MJ, Fleischmann CM. Calibrating an FDS Simulation of Goods-vehicle Fire Growth in a Tunnel Using the Runehamar Experiment. Journal of Fire Protection Engineering 2009;19:177–96. https://doi.org/10.1177/1042391508101981.
[50] Guo X, Zhang Q. Analytical solution, experimental data and CFD simulation for longitudinal tunnel fire ventilation. Tunnelling and Underground Space Technology 2014;42:307–13. https://doi.org/10.1016/j.tust.2014.03.011.
[51] Wang P, Fan F, Li Q. Accuracy evaluation of the gray gas radiation model in CFD simulation. Case Studies in Thermal Engineering 2014;3:51–8. https://doi.org/10.1016/j.csite.2014.03.003.
[52] Hostikka S, Mcgrattan K, Hamins A. Numerical Modeling Of Pool Fires Using Les And Finite Volume Method For Radiation. Fire Safety Science 2003;7:383–94. https://doi.org/10.3801/IAFSS.FSS.7-383.
[53] Beyler CL. Chapter 66: Fire Hazard Calculations for Large, Open Hydrocarbon Fires. SFPE Handbook of Fire Protection Engineering, vol. III. 5th Edition, New York, NY: Society of Fire Protection Engineering; 2016, p. 2591–663.
[54] Mudan KS. Thermal radiation hazards from hydrocarbon pool fires. Progress in Energy and Combustion Science 1984;10:59–80. https://doi.org/10.1016/0360-1285(84)90119-9.
[55] Shokri M, Beyler CL. Radiation from Large Pool Fires. Journal of Fire Protection Engineering 1989;1:141–9. https://doi.org/10.1177/104239158900100404.
[56] Quiel SE, Yokoyama T, Bregman LS, Mueller KA, Marjanishvili SM. A streamlined framework for calculating the response of steel-supported bridges to open-air tanker truck fires. Fire Safety Journal 2015.
[57] Heskestad G. Luminous heights of turbulent diffusion flames. Fire Safety Journal 1983;5:103–8. https://doi.org/10.1016/0379-7112(83)90002-4.
[58] McGrattan KB, Baum HR, Hamins A. NISTIR 6546: Thermal radiation from large pool fires. Gaithersburg, MD: National Institute of Standards and Technology; 2000. https://doi.org/10.6028/NIST.IR.6546.

[59] Muñoz M, Planas E, Ferrero F, Casal J. Predicting the emissive power of hydrocarbon pool fires. Journal of Hazardous Materials 2007;144:725–9. https://doi.org/10.1016/j.jhazmat.2007.01.121.
[60] Thomas PH. The size of flames from natural fires. Symposium (International) on Combustion 1963;9:844–59. https://doi.org/10.1016/S0082-0784(63)80091-0.
[61] Kent JH. A quantitative relationship between soot yield and smoke point measurements. Combustion and Flame 1986;63:349–58. https://doi.org/10.1016/0010-2180(86)90004-0.
[62] Munoz M, Arnaldos J, Casal J, Planas E. Analysis of the geometric and radiative characteristics of hydrocarbon pool fires. Combustion and Flame 2004;139:263–77. https://doi.org/10.1016/j.combustflame.2004.09.001.
[63] Quiel SE, Yokoyama T, Bregman LS, Mueller KA, Marjanishvili SM. A streamlined framework for calculating the response of steel-supported bridges to open-air tanker truck fires. Fire Safety Journal 2015;73:63–75. https://doi.org/10.1016/j.firesaf.2015.03.004.
[64] Hägglund B, Persson L-E. FOA Report C 20126-D6 (A3): The Heat Radiation from Petroleum Fires. Stockholm, Sweden: Research Institute of National Defence; 1976.
[65] Hurley MJ, Gottuk D, Hall JR, Harada K, Kuligowski E, Puchovsky M, et al., editors. SFPE Handbook of Fire Protection Engineering. New York, NY: Springer New York; 2016. https://doi.org/10.1007/978-1-4939-2565-0.
[66] Russell LH, Canfield JA. Experimental Measurement of Heat Transfer to a Cylinder Immersed in a Large Aviation-Fuel Fire. Journal of Heat Transfer 1973;95:397–404. https://doi.org/10.1115/1.3450070.
[67] Planas-Cuchi E, Chatris JM, López C, Arnaldos J. Determination of Flame Emissivity in Hydrocarbon Pool Fires Using Infrared Thermography. Fire Technology 2003;39:261–73. https://doi.org/10.1023/A:1024193515227.
[68] Raj VC, Prabhu SV. Measurement of geometric and radiative properties of heptane pool fires. Fire Safety Journal 2018;96:13–26. https://doi.org/10.1016/j.firesaf.2017.12.003.
[69] Sudheer S, Prabhu SV. Measurement of Flame Emissivity of Hydrocarbon Pool Fires. Fire Technology 2012;48:183–217. https://doi.org/10.1007/s10694-010-0206-5.
[70] Sudheer S, Prabhu SV. Characterization of hexane pool fires using infrared thermography. Journal of Fire Sciences 2013;31:143–65. https://doi.org/10.1177/0734904112459260.
[71] Sudheer S, Prabhu SV. Measurement of flame emissivity of gasoline pool fires. Nuclear Engineering and Design 2010;240:3474–80. https://doi.org/10.1016/j.nucengdes.2010.04.043.
[72] Zhou K, Liu N, Zhang L, Satoh K. Thermal Radiation from Fire Whirls: Revised Solid Flame Model. Fire Technology 2014;50:1573–87.
[73] Shen G, Zhou K, Wu F, Jiang J, Dou Z. A Model Considering the Flame Volume for Prediction of Thermal Radiation from Pool Fire. Fire Technology 2019;55:129–48. https://doi.org/10.1007/s10694-018-0779-y.
[74] Zhou K, Liu N, Lozano JS, Shan Y, Yao B, Satoh K. Effect of flow circulation on combustion dynamics of fire whirl. Proceedings of the Combustion Institute 2013;34:2617–24. https://doi.org/10.1016/j.proci.2012.06.053.
[75] Zukoski EE, Cetegen BM, Kubota T. Visible structure of buoyant diffusion flames. Symposium (International) on Combustion 1985;20:361–6. https://doi.org/10.1016/S0082-0784(85)80522-1.
[76] The MathWorks, Inc. MATLAB and Statistics Toolbox. Natick, Massachussetts: 2017.
[77] Spinti JP, Thornock JN, Eddings EG, Smith PJ, Sarofim AF. Chapter 3: Heat transfer to objects in pool fires. In: Sunden B, Faghri M, editors. Transport Phenomena in Fires, vol. 1. 1st ed., WIT Press; 2008, p. 69–136. https://doi.org/10.2495/9781845641603/03.
[78] Franchini A, Galasso C, Torero JL. Optimising the inherent fire capacity of structures. Fire Safety Journal 2023;141:103883. https://doi.org/10.1016/j.firesaf.2023.103883.
[79] ISO. ISO 834-11:2014 Fire resistance tests — Elements of building construction — Part 11: Specific requirements for the assessment of fire protection to structural steel elements. Geneva, Switzerland: International Organization for Standardization; 2019.

[80] ASTM Standard E119-19. Test Methods for Fire Tests of Building Construction and Materials. West Conshohocken, PA: ASTM International; 2019. https://doi.org/10.1520/E0119-19.
[81] ASTM Standard E1529-22. Test Methods for Determining Effects of Large Hydrocarbon Pool Fires on Structural Members and Assemblies. West Conshohocken, PA: ASTM International; 2022. https://doi.org/10.1520/E1529-22.
[82] CEN. EN 1991-1-2:2002 Eurocode 1: Actions on structures - Part 1-2: General actions - Actions on structures exposed to fire. Brussels, Belgium: European Committee for Standardization; 2009.
[83] Kodur VKR, Naser MZ. Importance factor for design of bridges against fire hazard. Engineering Structures 2013;54:207–20. https://doi.org/10.1016/j.engstruct.2013.03.048.
[84] Rubert A, Schaumann P. Critical temperatures of steel columns exposed to fire. Fire Safety Journal 1988;13:39–44. https://doi.org/10.1016/0379-7112(88)90031-8.
[85] SSSBA. eSPAN140. Washington, D.C.: Short Span Steel Bridge Alliance; 2017.
[86] AASHTO. AASHTO LRFD Bridge Design Specifications, 7th Edition. Washington, D.C.: American Association of State Highway and Transportation Officials; 2014.
[87] ASTM Standard A709-17. Standard Specification for Structural Steel for Bridges. West Conshohocken, PA: ASTM International; 2017.
[88] PCI. MNL-133-23: Bridge Design Manual, 4th Edition. Chicago, IL: Precast/Prestressed Concrete Institute; 2023.
[89] CEN. EN 1993-1-2:2005 Eurocode 3: Design of steel structures - Part 1-2: General rules - Structural fire design. Brussels, Belgium: European Committee for Standardization; 2005.
[90] AISC. Specification for Structural Steel Buildings (ANSI/AISC 360-22). Chicago, IL: American Institute of Steel Construction; 2022.
[91] Jansson R. Fire spalling of concrete – A historical overview. MATEC Web of Conferences, vol. 6, 2013, p. 01001. https://doi.org/10.1051/MATECCONF/20130601001.
[92] Franssen J-M, Gernay T. User's manual for SAFIR 2019: A computer program for analysis of structures subjected to fire. Liege, Belgium: University of Liege; 2019.
[93] Drury MM, Kordosky AN, Quiel SE. Structural fire resistance of partially restrained, partially composite floor beams, II: Modeling. Journal of Constructional Steel Research 2020;167:105946. https://doi.org/10.1016/j.jcsr.2020.105946.
[94] International Center for Numerical Methods in Engineering (CIMNE. GiD: The personal pre and postprocessor. Barcelona, Spain: 2016.
[95] Quiel SE, Irwin CH, Naito CJ, Vermaak N. Mechanical Characterization of Normal and High-Strength Steel Bars in Reinforced Concrete Members under Fire. Journal of Structural Engineering 2020;146:17. https://doi.org/10.1061/(ASCE)ST.1943-541X.0002644.
[96] CEN. EN 1992-1-1:2004 Eurocode 2: Design of concrete structures - Part 1-1: General rules and rules for buildings. Brussels, Belgium: European Committee for Standardization; 2004.
[97] Olsson AMJ, Sandberg GE. Latin Hypercube Sampling for Stochastic Finite Element Analysis. Journal of Engineering Mechanics 2002;128:121–5. https://doi.org/10.1061/(ASCE)0733-9399(2002)128:1(121).
[98] Cortes C, Vapnik V. Support-Vector Networks. Machine Learning 1995;20:273–97. https://doi.org/10.1007/BF00994018.
[99] Carlton A, Guo Q, Ma S, Quiel SE, Naito CJ. Experimental assessment of explosive spalling in normal weight concrete panels under high intensity thermal exposure. Fire Safety Journal 2022;134:103677. https://doi.org/10.1016/j.firesaf.2022.103677.
[100] Mueller K, Marjanishvili S, Quiel S. Resilient Bridge Design Framework to Extreme Fire Loading. Proceedings of the 9th International Conference on Structures in Fire (SiF'16), Princeton, NJ: 2016, p. 10.
[101] Google Maps. MacArthur Maze Interchange, Oakland, CA (37°49'45"N 122°17'35"W) 2024. https://www.google.com/maps/search/macarthur+maze+oakland+ca/@37.8288779,-122.2969687,16z?entry=ttu.

[102] Pearlman J, Meltzer N. Risk of Commercial Truck Fires in the United States: An Exploratory Data Analysis. Cambridge, MA: John A. Volpe National Transportation Systems Center; 2012.
[103] Ahrens M. NFPA Research: Vehicle Fires. Quincy, MA: National Fire Protection Association; 2020.
[104] PIARC Technical Committee 3.3. Experience with Significant Incidents in Road Tunnels. Paris, France: World Road Association (PIARC); 2016.
[105] NFPA. NFPA 557: Standard for Determination of Fire Loads for Use in Structural Fire Protection Design. 2023rd ed. Quincy, MA: National Fire Protection Association; 2023.
[106] Marelli S, Lamas C, Konakli K, Mylonas C, Wiederkehr P, Sudret B. UQLab user manual – Sensitivity analysis. Zurich, Switzerland: ETH Zurich; 2023.
[107] Li Z, Yoon J, Zhang R, Rajabipour F, Srubar Iii WV, Dabo I, et al. Machine learning in concrete science: applications, challenges, and best practices. Npj Computational Materials 2022;8:127. https://doi.org/10.1038/s41524-022-00810-x.